

Rochester Institute of Technology

**RIT Digital Institutional Repository**

---

Theses

---

2024

## **Characterization of Curing Kinetics of an Anisotropic Conductive Adhesive using Rheology and Differential Scanning Calorimetry**

Connor Kirkpatrick  
crk7940@rit.edu

Follow this and additional works at: <https://repository.rit.edu/theses>

---

### **Recommended Citation**

Kirkpatrick, Connor, "Characterization of Curing Kinetics of an Anisotropic Conductive Adhesive using Rheology and Differential Scanning Calorimetry" (2024). Thesis. Rochester Institute of Technology. Accessed from

This Thesis is brought to you for free and open access by the RIT Libraries. For more information, please contact [repository@rit.edu](mailto:repository@rit.edu).

# **Characterization of Curing Kinetics of an Anisotropic Conductive Adhesive using Rheology and Differential Scanning Calorimetry**

By

Connor Kirkpatrick

A thesis submitted in partial fulfillment of the requirements for the degree of Master of Science in the  
Materials Science and Engineering in School of Chemistry and Material Science

Supervised by

Dr. Christopher Lewis

College of Science

Rochester Institute of Technology

Rochester, New York

2024

School of Chemistry and Material Science  
College of Science  
Rochester Institute of Technology  
Rochester, New York

**CERTIFICATE OF APPROVAL**

The M.S. degree thesis of Connor Kirkpatrick has been examined and approved by the thesis committee as satisfactory for the thesis required for the M.S. degree in Material Science and Engineering.

**4/19/24**

---

Dr. Christopher Lewis (Thesis Advisor)

Date

**4/19/24**

---

Dr. Martin Anselm

Date

**4/19/24**

---

Dr. Matt Miri

Date

**4/19/24**

---

Dr. Iris Rivero

Date

**4/19/24**

---

Dr. Scott Williams (MSE Graduate Program Director)

Date

## **Acknowledgements**

I would like to express my deep gratitude and appreciation to my advisor, Dr. Christopher Lewis, for his patience and guidance. The motivation given to me was crucial to me for completing this research. His input always steered me down the path of the greatest learning, and for that, he has my utmost respect.

I am sincerely grateful to my mentor and colleagues, Dr. Martin Anselm, and Seraphim Wieber for inspiring me and helping me to gain a better understanding and interest in the field. It was an honor to work with Dan Balder (SRS) and Brent Skupien (SRS) as they encouraged and instigated the research that led to this thesis.

I would also like to thank my thesis committee members Dr. Scott Williams, Dr. Martin Anselm, Dr. Matt Miri, and Dr. Iris Rivero for their comments and suggestions along with the patience and time given to my thesis completion. I would also like to thank Tom Allston and the School of Chemistry and Material Science for their help.

A special thanks to my friends, made both in my hometown, who have stuck with me all the way, and the friends made at college who grew with me. Finally, I would like to thank my family who were unwavering in their support of me and my future, for which I am most grateful.

## Abstract

A kinetic study performed to further the understanding of a novel magnetically aligned anisotropic conductive adhesive (ACA) was performed using differential scanning calorimetry (DSC) and a rheometer, under both isothermal and non-isothermal conditions. Isothermal data was collected at 70, 80, and 90°C, whereas non-isothermal data was collected at 5, 10, 20, and 30°C/min, with results interpreted through the use of an autocatalytic model. For isothermal experiments, the rate of conversion was found to increase with increasing isothermal curing temperature, and this was reflected in the kinetic rate constant. Moreover, the rate constant determined by DSC was found to range from  $2.6 \times 10^{-3}$  -  $5.2 \times 10^{-3}$  whereas values of  $k$  from  $4.6 \times 10^{-3}$  -  $9.6 \times 10^{-3}$  when determined using rheology. Similarly, the rate of reaction generally increased with increasing non-isothermal heating rate and again differences were noted when comparing results obtained from the two models. The activation energies for the rheological and DSC data sets for isothermal runs were 38.2kJ/mol and 61.5kJ/mol respectively. The average fit constant values,  $\ln(A)$ ,  $m$ , and  $n$ , found for the rheological and DSC data sets for isothermal runs were 8.1, 0.61, and 0.73 for rheology, and 15.6, 0.78, and 0.71 for DSC results. For isothermal rheology, the values of  $m$  were found to decrease with increasing isothermal temperature, the same was found for  $n$  where the values decrease as temperature increases. For isothermal DSC results, the values of  $m$  were found to decrease slightly with an increase in isothermal temperature where the value of  $n$  stayed relatively the same. For non-isothermal experiments, the rheological and DSC activation energies were found to be 46.5kJ/mol and 60.8kJ/mol respectively. The fit constants,  $\ln(A)$ ,  $m$  and  $n$  found for the rheological and DSC data sets for non-isothermal runs were 11.27, 0.55, and 0.86 for rheology, and 13.4, 0.69, and 0.73 for DSC results. Non-isothermal rheology values of  $m$  and  $n$  were both found to increase as the non-isothermal cure rate was increased. Non-isothermal DSC values showed a trend of a decreasing value of  $m$  with an increasing rate, and a trend of a decreasing value of  $n$  with an increase in non-isothermal rate.

## Table of Contents

Chapter 1: Introduction .....	1
Chapter 2: Literature Review .....	4
2.1 PCBs and substrates:.....	4
2.2 Electrically Conductive Adhesives:.....	7
2.3 Metallic ECA fillers: .....	14
2.4 Carbon ECA filler types:.....	16
2.5 DSC and Rheology Fundamentals: .....	18
2.5.1 DSC: .....	18
2.5.2 Rheology: .....	20
2.6 Curing Kinetics of Adhesives: .....	23
2.6.1 Kinetic models:.....	23
2.6.2 Isothermal Methods: .....	26
2.6.3 Non-isothermal Methods:.....	28
Chapter 3: Experimental .....	31
3.1 Materials: .....	31
3.2 Differential Scanning Calorimetry:.....	31
3.3 Rheology: .....	32
Chapter 4: Results and Discussion .....	34
4.1 Isothermal Behavior-DSC: .....	34
4.2 Isothermal Behavior-Rheology: .....	44
4.3 Non-Isothermal Behavior-DSC: .....	54
4.4 Non-Isothermal Behavior-Rheology: .....	64
4.5 Comparison of Rheology / DSC Results:.....	74
Chapter 5: Conclusions and Future Work .....	80
5.1 Conclusion:.....	80
5.2 Future Work: .....	81
Appendix: .....	83
Supplementary Tables: .....	83
Supplementary Figures: .....	88
References: .....	97

## Chapter 1: Introduction

Electronics manufacturing is the process used to produce electronic equipment; most notably it's the process used to manufacture circuit boards used in products such as computers, consumer electronics, etc. The electronics manufacturing industry has a compounding advancement in electronic technology and thus strongly contributes to the global economy. Within electronics manufacturing, solder is often used as the electrically conductive, bonding material utilized to attach components to an integrated circuit within an interconnect.

Anisotropic Conductive Adhesives (ACAs) are commonly found Electrically Conductive Adhesives (ECAs) used in interconnect systems where solder is found to be ineffective. ECAs are typically a polymer based medium with conductive components and materials used as fillers. ACAs can offer superior properties to conventional solders including good chemical and thermal resistance and exceptional mechanical properties (Aradhana 2020). These anisotropic conductors can be implemented as films or pastes. Films typically come pre-rolled, with the intention of laying it between an integrated circuit and its connection point. These films are typically heat and pressure activated to provide anisotropic connection across a plane, the most common case being used in modern LCD displays. In contrast, pastes have more variety: For example, pastes can come as thermoplastics or thermosets, pending environmental needs. Unlike films, pastes allow for tailoring of the bond thickness and therefore conductivity. They can also be used on a component-to-component basis, which is their main advantage over films. Pastes can be set up in dispensers similar to solder, however the curing of these pastes requires much more attention.

Anisotropic conductive pastes are typically made with an epoxy and a metallic filler, of different shapes and composition. The filler particles for an anisotropic conductive paste must be aligned if they are not pre-shaped to provide a conduit for current flow in a single direction. This is most commonly done using contact conduction achieved through heat and pressure of the material allowing adhesion (Li 2006).

Another way to align filler particles is via a uniform magnetic field with field lines passing perpendicular to the mounting surface; this is how the particles are aligned in Ztach ACA, the commercially available ACA material examined in this study. The magnetic field drives the formation of columns of particles that allow for conductivity in the z-axis within the interconnect. These columns must be formed while the epoxy is not cured as the mobility of filler particles approaches zero as the epoxy cures.

Understanding the curing behavior and viscoelastic properties of an ACA is imperative to the performance of the material in its final application. The properties of an anisotropic conductive paste change drastically during its cure (Hoang-Vu 2013). Without the proper procedure for production, issues like poor conductivity due to lack of contact or column formation, poor final material dispersion or component slippage due to a low viscosity during manufacturing, can cause poor performance and even device failure.

In this study, the isothermal and non-isothermal curing kinetics of a commercially available ACA is investigated using Differential Scanning Calorimetry (DSC) and rheometry. DSC is a method of thermal analysis that involves monitoring heat flow of a material and is often used to measure transitions such as  $T_g$ ,  $T_m$ , etc. and/or the heat evolved during chemical reactions. Alternatively, rheometry measures the viscous and/or viscoelastic properties of a material and for the case of polymers, is highly sensitive to molecular weight. These two methods are fundamentally measuring different phenomena and therefore provide complementary information. As such, the combination of these two results allows for a more complete description of the curing behavior of this ACA.

Isothermal studies were conducted at 70, 80, and 90°C and the results are discussed in Chapter 4. The data was then fitted to a rate equation that, through the Arrhenius equation, enabled an assessment of the influence of temperature on the resulting kinetics. The model used to fit all data sets is the Šesták-Berggren autocatalytic kinetic model (Šesták 1971).

Non-isothermal studies were also performed on both DSC and rheological data, and this is shared in Chapters 4.3 and 4.4. Since this model is temperature dependent and not rate dependent, the temperature

values from experimental data were used in the fitting process for a three-dimensional fit. For non-isothermal data sets, the Kissinger-Akahira-Sunrose method was used to determine the activation energy in a model independent calculation. As with isothermal experiments, data was then fitted to determine a final equation that expresses reaction kinetics as a function of temperature.

The scope of this study focused on assessing the kinetics of a novel ACA using DSC and rheology. Applying the same model and methods to two different instruments measuring inherently different things allows a comparison that enables a clearer understanding of how each of these processes work.

# Chapter 2: Literature Review

## 2.1 PCBs and substrates:

Circuit boards are designed to hold electronic components by providing infrastructure using a flat piece of material through which conductive pathways enable the full functionality of the board. Where components could be connected by wires with full functionality, circuit boards enable a much more space efficient way to package an electronic device. Circuit board backings, usually called the substrate, are a non-metallic material used to support the conductive material that connects the circuits (Grout 2008). Shown in Figure 1 is a circuit board with only the connections laid out, no components attached. While some connections can be seen topically on the green substrate, other connections are within or underneath the board as the connections of various components cannot cross. The shapes and lines on the circuit board in Figure 1 represent the locations where the designated electronic components need to be connected to produce a functional circuit board.

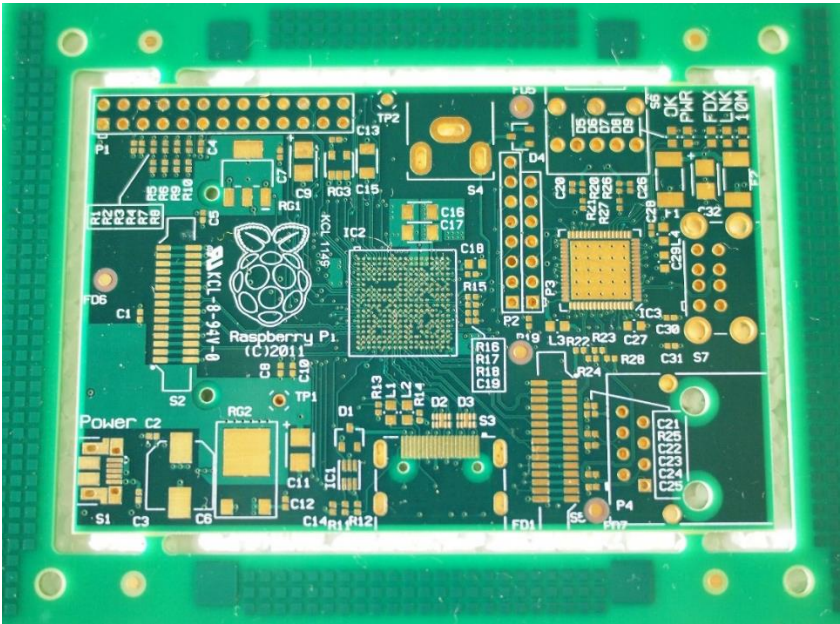


Figure 1: Unpopulated circuit board shown with only connections laid (Upton)

A Printed Circuit Board (PCB) is a large piece of insulator coated with metal; the metal can then be etched after protecting the desired pathways with a type of etch resistor to allow only the pathway to remain after the etch. An example of production processes used to prepare a PCB is shown in Figure 2. Vias are holes that are used to connect different layers of the material, back to front, or if the circuit is more complex, to the middle layers of the board (Martha). The layers of the board and the components themselves are typically connected using solder, which is historically an alloy of tin and lead. The solder mask shown is used to keep the solder in place as the circuit board moves through an oven to set the solder and complete the electrical connections. Many different types of substrates can be used, but some applications and environments require the robustness of having a circuit board that can withstand bending and vibrations without these layers delaminating (Cheng).

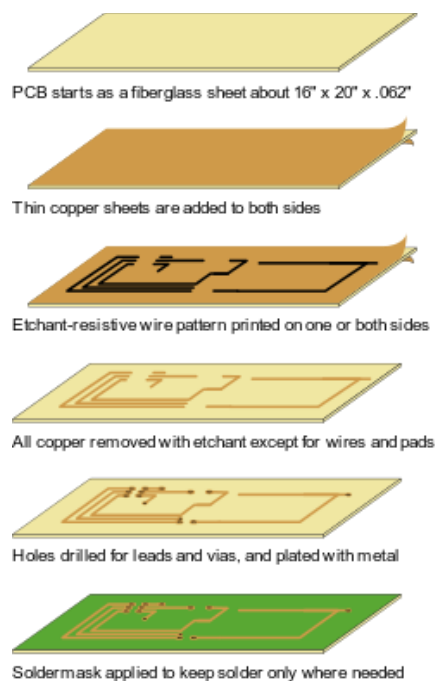


Figure 2: Depiction of process to create a printed circuit board (Martha)

To ensure the versatility of produced electronic instruments, a flexible substrate material can be used to make PCBs. These are typically made with a polyimide composite which increases both the flexibility and thermal conductivity depending on the composite chosen (Kumar). The demand for

miniaturization and robustness of electronic devices comes from the rapid increase in power density of electronics. This type of technology is often implemented in wearable technology and the harsh environments of the defense and aerospace sector (Aradhana). This requires the design of a material that is both flexible while still retaining its thermal conductivity. Polymers used in electronics manufacturing typically have a thermal conductivity of less than 0.2 W/m-K. Carbon based nano structures have gained more support due to their high thermal conductivity, 3000-3500 W/m-K and desirable mechanical properties. Graphene has also shown a large advantage over other polymers boasting a thermal conductivity rivalling carbon based nano structures at 2000-3000 W/m-K. This peaks a large interest in the use of high thermally conductive polymer composite with graphene layers (Aradhana).

The choice of connection material is just as important as the type of substrate used. The most popular choice for connection material is a basic lead/tin (SnPb) solder. SnPb solder has been used for over 50 years to produce electronics due to its pricing, reliability and ease of use, and its soldering properties. SnPb solder presents good conductivity as well as good manufacturability (Cheng).

Conventional SnPb solder offers low resistivity and rigid structure, which explains why it has been historically the premier interconnect choice for the production of electronics. SnPb solder does not fit all modern situations: Pb is toxic and presents an environmental hazard. Conventional solder also has a high setting temperature which may drive up the cost of large-scale production and possibly cause issues if there are temperature sensitive components being bonded (Mir, Aradhana).

The substrate and binder of a flexible circuit board are an extremely important aspect of making a robust electronic product. Flexible printable circuit board packages can only be as strong as their weakest link. As such, the material used to bond the interface together is just as important as the substrate, if not more so. If parts of the substrate delaminate, the thermal dissipation of the material is compromised but may still work conditions pending. If the bond between components delaminates, a loss in functionality of the product or even total failure could occur.

The best option to use when attempting to create a flexible and heat resistance environment is to use an Electrically Conductive Adhesive (ECA). ECAs have many advantages over conventional solder, both in production and application. ECAs, being polymeric in nature, are more ductile than solders and therefore are better able to conform in flexible electronics applications. Moreover, ECAs offer lead free environmentally friendly options, a lower curing temperature to protect components and lower costs, dimensional stability due to the composition of the ECA, and offer larger bonding options as conventional solder cannot be used on such things as glass. This makes ECAs a binder that is superior to solder when applied correctly (Aradhana, Li).

## 2.2 Electrically Conductive Adhesives:

Electrically Conductive Adhesives (ECA) are conductive filled thermosets, typically epoxy, that are widely used in many electronic applications. Some applications include solderless interconnects, component modernization, display interconnects, and those that require better heat management. ECAs are based on inducing conduction via a polymer composite, which gives ECAs advantages over solder such as a lower heat processing temperature, a more environmentally safe method when compared to common lead solder, high flexibility, and low production cost (Aradhana).

ECAs can be categorized as either Anisotropic Conductive Adhesives (ACA) or as Isotropic Conductive Adhesives (ICA). As the name implies, ACAs are conductive only in one direction, typically the Z-axis, whereas ICAs are a uniform conductive material. There are two mechanisms to achieve conductivity through the polymer (Figure 4). As shown, one method is to disperse conductive particles within an insulating polymer, whereas the second method requires a more evenly dispersed filler composition. Another option would be to blend an inherently conductive polymer with another insulating polymer (Li). Some examples of types of ECAs are shown in Figure 3.

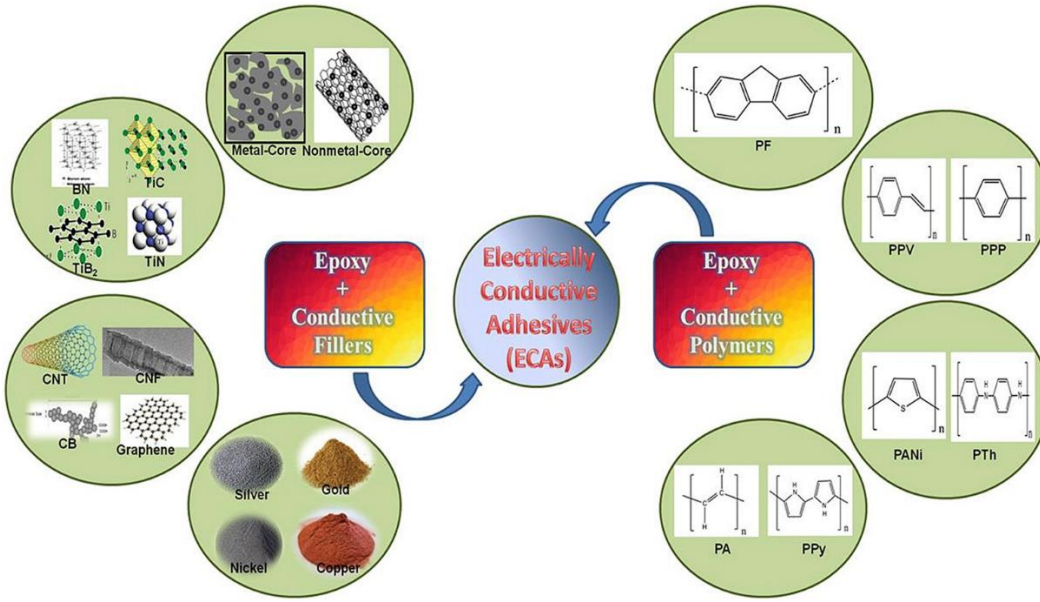


Figure 3: Examples of types of ECAs with named materials used for the conductive fillers for an ECA composition (Aradhana)

These methods require different mechanisms to achieve electrical conductivity. Firstly, particle to particle conductivity is required for those systems utilizing conductive fillers: Conductivity is achieved by the contact between conductive filler particles. For ECA's based on conductive polymers, polymer conductivity, relies on mechanisms of tunneling, hopping, and charge carrier injection to create conductivity throughout the material (Aradhana). The focus of this section is mainly around ACAs, as they're most suitable for high density electronic applications and therefore only those systems utilizing conductive fillers will be discussed.

ACAs are inherently much more complex than ICAs. Likewise, ACAs require specialized bonding equipment and methods as compared to solder. ACAs will not be conductive until the correct amount of heat and pressure are applied. For the correct contact of the filler particles to the contact plate, the correct amount of pressure allows for the correct gap size, while the correct heat will ensure the resin is fully cured allowing the conduction to hold after pressure is released (Li). Shown in Figure 4, ACA and ICA fillers are presented in their practical application. For ACAs to be unidirectional, there is an extremely sensitive gap that allows the particles to fill between contact points but restricts it from forming conductivity in other

areas. ACAs typically have conductive filler concentrations around 5-20% by volume which keeps the material within the threshold of establishing a conductive path along more than one axis, depending on gap application. ACAs be classified in another way, unidirectional, or bidirectional. Depending on the application, ACAs can be designed to conduct only in one axis, or along two axes, which can be regulated by the external forces applied to the material (Aradhana).

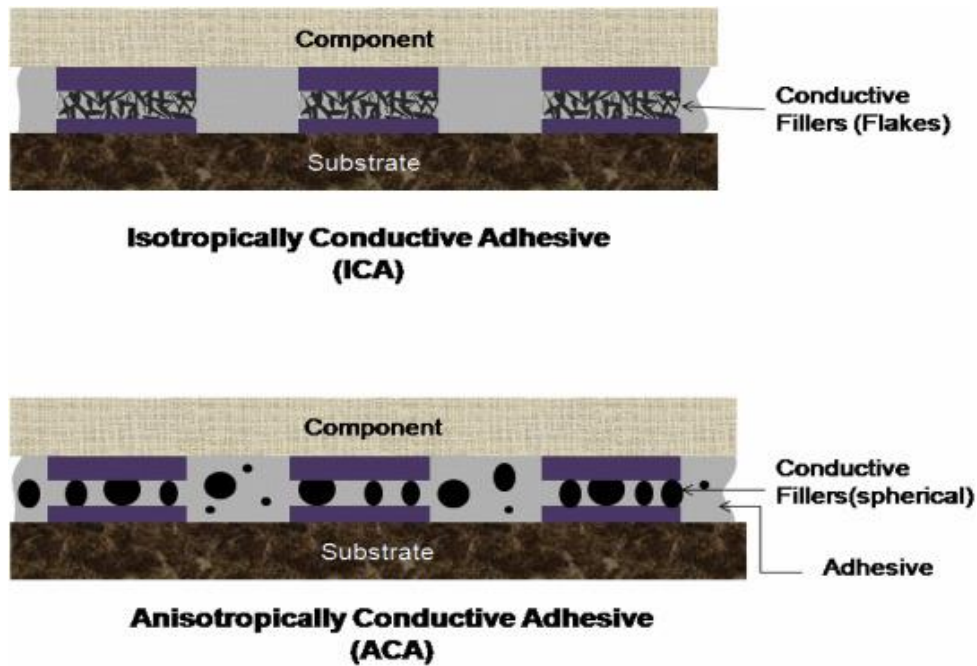


Figure 4: Types of ECAs: ICAs and ACAs, filler adhesion diagram (Aradhana)

Commercially available ACAs can be supplied as either thermoplastic or thermosetting materials. ACAs are also available in the form of a paste, or film. Pastes are used by sandwiching the material between the interconnect and applying the correct amount of heat and pressure which bonds the two connections together establishing conductivity. Once completed, the polymer is then hardened, and the bond made complete (Li). ACA films, also called ACAF, work in a similar fashion to the paste variant. Within the film there is a random distribution of conductive particles. The filler content of the material is designed such

that when the correct heat and pressure are applied, the film will then have conductivity in a singular direction. An example of an application where ACAFs are used is flat digital displays. The high density and high heat application make using conventional solder difficult. With the ACAF the heat and component spacing can be adjusted for a higher performance (Li). An example setup of an ACF is shown in Figure 5.

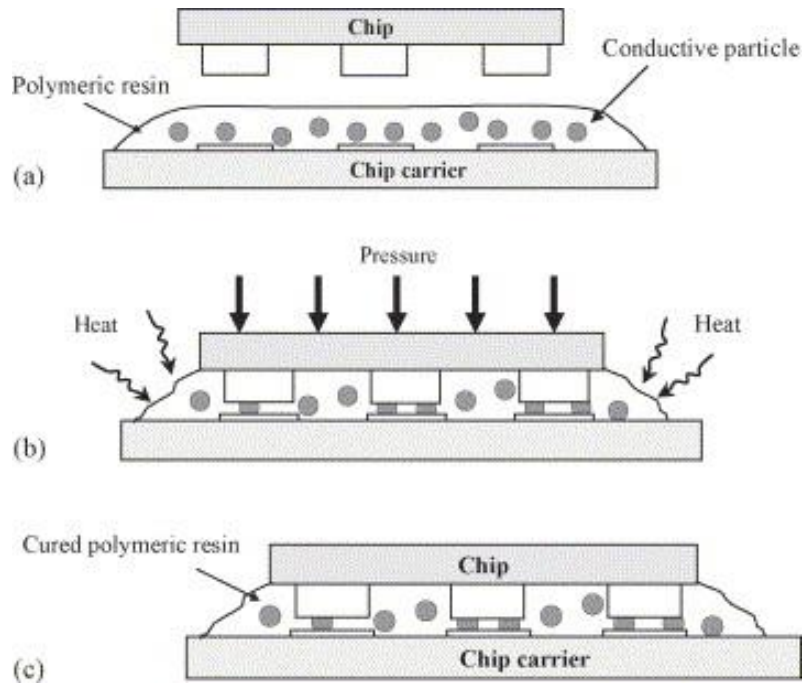


Figure 5: Diagram of ACAF application during processing to achieve conductivity in the z-direction. A) the layering of the film on the chip carrier B) the application of heat and pressure to bond the epoxy and create conductivity between chip and carrier C) the fully cure ACF (Li)

ACAs typically use a spherical filler particle to achieve unidirectional conductivity, which can restrict the contact through the x and y axes. ICAs will typically use a flaked shaped filler particle to increase the conductivity of the material in all directions.

Ztach ACA, is a proprietary ACA (Sunray Scientific, Eatontown, NJ), and functions using a different method to achieve unidirectional conductivity. Instead of relying on the ability of the contact plates compressing the conductive filler, the particles within Ztach are ferro-magnetic, they are made using

materials such as iron and nickel. To enhance electrical conductivity, particles are usually coated with Ag or Au. These conductive spherical particles are aligned using a uniform magnetic field adjacent to the circuit board to align the particles while the adhesive is curing. When the particles are aligned, they form columns which create unidirectional conductivity. This is shown in Figure 6. Though the specific formulation of Ztach is proprietary, the general filler composition of ZTACH formulations have been reported in the literature and are shown here in Table 1 (Ramkumar 2011).

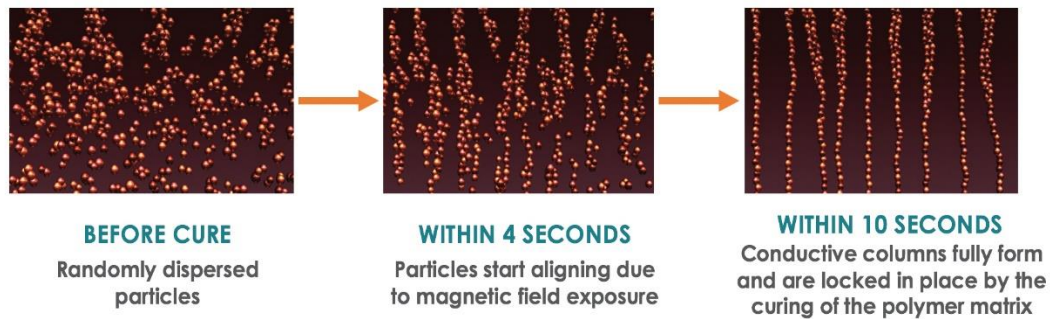


Figure 6: ZTACH ACE curing using a magnetic plate with particle position represented through the process (ZTACH ACE)

Table 1: Formulations of several ZTACH ACA formulation as described in the literature (Ramkumar 2011)

ZTACH Formulations	A-Type	2515CH (F-Type)	830NS	330FS
Filler Particle Size	25 $\mu\text{m}$	8 $\mu\text{m}$	8 $\mu\text{m}$	3 $\mu\text{m}$
Filler Core	C/Ni	C/Ni	Ni	Fe
Filler Coating	8% Au	8% Au	40% Ag	40% Ag
Filler Weight%	14	30	30	30

The filler is added to a thermosetting polymer, such as a two-part epoxy, where the pot life of the formulation depends on the formulation of the polymer used. The majority of formulations showed a pot life of four to eight hours (Ramkumar 2011). The particle alignment and column formation process following the application of a magnetic field is shown in Figure 7.

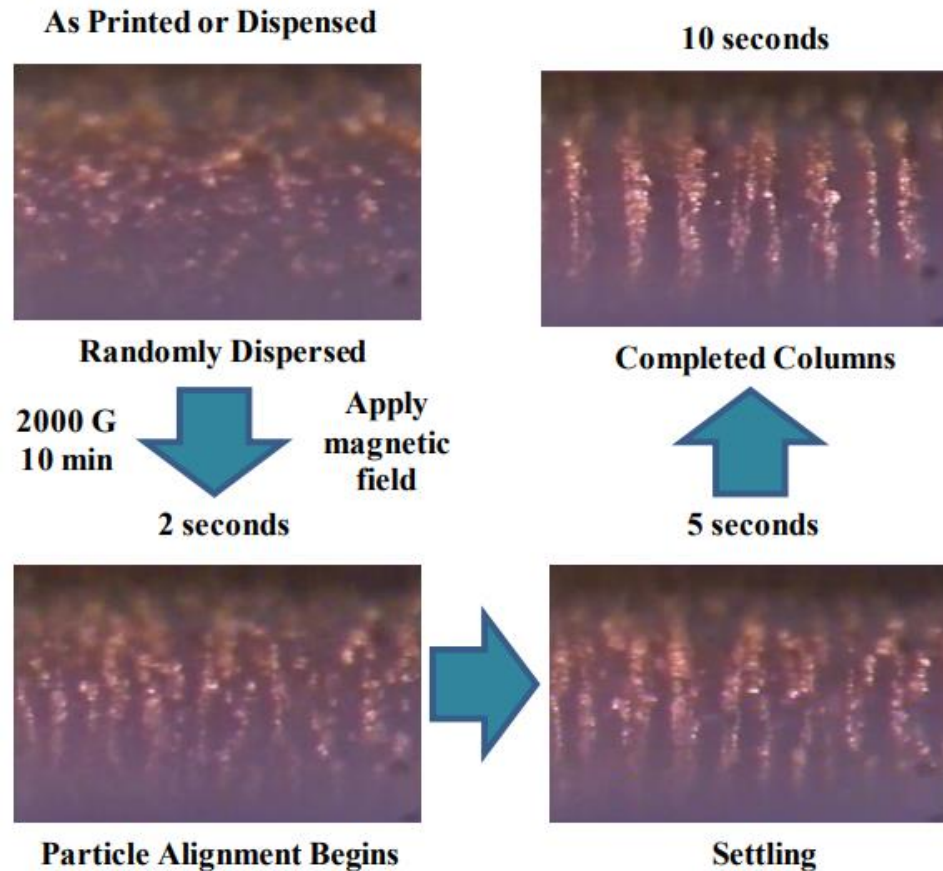


Figure 7: Column formation of ZTACH ACA in seconds after magnetic field is applied (Ramkumar 2011)

As shown in Figure 7, after the magnetic field is applied, the particles form into columns, guided by the magnetic field lines. This allows for uniform Z directional conductivity. Another ability Ztach has over typically ACAs is the ability to use the material without component or substrate posts. With typical ACA alignment, shown in Figure 5, the typical ACA must be compressed using a post which is what actually comes into contact with the conductive filler. Ztach allows for conduction with flush contact points and is therefore less complicated to use in a manufacturing setting. Numerous papers have been published regarding the properties and characteristics of ZTACH and other magnetically cured ACAs as it's becoming a more favorable option in the electronics industry (Ramkumar 2006-2007-2011, D'Angelo). While the full composition of the material is unknown, it is assumed that the binder material is a type of basic epoxy. A basic epoxy structure and reaction are shown in Figure 8.

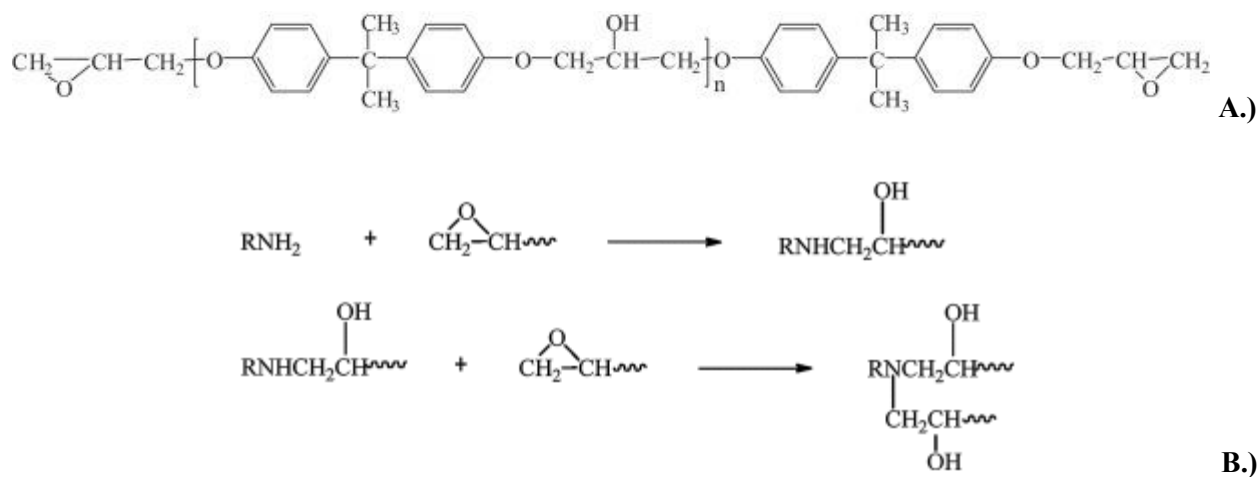


Figure 8: A.) A Chemical structure of diglycidyl ether of bisphenol-A B.) Cure reaction mechanism of amine and epoxide (Jin).

Epoxyes are a type of thermosetting resin characterized by having high stiffness and a high glass transition temperature. A typical epoxy is shown in Figure 8a. Notably the molecule has an epoxide group on each end that can react with a hardener to form a fully cross-link network. Hardeners are generally composed of amines and react according to the scheme shown in Figure 8b. Here they react with two epoxides to form the beginning stages of a cross-link network (Jin). In this work rheology and DSC will be used to follow this reaction and therefore describe its kinetics.

### 2.3 Metallic ECA fillers:

There are four main types of conductive fillers: metal fillers, carbon fillers, ceramic fillers, and metal coated fillers. Examples shown in Figure 9. These are the most commonly used fillers in industry and research.

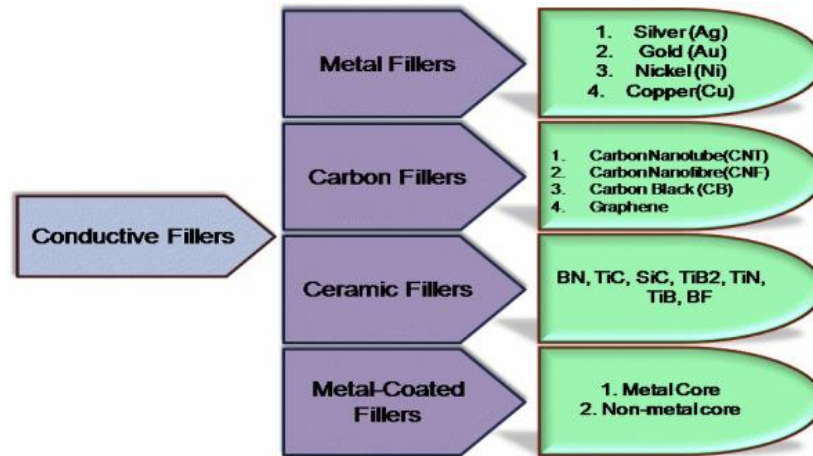


Figure 9: Types of conductive fillers (Aradhana)

Metal fillers are typically less than 20 $\mu$ m in diameter. Metallic fillers can be manufactured using varying milling techniques such as ball milling, impact milling, and gyratory milling. Typically, with metallic fillers, a large distribution of particle size is used while using a lower concentration of the filler which allows the material to pass the percolation threshold. In short, the percolation threshold is the amount of filler needed to shift from a less conductive material to a much more conductive material (Gong). This relationship is shown in Figure 10a for a sample of polypropylene with carbon black as a filler, compared against the same composite with a segregated structure. When the different composites are tested with certain amounts of filler, they reach a point where the ratio of the resistivity to the amount of filler in the sample decreases greatly. This is where the percolation threshold can be found. Percolation theory is extremely important when creating an ECA. With too little filler, the resistivity of the material is much higher than needed; with the right amount of filler, the composite will have good resistivity without a large

change in properties. This figure showcases the ability of the structure of the conductive network to greatly lower the amount of filler needed to achieve good conductivity. It's shown in Figures 10b, and 10c, that the  $\phi_c$  value, the predicted percolation threshold, is lower for the segregated structure which will lead to better conductivity at lower filler amounts.

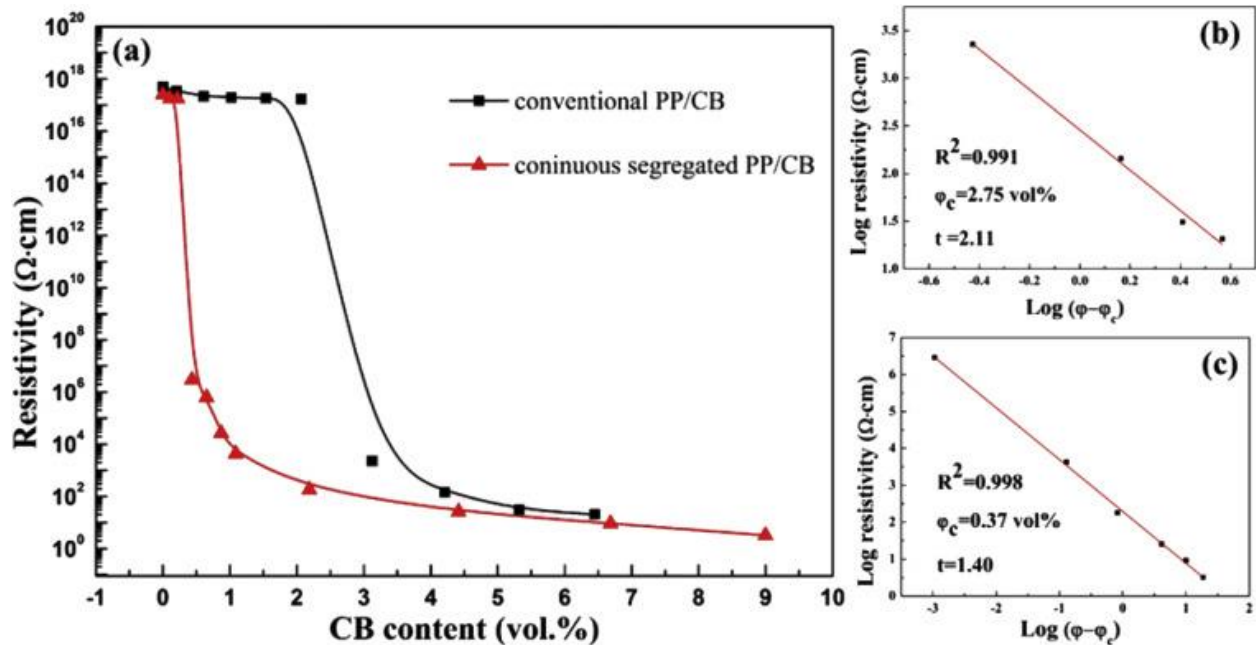


Figure 10: (a) dependance of resistivity on CB (b: conventional PP/CB / c: segregated PP/CB) fits of experimental data using percolation theory (Gong)

Silver metallic fillers are a popular choice for filler particles as they offer a high conductivity both electrically and thermally. It's also notable that the oxides of silver are still more conductive than many metals which eliminates some complications when heating. Other shapes for silver have also been a topic of research. Some studies show that when using silver particles in their nano-form, including nano-wires, nano-rods, and nano-particles, have shown superior electrical conductivity when compared to their micro-forms. Gold is also a commonly used metallic filler. Gold is often used in electronics to coat components

as it offers good electrical conductivity as well as oxidation and corrosion resistance. Yet, gold is used less on an industrial scale as it is still an expensive noble metal, which often is not budget friendly (Li).

Nickel is also a common metal used in fillers as it's an ingredient in many alloys. This is due to its slow oxidation process. Different types of Nickel powders and the processes used to manufacture them to produce spheres and flakes that stabilize with an oxide coating, typically at approximately 0.8% oxygen (Krupa). Nickel is commonly used in ACAs, while nickel has a higher resistivity when compared to other metals listed; the gap between contact points is typically very low in the application of an ACA which implies the resistivity matters less (Li, Gul).

#### 2.4 Carbon ECA filler types:

Carbon fillers are made of carbon atoms, which are very inert and moldable to many different forms. The most common allotropes of carbon being diamond and graphene. Other common forms include walled carbon nano tubes, nano fibers, and carbon black. Some of these structures are shown in Figure 11.

Fillers such as graphene or carbon black have good electrical conductivity. However, when the structures are brought down to the nano scale such as with carbon nano tubes, they exhibit superior electrical conductivity due to their large surface to volume ratio (Aradhana).

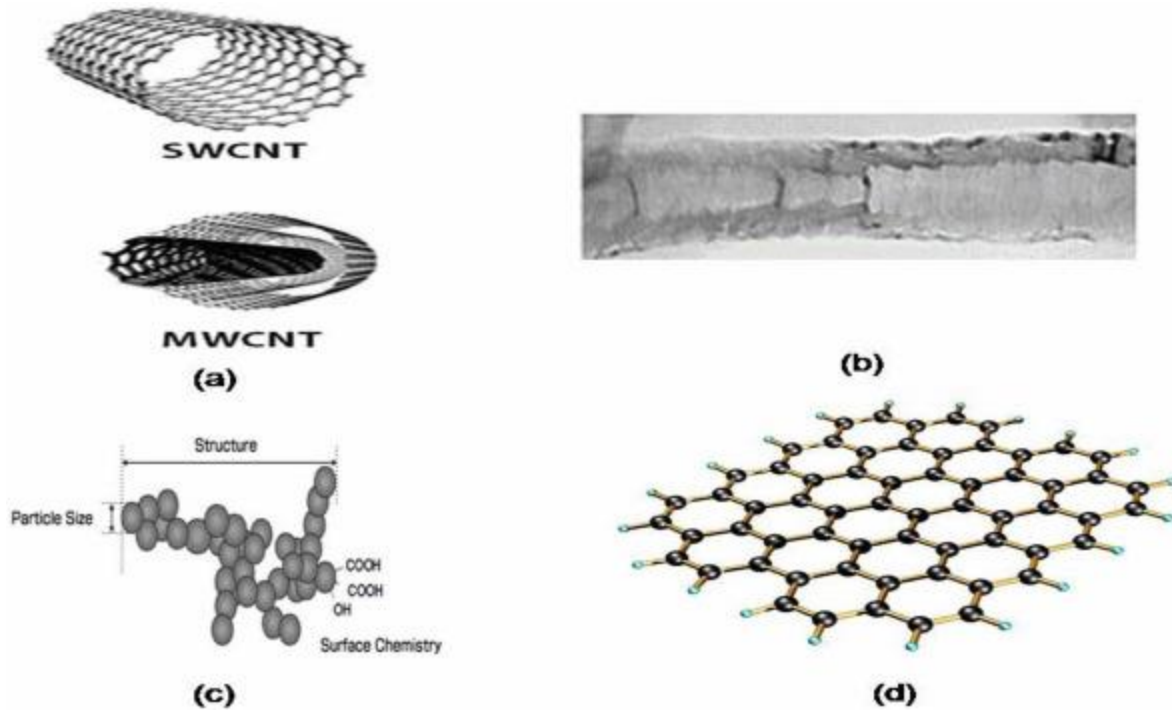


Figure 11: Structures of carbon-based fillers (a) single walled nano-tube and multi walled carbon nano-tube (b) carbon nanofiber (c) carbon black (CB) (d) graphene (Aradhana)

Carbon nano tubes are a popular choice of nano filler as they can impose their own properties on the polymer or adhesive they're added to. Carbon nano tubes exhibit high strength and modulus, a large surface to volume ratio, excellent thermal and electrical conductivity, and thermal stability at high temperatures. Carbon nano tube structures consist of many Van der Waal forces which can result in clustering of the carbon nano tubes which inhibits the ability of the filler to impart the desired properties mentioned prior. Many ways to disperse the carbon nano tubes within the polymer or adhesive have been studied. Some methods found to combat this include the use of ultra sonification as well as the use of surfactants to evenly disperse the filler for greater performance (Aradhana).

Carbon black is also a highly researched filler as its cost of manufacturing is very low. Carbon black is a paracrystalline carbon filler, meaning it possesses both short and medium range ordering in lattice structure, which is comprised of more than 97% elementary carbon grouped into clusters, shown in Figure 11c. Carbon black is a very desirable reinforcing filler as it holds properties similar, but less than that of

carbon nano tubes (Aradhana, Gul). The true properties of carbon black depend on many variables such as the particle size, structure, and impurities and functional groups present. Carbon black can also have a large effect on the curing kinetics among the other properties discussed. Direct relations to the activation energy of the adhesive and the amount of carbon black filler added have been studied (Trihotri).

## 2.5 DSC and Rheology Fundamentals:

### 2.5.1 DSC:

Differential Scanning Calorimetry (DSC) is one of the most widespread analytical techniques used for the determination of the properties of both unreacted and reacted thermosets. Conventional DSC is the most basic method, which involves measuring heat flow with the comparison of the sample to a reference. This can be done using a constant rate of heating or cooling, or a constant temperature. With the analysis of DSC results, properties like melting point, glass transition, and crystallization can be obtained (Drzezdzon, Tziamtzi, Capitain). Also worth mentioning is the support of Thermogravimetric Analysis (TGA) in use with DSC. TGA allows for the measurement of mass as a function of time or temperature. This is important to know prior to DSC methods as it can reveal if the designated sample shows decomposition as this can be harmful to the DSC instrument as well as affect the results. Moreover, TGA can also be used in conjunction with DSC for a more thorough investigation of the sample (Schindler).

If defined by their mechanisms of operation, DSC can be divided into two main types, heat-flux, and power-compensated DSCs. DSC is performed by placing a sample in a high thermal conductivity (usually aluminum) DSC pan and comparing the heat flowing to it to an empty DSC pan that acts as a reference. For heat-flux DSC, the sample and reference pans are placed on a thermoelectric disk which is surrounded by the heating element. The chamber is then heated at a linear rate as a result of the heat being transferred to the sample and reference pan through a thermoelectric disk (Gill). Since one pan contains a

sample there will be a difference in the heat capacity ( $C_p$ ) and therefore a temperature difference between the reference and sample pans.

Figure 12 shows the experimental setup for DSC. With plots including the heat capacity of the sample pan, and reference. The reference pan heat capacity is then subtracted from the sample heat capacity which yields the heat capacity with respect to temperature of only the sample. Figure 12 is of a heat flux DSC; this can be distinguished from the single heating chamber. A power compensated DSC would include individual heating elements for each of the pans, sample, and reference.

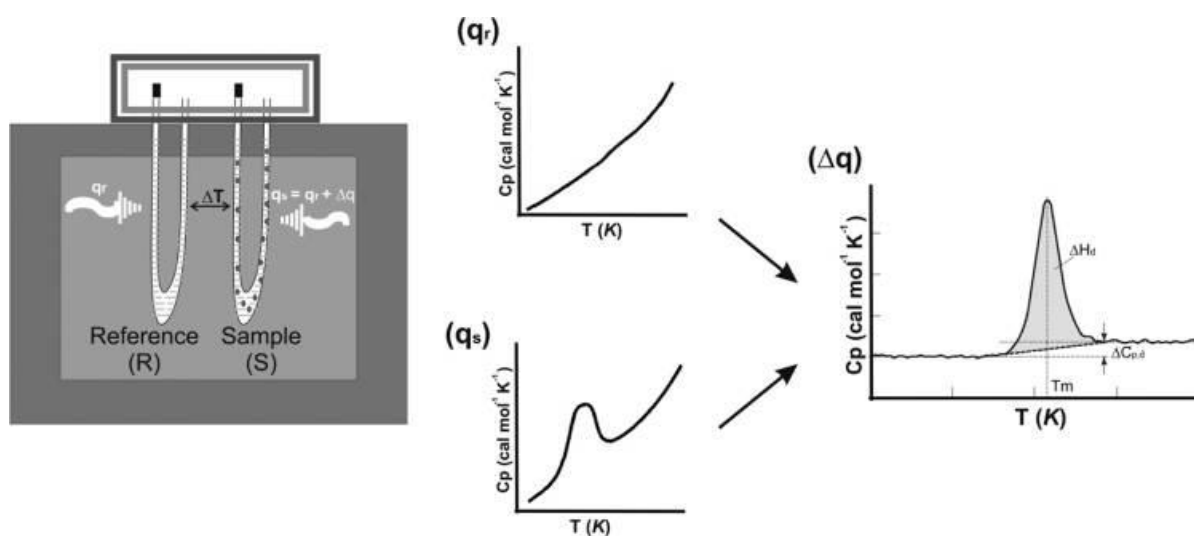


Figure 12: Instrument setup for a DSC (heat flux) experiment, Figures to right represent heat capacity measured from reference, and sample, then the final result through the combination of the measurements (Gill)

The temperature for each pan is measured with a thermocouple and the heat flow is calculated from the difference in temperature using the thermal equivalent of Ohm's law as shown in Equation 1.

Power compensated DSC requires the sample pan, and the reference pan, to be placed in separated heating elements. The sample and the reference pan are then held at the same temperature and the difference in the thermal energy required to hold them at the temperature is recorded as a function of time or temperature (Gill).

$$q = \frac{\Delta T}{R}$$

1

### 2.5.2 Rheology:

Rheology is the study of the flow of matter due to external forces as well as the deformation of material. Rheology is a well-established and wide area of study for a variety of materials. In this section the discussion will be directed to focus on polymer rheology (Sangroniz, Rueda).

There are many different ways to measure flow, the most common way being to calculate the apparent viscosity which is shown in Equation 2. Where  $\eta$  is the viscosity,  $\tau$  is the stress, and  $\dot{\gamma}$  is the strain rate. Shown in Figure 13 are the types of rheological behaviors of materials, showing how each trend reacts with respect to stress and strain (Ramachandran, Oswald).

$$\eta = \frac{\tau}{\dot{\gamma}}$$

2

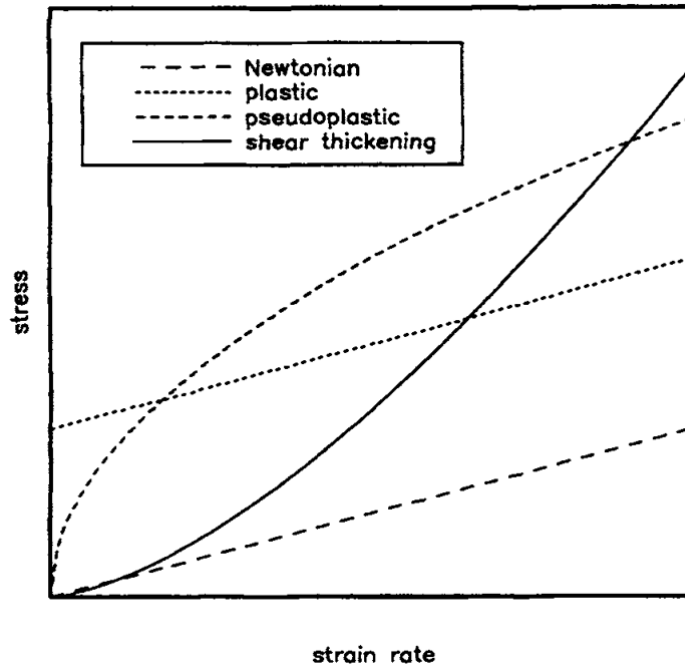


Figure 13: Types of rheological behavior (Ramachandran)

There are many ways to describe viscosity which revolve around different measurements taken to acquire it. A common procedure to capture the viscosity of a polymer is to use a rheometer, which yields a complex viscosity value. A rheometer functions by applying a stress to the material in the form of an oscillating piece in the upper geometry, and measuring the strain when the force is applied, shown in Figure 14. The lower portion of the instrument is stationary and typically contains a heating element such as a Peltier plate (Oswald).

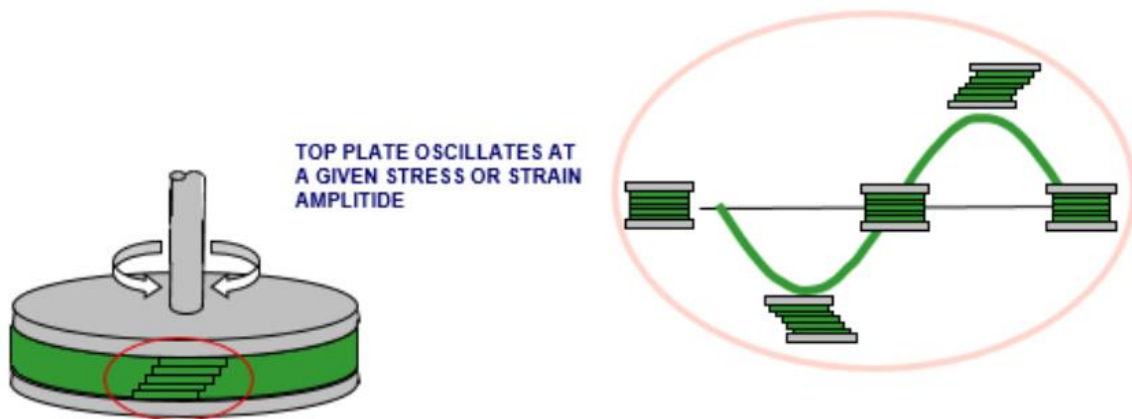


Figure 14: A sample loaded between a parallel plate geometry along with an oscillatory shear profile (Strasser)

The information typically obtained through this procedure comes in the form of a storage and loss modulus. Knowing the storage and loss modulus allows the calculation of the complex modulus. Equation 3 shows the formula for complex modulus using the storage ( $G'$ ) and loss modulus ( $G''$ ).

$$G^* = G' + i * G'' \quad 3$$

The storage and loss modulus both represent physical properties of the material. The storage modulus ( $G'$ ) represents the capability of the material to store energy, and the loss modulus ( $G''$ ) represents the energy loss of the material. A simplified way to look at it is that the storage modulus represents the degree to which a material behaves as a solid and the loss modulus represents the degree to which the material behavior is liquid-like. This can be seen when each value is taken to an extreme. When storage modulus is dominant the material is more solid-like in terms of its behavior and if the loss modulus is dominant the material is more liquid-like (Osswald, Ramachandran). Knowing the storage and loss modulus allows for the calculation of the complex viscosity which is shown in Equation 4.

$$\eta^* = \frac{G^*}{\omega}$$

4

$\eta^*$  Represents the complex viscosity of the material, and  $\omega$  represents the angular frequency of the upper rotating geometry part (Osswald).

## 2.6 Curing Kinetics of Adhesives:

### 2.6.1 Kinetic models:

ACAs require a high level of accuracy for a consistent and usable product. For Ztach, the material conducts through columns that are magnetically formed during the curing process and subsequently cured in-place. Just like other methods for ACAs, this gap has to be correctly spaced across the entire contact area, else the components may experience an inconsistent resistance which can cause a multitude of issues.

When using a curing material in a large-scale production, the material must be well understood in order to create a method to properly utilize it: For the magnetically aligned ICA investigated in this study (Ztach), the curing process is very important as the increase in viscosity that occurs during polymerization must be timed properly to allow for particles to first align into columns. A common procedure to characterize a material is to perform a kinetic study on the reaction taking place. This is typically done by taking experimental data and fitting an equation that best represents the kinetics within the material.

Equation 5 shows the fundamental rate equation. This function can be used to directly model the reaction rate in terms of temperature (T), and cure conversion ( $\alpha$ ).  $d\alpha/dt$  represents the rate of cure,  $k(T)$  is the rate constant of the equation which is a function of temperature and  $f(\alpha)$  represents the model function which is dependent on the material being studied.

$$\frac{d\alpha}{dt} = k(T) * f(\alpha) \quad 5$$

The function  $k(T)$  is represented by the Arrhenius equation which is shown in Equation 6. Here  $A$  is the pre-exponential constant,  $E_a$  is the activation energy,  $R$  is the universal gas constant, and  $T$  is the temperature.

$$k(T) = A * \exp\left(-\frac{E_a}{RT}\right) \quad 6$$

Equation 7 shows the model function which is the two-parameter autocatalytic kinetic model advanced by Šesták Berggren (Šesták). The constant  $\alpha$  represents the normalized cure, and  $m$  and  $n$  represent the kinetic exponents which are factors relating to the amount of product and reactants present at any time during the course of the reaction. The kinetic exponents represent the reaction orders:  $m$  represents the reaction order of the autocatalytic effect, and  $n$  represents the main reaction order. This was the model chosen to best represent this material as this model is often used on many basic epoxies (Zhang, Zhongliang, Dominguez).

$$f(\alpha) = \alpha^m * (1 - \alpha)^n \quad 7$$

Before the application of the kinetic model, a standard unit must be applied to experimental data to define the degree of conversion ( $\alpha$ ). In the case of characterizing both rheological and DSC data, the degree of conversion ( $\alpha$ ) of the material must be first determined as this allows the application of kinetic modeling. Since DSC and rheology use fundamentally different methods of measuring data, the methods by which the degree of conversion,  $\alpha$ , is found also differs.

For the case of DSC, the heat flow of the sample is being measured. Knowing the total heat of the reaction and the total heat released at any point during the experiment allows the integration of heat flow to solve for the relative amount of heat released at any given time to that of the total heat of reaction. Since heat of reaction is a direct correlation to the amount of product created, we can solve for the degree of conversion using Equation 8. Here  $(\Delta H_p)_t$  is the heat released at time  $t$  and  $\Delta H_0$  is the total heat released in the reaction (Dominguez).

$$\alpha(t) = \frac{(\Delta H_p)_t}{\Delta H_0} \quad 8$$

The degree of conversion for rheology is applied in a similar manner to that described for DSC methods. To obtain the degree of conversion for rheology, the Arrhenius equation can be proposed to explain the dependence of the storage modulus on the temperature. This allows the assumption that the storage modulus is a good representation of the degree of conversion (Zhongliang, Vyazovkin [ICTAC]). Here the final value of the storage modulus and the storage modulus at any time can be used to determine the degree of conversion at any point during the course of the reaction. This is shown in Equation 9. For the numerator,  $G'(t)$  represents the value at any point and is subtracted from  $G'(\alpha=0)$  (i.e. the  $G'$  value at  $\alpha$  equals zero).

In the denominator,  $G'(\alpha=1)$  represents the final value of  $G'$  and this is subtracted from  $G'(\alpha=0)$ . (Zhongliang).

$$\alpha(t) = \frac{G'(t) - G'(\alpha = 0)}{G'(\alpha = 1) - G'(\alpha = 0)} \quad 9$$

### 2.6.2 Isothermal Methods:

For the experimental modeling of isothermal data, there are four main constants needed. The frequency factor, the activation energy, and the exponential constant  $m$  and  $n$ . Equation 10 shows the equation used to calculate the activation energy in an isothermal setting. Here a linear dependence of  $\ln(k)$  versus  $1/T$  is plotted which allows the activation energy to be determined using all temperatures experimental data was sampled at (Perez).

$$\ln[k] = \ln [A] - \frac{E_a}{RT} \quad 10$$

This equation is found by solving the fundamental rate equation to get the activation energy out of the exponential. This method requires multiple sets of data to calculate a single value of activation energy for all the plots. To plot the data sets, the value of  $k$  must be found so that the linear dependence can be complete. This can be done using a simplified version of the rate equation with  $k$  as its own constant; since temperature is constant, so is  $k$ . This allows the use of fitting software to find experimental values of  $k$ ,  $m$ ,

and  $n$ , which defines the relationship used in Equation 10. It is also observable that the y intercept of the above linear fit is the value of  $A$ , the frequency factor in  $k(T)$ .

With the activation energy solved, the constants left are  $m$  and  $n$ , the exponential constants. The final constants can be solved by using the same fitting software used before. This concludes the calculation of the final constants which can then be inserted into the final rate equation, Equation 11, for isothermal testing. An example plot of fitted isothermal data is shown in Figure 15.

$$\frac{d\alpha}{dt} = \exp\left(A + \left(-\frac{E_a}{RT}\right)\right) * (\alpha^m) * (1 - \alpha)^n \quad 11$$

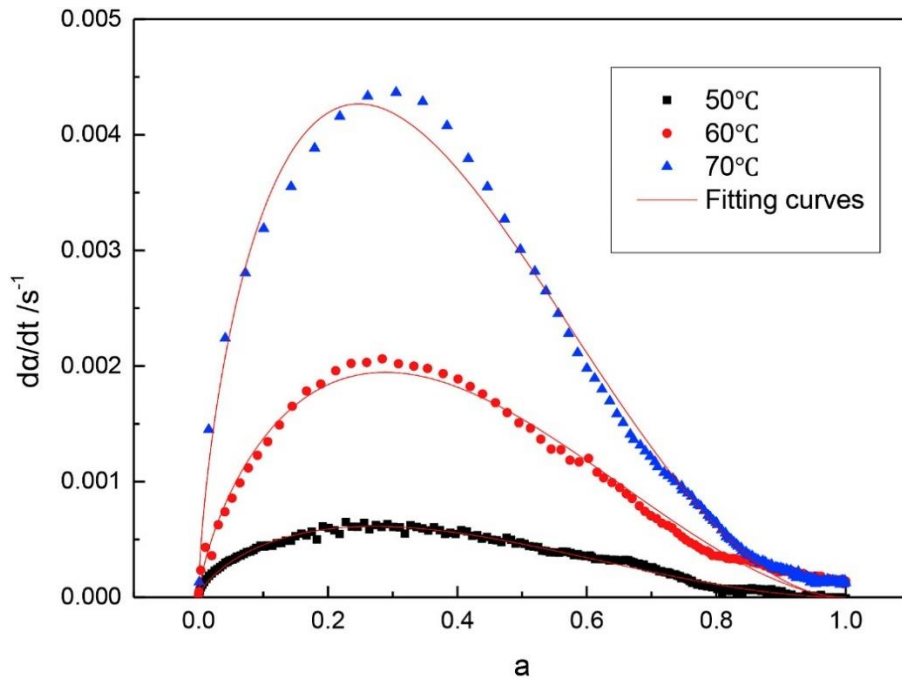


Figure 15: Example of experimental data fitted with the autocatalytic model at 50, 60, and 80°C (Zhongliang)

### 2.6.3 Non-isothermal Methods:

For non-isothermal methods, the first step of finding the activation energy is calculated using a different method. Since the previous method relied on  $k(T)$  being constant, as it applied to isothermal, the same method cannot be used for experimental data taken at a linear heating rate. To calculate the activation energy for non-isothermal data, the Kissinger-Akahira-Sunose (KAS) method can be used. To find the KAS equation the natural logarithm of the fundamental rate equation is taken to start. This is shown in Equation 12.

$$\ln \frac{d\alpha}{dt} = \ln [Af(\alpha)] - \frac{E_a}{RT} \quad 12$$

The Kissinger-Akahira-Sunose (KAS) method is utilized for the non-isothermal case and relies on a dependance between temperature and the logarithm of the rate of heating and the temperature squared as shown in Equation 13 (Akahira). Obtaining this equation requires integrating Equation 12 originally found from Equation 5, which is the fundamental rate equation with the activation energy taken out of the exponential in  $k(T)$ , with respect to temperature and changing the  $dT/dt$  relationship to  $\beta$  which represents the heating rate. Solving the rest of the integration results in this equation, which leaves some grouped constants and a function of  $\alpha$  as the y-intercept in this fit which can be ambiguous as this is a model free method: This method has no dependance on a function of alpha and could therefore be used with other models of  $\alpha$ . After, we are left with the constant of  $E_a/R$  times the variable  $T$ , temperature, which is the object of the KAS method. An example of this is shown in Figure 16 where each color represents a specific value of the degree of cure,  $\alpha$  (Zhang).

$$\ln \frac{\beta}{T^2} = \ln \frac{AR}{E} - \ln[g(\alpha)] - \frac{E_a}{RT}$$

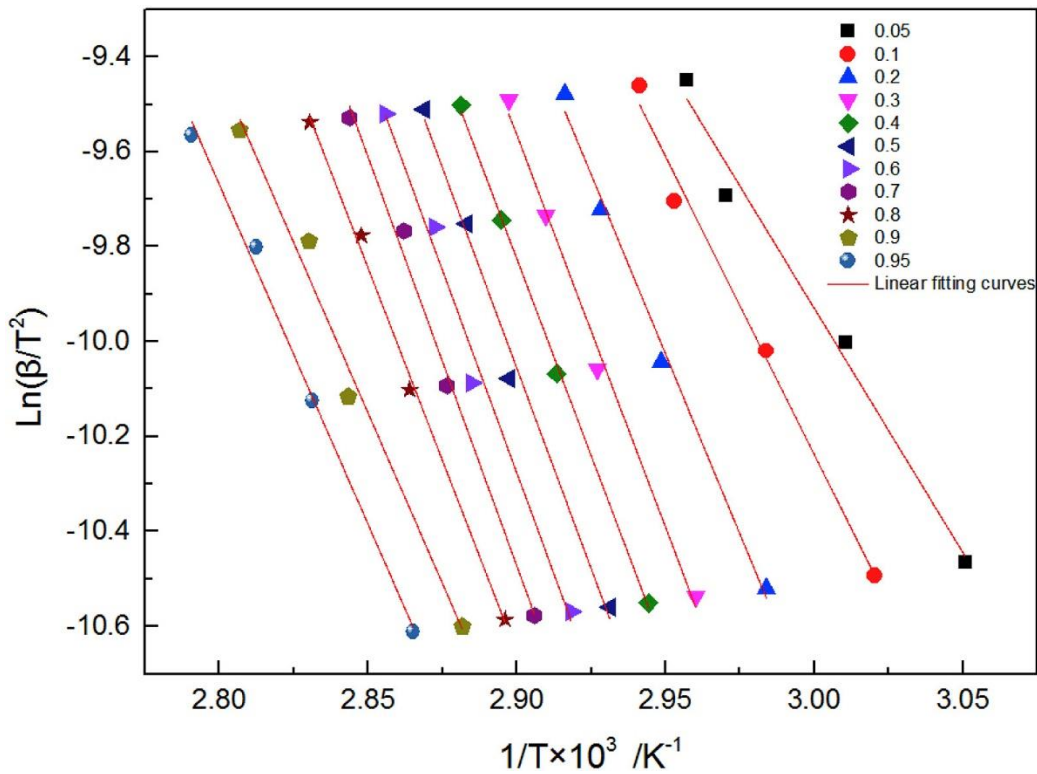


Figure 16: Example of KAS fitting to experimental data performed on an epoxy resin of  $\ln(\beta/T^2)$  versus  $1/T$  (Zhongliang)

Shown above is an example of the KAS method applied to non-isothermal data. The legend shows the respective point of  $\alpha$  for each type of data point. The lines of fit cross all the points where  $\alpha = x$ , where  $x$  is one of the cure conversions calculated picked from the legend. The slope of each of the linear fits represents the value of  $E_a$  at the designated point of  $\alpha$ . This can be used to find the  $E_a$  at any point in the cure if needed (Zhang).

With the activation energy found, the next constants to solve for are  $A$ ,  $m$ , and  $n$ . This can be done using Equation 14. This equation can be calculated using the logarithmic form of the fundamental rate

equation. This can be used for a linear fit using the known  $E_a$  to find the slope, which represents the value of  $n$ , and the y-intercept, which represents the value of  $\ln(A)$ . The value of  $m$  can subsequently be solved by using the value of  $n$  and the value of  $p$ . Where  $p = \frac{m}{n} = \frac{\alpha_m}{1-\alpha_m}$  and  $\alpha_m$  represents the maximum value of the rate of cure (Zhongliang). The constant  $p$  is a mathematical ratio between  $m$  and  $n$  that represents both the values in this compounded version of the fitting equation (Zhongliang)

$$\ln \left[ \frac{d\alpha}{dt} * \exp \left( \frac{E_a}{RT} \right) \right] = \ln A + n * \ln [\alpha^p (1 - \alpha)]$$

14

Once the  $m$ ,  $n$ , and  $A$  variables are found, Equation 11 could be used to make a fit to predict experimental data. An example of a fit using this method being applied is shown in Figure 17.

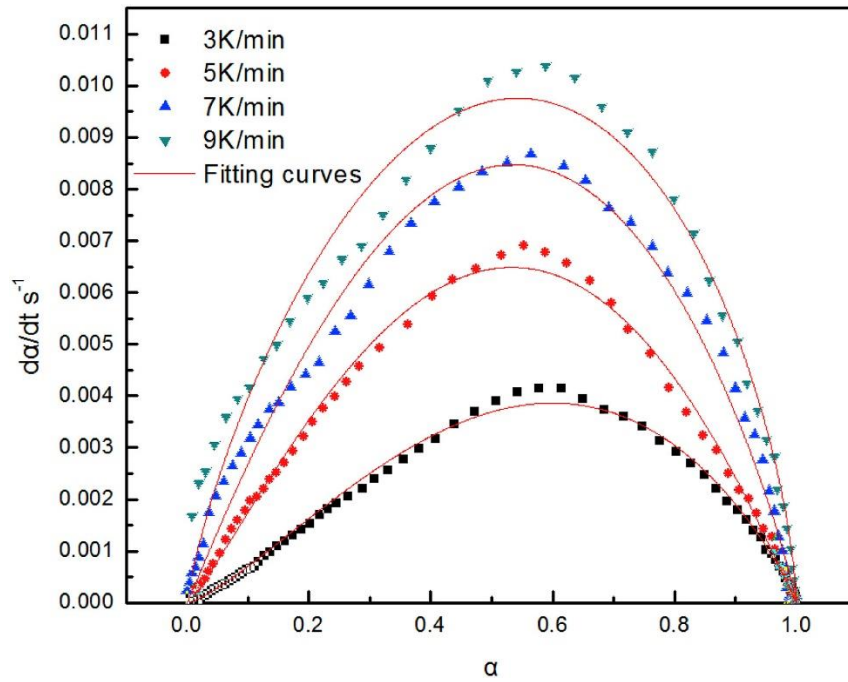


Figure 17: Example of fully complete fit on non-isothermal experimental data on an epoxy at 3, 5, 7, and 9°K/min (Zhongliang)

## Chapter 3: Experimental

### 3.1 Materials:

ZTACH® ACE (Anisotropic Conductive Epoxy) was supplied by Sunray Scientific (Eatontown, NJ) as a two-part system (i.e. filled prepolymer and hardener). Though this material formulation is proprietary, it generally consists of an epoxy prepolymer and magnetic, electrically conductive particles (~15wt%). According to the manufacturer, the optimal resin/hardener ratio is 5% hardener by weight of epoxy, and we applied this ratio for all of our work. Notably, work was performed using as-received materials with no additional purification. Mixing of resin and hardener was performed using a Flaktek centrifugal mixer (DAC 330-100 PRO) according to the following program: 2g of filled resin and 100mg of hardener was placed into a 10ml Flaktek mixing cup and hand mixed until homogeneous. The mixing cup was then placed into a Flaktek vacuum sealable mixing cup holder, and subsequently placed under 9 mm Hg vacuum using an Edwards High Vacuum Pump. Samples were then mixed for two minutes at 1250 RPM, while under vacuum. Following mixing, the stability of the resin system was evaluated using DSC. One sample of the material was used at varying times from mixing to show an insignificant amount of reaction, as shown in (Figure SI.8). Kinetics did not show an appreciable difference in enthalpy following 1.2 hours of curing. As such, the amount of time following mixing and rheology testing was held to <1 hour to ensure consistency of measurement.

### 3.2 Differential Scanning Calorimetry:

A TA instruments Discovery DSC2500 Differential Scanning Calorimeter was used in this investigation. Each experiment was performed using ~10 mg of sample, placed into a hermetically sealed aluminum DSC pan. Isothermal tests were performed by heating at 200C/min from room temperature to

the target isothermal temperature and holding for 20-50 minutes; such time was sufficient to capture the heat released during crosslinking as indicated by a return to a stable baseline. Isothermal experiments were conducted at 70, 80, and 90°C. Non-isothermal experiments were conducted by heating from 23°C to 200°C at rates of 5, 10, 20 and 30°C/min. All tests were performed in triplicate.

Curve fitting to determine kinetic constants was performed using the MATLAB R2019b curve-fitting app, as well as built in functionalities within a Python 3 shell. Thermal Gravimetric Analysis was performed prior to DSC on a TA instruments Discovery TGA5500 to confirm no significant weight loss had occurred over the investigated temperature range (Figure SI.9).

### 3.3 Rheology:

A TA instruments Discovery DHR-2 rheometer equipped with an advanced Peltier plate was used in this investigation. 20mm aluminum upper and lower disposable plates were used, shown in Figure 18. TRIOS (v5.6.0.87) software (TA instruments) was used to control the rheometer, synchronize the temperature control, collect data, and analyze results. Curve fitting to determine kinetic constants was performed using the MATLAB R2019b curve-fitting app, as well as built in functionalities within a Python 3 shell.

To conduct rheological measurements, a slight excess of pre-mixed material was placed onto the lower disposable geometry. The 20mm upper disposable geometry was slowly lowered to the gap size (500 $\mu$ m) and excess material squeezed from the gap was removed using a Kimwipe prior to measurement. Oscillatory strain measurements were carried out at a frequency of 1Hz. Large changes in viscosity observed during rheological experiments necessitated the use of auto-strain adjustment: In these experiments, strain varied from 5-80% for the uncured material, to about 0.06% for cured materials. Linear viscoelasticity was confirmed as a representative material in both the uncured and cured states by

performing a strain amplitude test (Figure SI.11). The program used for the instrument was set to target a strain of 0.1%, with a frequency of 1Hz. Because curing occurs rapidly, a fast-sampling strategy (2 points  $s^{-1}$ ) was employed. Note that frequency and sampling rate are two distinct parameters, one relating to how fast the data is being taken, the other relating to the instrumental rotation speed parameter. The applied normal force was maintained at 0N with a high sensitivity, 0.1N, this allowed for a measurement of dynamic shrinkage during cure. Isothermal tests were performed by heating at  $\sim 60^{\circ}\text{C}/\text{min}$  from room temperature to the target isothermal temperature and holding for 20-50 minutes; such time was sufficient to allow for restabilization of the baseline following curing. Isothermal experiments were conducted at temperatures of 70, 80, and  $90^{\circ}\text{C}$ . Non-isothermal experiments were conducted by heating from  $23^{\circ}\text{C}$  to  $200^{\circ}\text{C}$  at rates of 5, 10, 20 and  $30^{\circ}\text{C}/\text{min}$ . For a more in-depth section on the progression of building a working rheological procedure for this material, see Appendix Figure SI.10. As with DSC experiments, all rheology experiments were performed in triplicate.

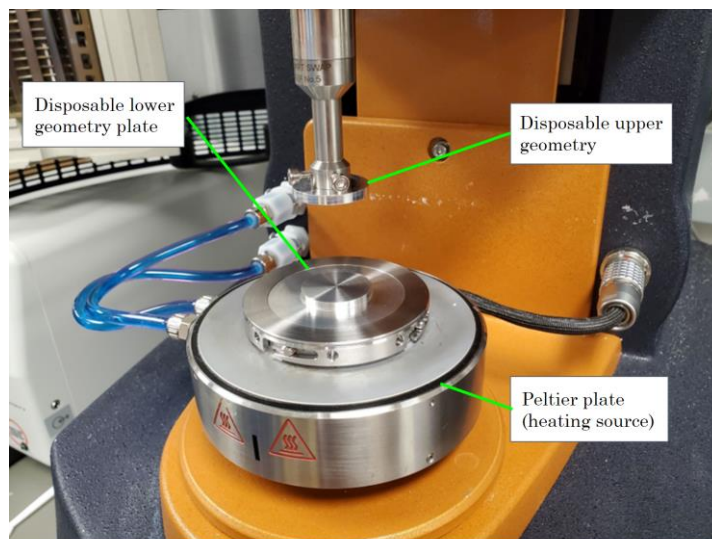


Figure 18: Rheology instrument with disposable upper and lower geometry

## Chapter 4: Results and Discussion

### 4.1 Isothermal Behavior-DSC:

Shown in Figure 19 are representative DSC curves for the ACA taken at three isothermal temperatures ( $T_{\text{iso}}$ ): 70, 80, and 90°C. Notably, two peaks are observed in this experiment: a small peak at shorter times and a larger peak at longer times. The peak heat flow changes with the chosen temperature of the isothermal run. Studies were performed on the base material without catalyst, as well as empty hermetically sealed DSC pans. Results showed the initial peak is not an inherent system response and therefore leads us to conclude that it is materials related (See Figures SI.1 and SI.2 for details).

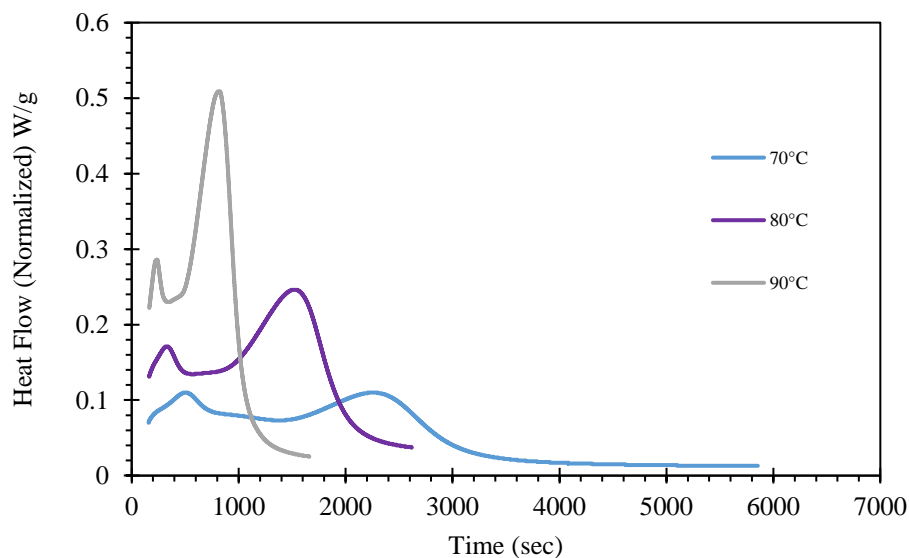


Figure 19: Isothermal DSC data at 70, 80, and 90°C for the ACA with respect to normalized heat flow

Because the material is proprietary, we are not able to determine the cause of this initial peak. For the intention of applying a kinetic study method on this material, only the second larger peak was used to

represent the epoxy curing reaction and we justify this choice as the area under the first peak is quite small compared to that of the second peak (<7%).

The enthalpy, which is the main reaction peak integration, increases with increasing isothermal temperature. The total reaction time decreases with increasing temperature indicating that the rate of reaction is faster at elevated temperature. The total enthalpy, as determined by integrating each main reaction peak, was found to be about 92.99 +/- 26.79 J/g (see Table 1). As such, the enthalpy of reaction is more consistent at higher temps, notable at 80 and 90°C.

The data was more consistent at the higher temperatures of 80 and 90°C as compared to data taken at 70°C (Table 2). The ratio of first peak enthalpy versus second peak enthalpy is also different for each temperature range, mentioned before to be (<7%). The trend here shows that the higher the temperature, the smaller the ratio between the first and second peak enthalpies. Knowing the enthalpies at 70°C are much lower than that of 80 and 90°C, the assumption could be made that isothermal runs at 70°C is that the material may not reached full conversion, or that the initial peak observed has a larger impact than predicted.

Table 2: Characteristics of DSC isothermal data

Temperature °C	reaction start (mins)	reaction end (mins)	first peak time (mins)	second peak time (mins)	first peak enthalpy (J/g)	second peak enthalpy (J/g)
70	22 ± 4	61 ± 7	8.2 ± 0.7	41 ± 4	6.7 ± 1	58 ± 4
80	12 ± 0.6	36 ± 0.3	5.8 ± 0.3	26 ± 0.4	5.2 ± 0.5	100 ± 6
90	6.4 ± 0.1	19 ± 1	3.7 ± 0.3	13 ± 0.3	2.4 ± 0.4	120 ± 5

The heat flow measured from a sample of ACA taken at  $T_{iso}=90^{\circ}\text{C}$  is shown in Figure 20. Plotted in the same figure is the running integral of the enthalpy, which can be normalized to find the relative degree of conversion (see Figures SI.4 showing details of DSC integrations). The rate of reaction can be measured by using this running integral, which in turn can be used to determine the degree of conversion ( $\alpha$ ). The

degree of conversion allows for the calculation of a  $d\alpha/dt$  curve, which is the experimental data used to determine the kinetic parameters,  $k$ ,  $m$ , and  $n$  as described in Equation 7.

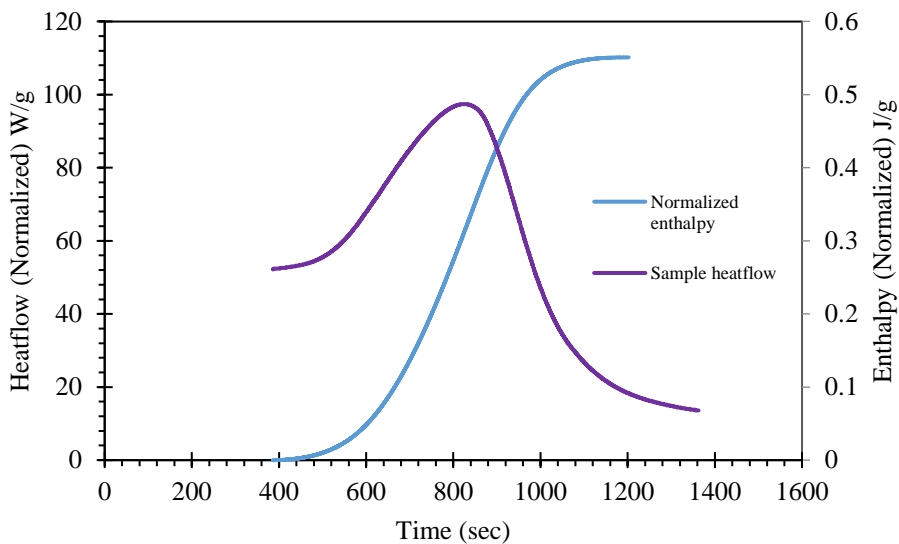


Figure 20: Example of how DSC results are normalized for fitting process, shown on 90C isothermal cure example

The normalized enthalpy curve, showing  $\alpha(t)$ , is represented in Figure 21. As expected, the curve exhibits a qualitatively similar shape to that of the running integral presented in Figure 20 except that in this case, values range between 0 and 1. As shown in Table 2, the enthalpies for each isothermal temperature differ. Normalizing the experimental data within each set of data allows for a standardized format in which a kinetic model can be applied. With the data being normalized, it allows all the data to universally be applicable to the method that allows for the calculation of a  $d\alpha/dt$  curve.

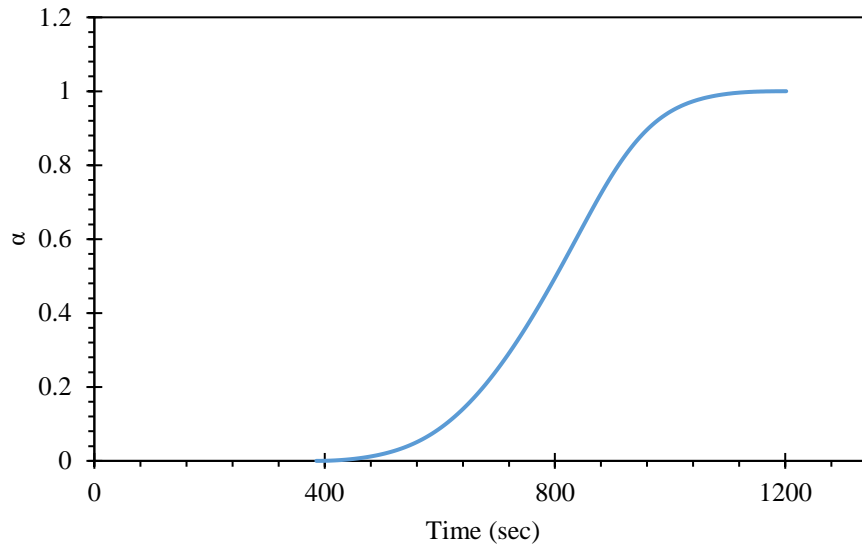


Figure 21: Evolution of the degree of conversion with respect to time, at 80°C

$d\alpha/dt$  is plotted as a function of the relative degree of conversion ( $\alpha$ ) for all three isothermal temperatures (Figure 22). As shown, the maximum rate values are dependent on the isothermal temperature; for example, a peak in the y-axis,  $d\alpha/dt (T_{iso}=90^{\circ}\text{C}) = 0.003 \text{ s}^{-1}$  whereas at  $70^{\circ}\text{C}$  the value of  $d\alpha/dt$  drops to less than  $0.001 \text{ s}^{-1}$ . This is coherent with the data found in Table 2, where the total time of each isothermal temperature decreases with increasing temperature. The larger the area under the curve, the shorter the reaction is. Simplified, the longer a higher rate is sustained, the shorter the reaction will be. It can also be seen that the value of  $\alpha$  where each of the  $d\alpha/dt$  peaks occur shifts slightly depending on the temperature of the experiment. This could be attributed to the dispersion of thermal energy throughout the experiment, both in sample and instrument. The quicker the total reaction time, the less time the rate of reaction has to reach its peak rate. The rates at the beginning and end of the reaction both converge to zero, as the slope of the normalized  $\alpha$  shown in Figure 21 approaches zero.

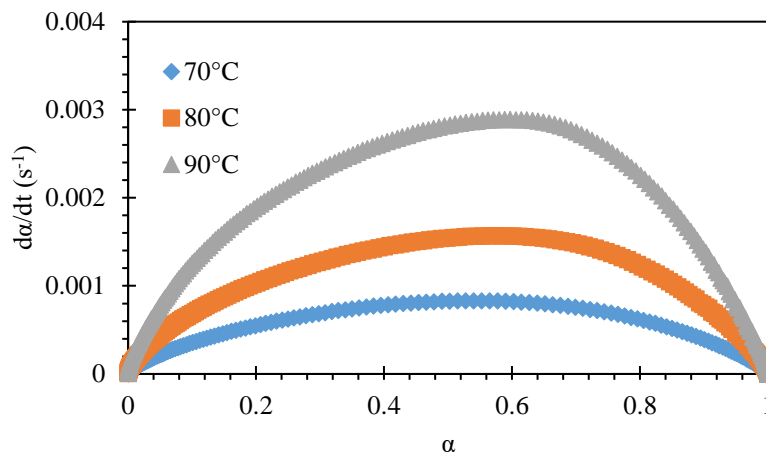


Figure 22: DSC isothermal rate of cure during reaction versus the degree of conversion for three isothermal temperatures. Note that the maximum rate of reaction increased with increasing isothermal temperature.

Experimental data was fitted to Equations 5, 6, and 7 to determine the rate constant,  $k$  and the reaction coefficients  $m$  and  $n$ . Fits to the three-parameter model was performed on experimental data using MATLAB (Table 3). As shown, the values of  $m$  and  $n$  are nearly constant over the temperature range investigated as indicated by a coefficient of variation of less than 5%. After this initial fit is performed,  $m$  and  $n$  are averaged and held constant as values since the theoretical values of  $m$  and  $n$  are static. Since  $m$  and  $n$  represent the ratios of product and reactant used, these should stay constant over heating rates as they're no temperature dependent (Zhongliang, Zhang). For this instance of applying the fundamental rate equation the values are held constant to allow for a final fit where the only variable is temperature. In Figure 23, these values are applied to a fit on experimental data with a regression of 0.98.

Table 3: Isothermal DSC initial fit constants

Isothermal Temp (°C)	$k^* 10^3 (s^{-1})$	m	n
70	$2.5 \pm 0.4$	$0.76 \pm 0.04$	$0.72 \pm 0.01$
80	$4.2 \pm 0.2$	$0.78 \pm 0.01$	$0.69 \pm 0.006$
90	$8.6 \pm 0.3$	$0.8 \pm 0.02$	$0.71 \pm 0.02$
Average	$5.1 \pm 3.0$	$0.78 \pm 0.03$	$0.71 \pm 0.02$

The fit used on experimental data shown in Figure 23 has a high regression, which leads to the assumption that the procedure up to now has accurately predicted the experimental data. To further the accuracy of this fit, the remaining constants can be solved for to give a more complete analysis with regard to the final fit for this material. The activation energy ( $E_a$ ) is then determined using the constant values of m and n, found prior, to collect a set of values of k. The values of k found with the constant values are shown in Table 4, with the values of m and n used from Table 3. The values of k are found to increase with temperature which is expected behavior from the rate equation.

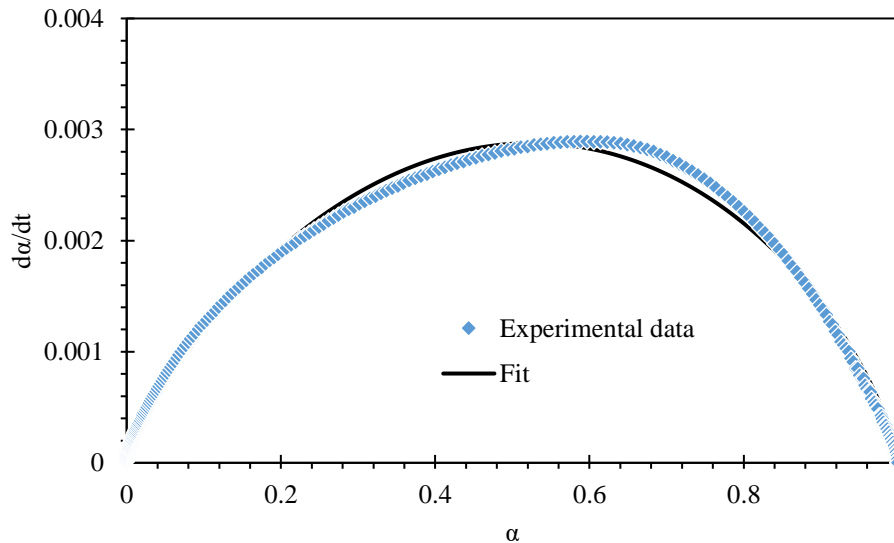


Figure 23: Experimental fit using parameters for  $E_a$  calculation at 80°C

The values found in Table 4 for k can then be used to find the activation energy by applying them to Equation 10. This allows for the plotting of a linear relationship between  $\ln(k)$  and  $1/T$  shown in Figure 24. With this relationship, the slope of the line is the activation energy divided by the universal gas constant (R), and the y-intercept of the line is the value of the frequency factor A from the Arrhenius equation.

During optimization it was found that when the non-constant values of m and n were averaged and plotted, the results showed a non-linear relationship and therefore was not the best representation of this relationship, hence the current method was used.

Table 4: k, m, and n values used in  $E_a$  calculation for isothermal DSC fit procedure

Isothermal Temp (°C)	k (s <sup>-1</sup> )	m (held constant)	n (held constant)
70	0.0026 ± 0.0005	0.78	0.71
80	0.0043 ± 0.0001	0.78	0.71
90	0.0084 ± 0.0005	0.78	0.71

The fit used on experimental data shown in Figure 23 has a high regression, which leads to the assumption that the procedure up to now has accurately predicted the experimental data. To further the accuracy of this fit, the remaining constants can be solved for to give a more complete analysis with regard to the final fit for this material. The activation energy ( $E_a$ ) is then determined using the constant values of m and n, found prior, to collect a set of values of k. The values of k found with the constant values are shown in Table 4, with the values of m and n used from Table 3. The values of k are found to increase with temperature which is expected behavior from the rate equation.

Each point in Figure 24 represents a value obtained from three experimental runs used to solve for the slope,  $E_a$ . The regression of the linear fit is 0.99, with a final  $E_a$  value of 61,465 J/mol. As mentioned before, this linear fit also yields the value for A as well. While this value of A could be used, the value of A was instead calculated using the curve optimizer to obtain the most accurate value, as well as to compare

whether the method of constant m and n values was justified when compared to the value of A that was found using the linear fit.

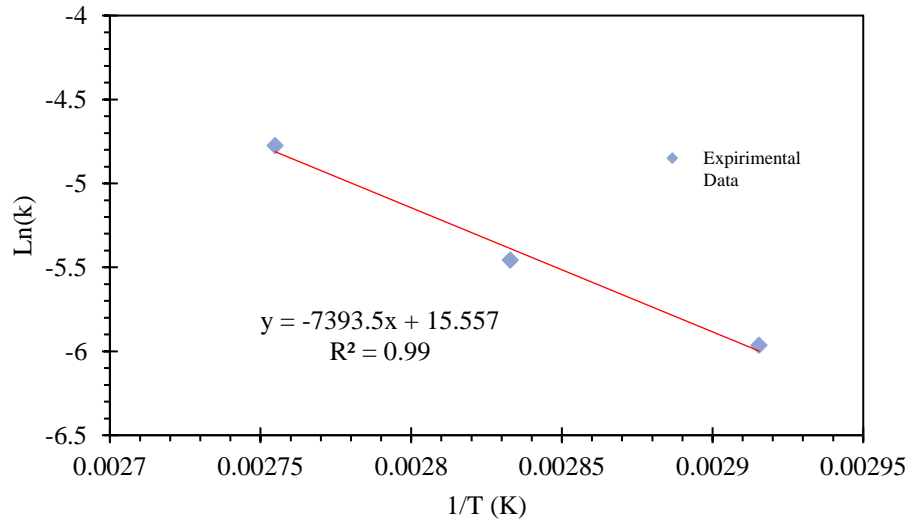


Figure 24: DSC Isothermal Activation calculation,  $\ln(k)$  versus  $1/T$  using the relationship from Equation 10

To find the value of A using this method, all other values found were applied to the fitting formula in the fitting software. Knowing the activation energy, the same constant m and n values that were used while solving for the activation energy, can be used to determine A, the frequency factor / pre-exponential constant in the Arrhenius equation, which represents the frequency of reactions in the material. This was fitted using the MATLAB curve fitter with results shown in Table 5 and the final predictive equation as shown in Equation 14.

The values shown for A found through the fitting software show very low variation when compared by temperature, which is congruent with the Arrhenius equation as its dependent on temperature, these values should logically be identical. The fitted values of A also align very well with the value of A calculated through the linear fit when solving for the activation energy shown in Figure 24.

Table 5: Isothermal DSC final fit equation values (m=0.78, n=0.71)

Isothermal Temp (°C)	A(optimized)	m (held constant)	n (held constant)	Regressions
<b>70</b>	<b>15.59 ± 0.047</b>	<b>0.78</b>	<b>0.71</b>	<b>0.96 ± 0.04</b>
<b>80</b>	<b>15.48 ± 0.023</b>	<b>0.78</b>	<b>0.71</b>	<b>0.98 ± 0.008</b>
<b>90</b>	<b>15.57 ± 0.17</b>	<b>0.78</b>	<b>0.71</b>	<b>0.99 ± 0.006</b>
<b>Final Average Values</b>	<b>15.55 ± 0.10</b>	<b>0.78</b>	<b>0.71</b>	<b>0.98 ± 0.02</b>

The final fit equation shown in Equation 14 is the formula used to predict the kinetic behavior of the material with dependence on temperature. With a known isothermal temperature, the characteristics of the kinetic behavior can be compared to the experimentally collected data to measure goodness of fit. An example of the final fit equation being applied to experimental data is shown in Figure 25.

$$\frac{d\alpha}{dt} = \exp\left(15.55 + \left(-\frac{61465}{RT}\right)\right) * (\alpha^{0.78}) * (1 - \alpha)^{0.71} \quad 15$$

Using Equation 14 allows for the prediction of the rate of reaction versus cure conversion at a given isothermal temperature. This is demonstrated in Figure 25 for  $T_{iso}=90^{\circ}\text{C}$ , where good agreement between the prediction and experimental data is obtained ( $R^2= 0.987$ ). It is not surprising that the fitting using isothermal data gathered from DSC yielded good results. The thermal lag between the instrument and sample is very low which allows for an accurate study of the reaction taking place. The slight skew in the data near the maximum is hypothesized to result from the poor ability to capture and predict a reaction during the portion of cure where rates are at their maximum. Another possibility is related to the difference in enthalpies of the reactions. There is the possibility of the lower temperatures not fully capturing a reaction where the cure conversion was near 100%, however this seems less likely as the fit would show a much greater difference in experimental data and the predicted fit.

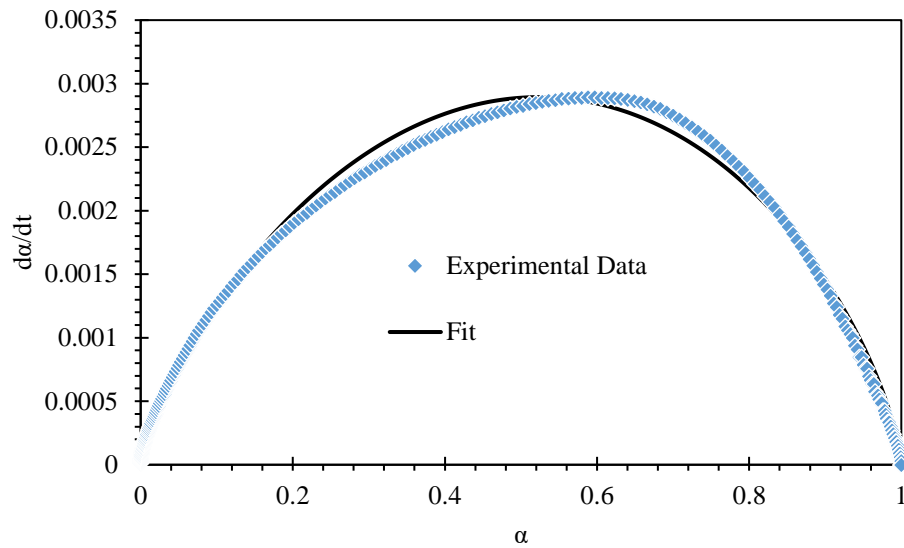


Figure 25: DSC 90 °C Isothermal fit on experimental data using Equation 5

This predicted fit equation shows regressions well into the 0.90s, which leads to the conclusion that the fitting equation and method are a successful way to measure and characterize the material. For more information on final fit values, see Table SI.5.

## 4.2 Isothermal Behavior-Rheology:

Shown in Figure 26 is an example of experimental isothermal curing data acquired using a parallel plate rheometer for  $T_{\text{iso}}=80^{\circ}\text{C}$ . Storage modulus and Loss modulus ( $G'$  and  $G''$ ) as a function of isothermal hold time are shown. From these two parameters complex viscosity ( $G^*$ ) can be calculated using Equation 3. A few important material properties worth noting including induction time, gelation time and total cure time. Induction time is the elapsed time from the achievement of isothermal conditions to the time that the material starts to cure (in this case indicated by a change of 0.01% from the minima change in  $G'$ ). Gelation time is the time when the storage and loss modulus are equal and thus indicates the elapsed time (not including the induction time) when the material transforms from a liquid to a solid. Finally, total cure time is the time required for the sample to be fully cured starting from the induction time. Some key parameters are noted in Table 6. Comparing values of induction time, end of reaction, and time to gelation, the experimental runs show good consistency within their own isothermal temperature sets.

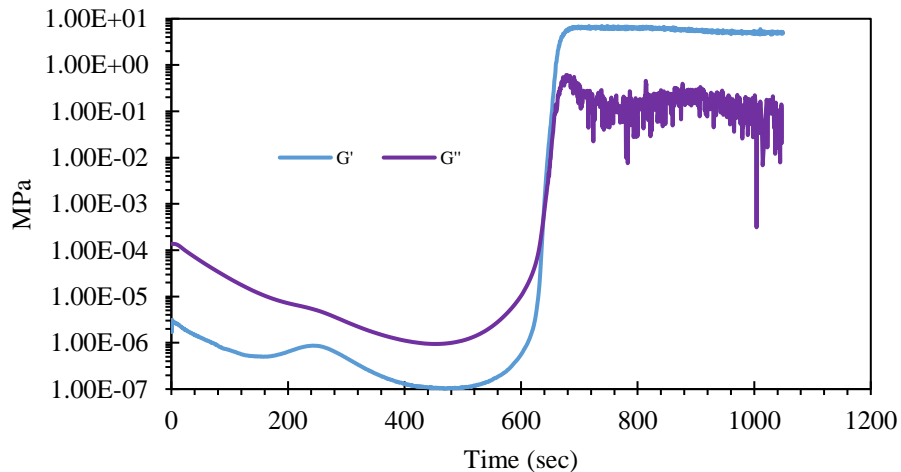


Figure 26: Example of Storage and Loss modulus through a sample of rheological data for ACA at  $80^{\circ}\text{C}$

An identical reaction of small pre-cure peak is notable in the beginning of the experiment, comparable to that observed under isothermal DSC conditions; this confirms our prior explanation that there is some small amount of an initial reaction at the onset of the isothermal experiment. An important factor to note, all data collected from rheology was first treated using a Savitzky-Golay filter for the purpose of minimizing noise in the experimental data prior to analysis (see Figures SI.6 and SI.7 for details). Through characterization of this filter, it was found that no significant changes in data positioning or characteristics were found.

Table 6: Characteristics of isothermal rheological data

Temperature °C	reaction induction time (mins)	reaction end (mins)	gelation time (mins)	final viscosity (MPa·s)
70	8.8 ± 1	78 ± 3	67 ± 4	1.7 ± 0.6
80	6.8 ± 0.6	41 ± 1	34 ± 1	1.1 ± 0.03
90	4.4 ± 0.2	25 ± 1	20 ± 0.9	1.1 ± 0.09

In Figure 27, the time it takes to both start and end the reaction decreases with increased isothermal temperature. The same is noted for the time to gelation, which is calculated by finding the time at which the storage ( $G'$ ) and loss modulus ( $G''$ ) cross. For example, gelation takes about 65 minutes at 70°C, but decreases to only about 20 minutes at 90°C, thus indicating a much faster reaction at elevated temperatures. The induction time decreases by nearly a factor of two when increasing the temperature from 70 to 90°C and likewise the total reaction time is greatly shortened from about 77 minutes to about 25 minutes over the same temperature comparison. It is also notable that the relationship between temperature and rate of

cure, as well as time to cure, is not linear as is visible in Figure 27. For a given increase in isothermal curing temperature (eg: 70°C to 80°C), the total cure time does not decrease at a constant rate for steps of 10°C.

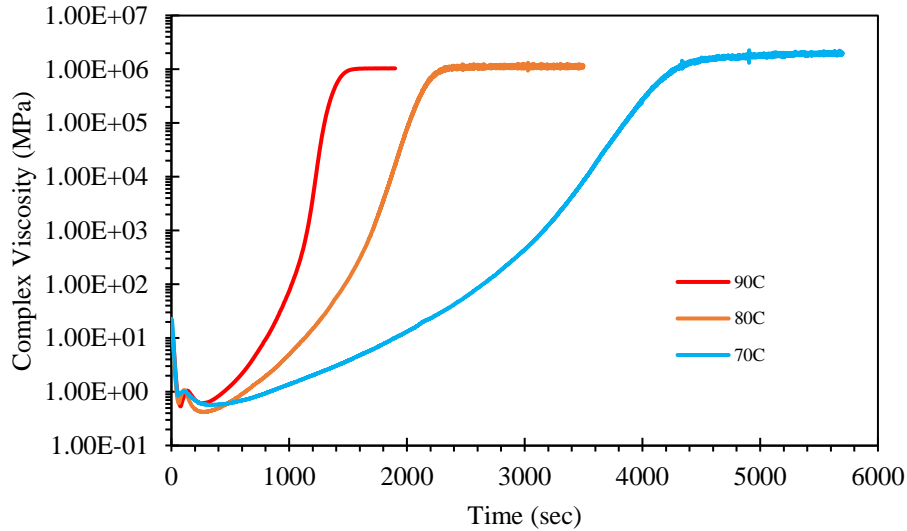


Figure 27: Isothermal Rheology, data sets for 70, 80, and 90C

A common issue with epoxies is that the final viscosity depends on the temperature that the material is cured. When the epoxy cures, the hardening of the material causes an increase in  $T_g$  and consequently a reduction in molecular mobility. In turn, this can result in a reduction in the total degree of conversion. This becomes particularly important at lower temperatures. This is not observed in this material as shown by the final viscosities in Table 6 with the exception of the final viscosity values for 70°C. This discrepancy in viscosity could be explained by the higher variability at the lower temperatures which causes a larger value for final viscosity. This is difficult to notice in Figure 27 as it has a logarithmic y-axis. The values of viscosity stay nearly constant with the lowest temperature having a slightly higher viscosity likely due to a result in a slower curing temperature.

To determine the final fit equation, a similar method to the DSC procedure was used, except that  $\alpha$  is determined using storage modulus signal instead of enthalpy (Equation 9). The Arrhenius equation can be used to explain the dependence of the temperature on the storage modulus; the storage modulus can be directly linked to the amount of crosslinking achieved and therefore be related to the cure conversion (Zhongliang, Vyazovkin [ICTAC], Dominguez).

Figure 28 shows the normalized cure conversion calculated using Equation 9. The storage modulus is shown to be a good representation of the cure conversion as its characteristics while curing compare well to the cure conversion found through DSC results. This method is applied to all experimental data taken to allow for a unified method on normalized data to proceed with the calculation of the fitting equation.

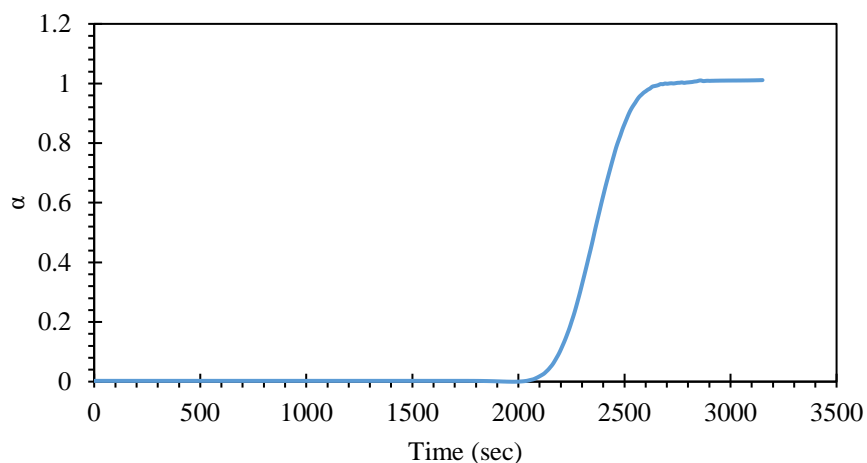


Figure 28: Rheological isothermal evolution of cure conversion with respect to time, 80°C

Shown in Figure 29 is the time derivative plot of the same normalized curve of alpha with all three temperatures shown. As with DSC, the rate increases from an initial value of zero to a maximum near a value of  $\alpha=0.5$ . Likewise, the rate increases markedly with each increment in temperature. A noticeable difference between the rheological and DSC curves is the resolution of the data, particularly when the rate of reaction is at its maximum. This is due to the different data sampling rates available between DSC (~10

points/second) and the rheological technique ( $\sim 2$  points/second). As with DSC, the derivative of the normalized curve of alpha was used to calculate kinetic parameters using an initial fit.

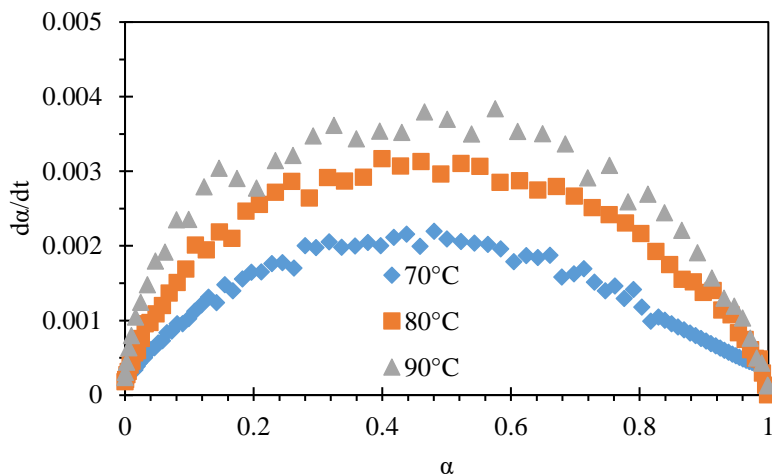


Figure 29: Rheological isothermal rate of cure during reaction versus the degree of conversion: three example runs of experimental data at the three designated isothermal temperatures

Another notable characteristic is the precision of the data. The experimental  $d\alpha/dt$  curves show what could be described as oscillations. This is especially true for experimental results taken at  $90^\circ\text{C}$ . This is related to the method the rheometer uses to collect data. The rheometer must keep a very precise strain percent value to obtain data that is accurate, an issue with this being that the optimal strain value during a curing changes drastically as well as dynamically. Due to the nature of a rheological study on a material that changes viscoelastic properties under procedure, the low force required to gather consistent results over the entire curing process shows more fluctuation during the experiment. This leads to the raw output data being much more sporadic than desired. This is combated mostly by the Savitzky-Golay filter applied to the data, but the result still shows some oscillations.

Figure 30 shows an initial fit to an experimental data set taken at 90°C. This was done using Equations 5, 6, and 7. The regression of the fit is considered good with a value of 0.97. The regression values were good over all runs at all three isothermal temperatures with a range of 0.9 – 0.98. Since no values were normalized, they each acquire their own set of independent variables that yield an extremely accurate fit.

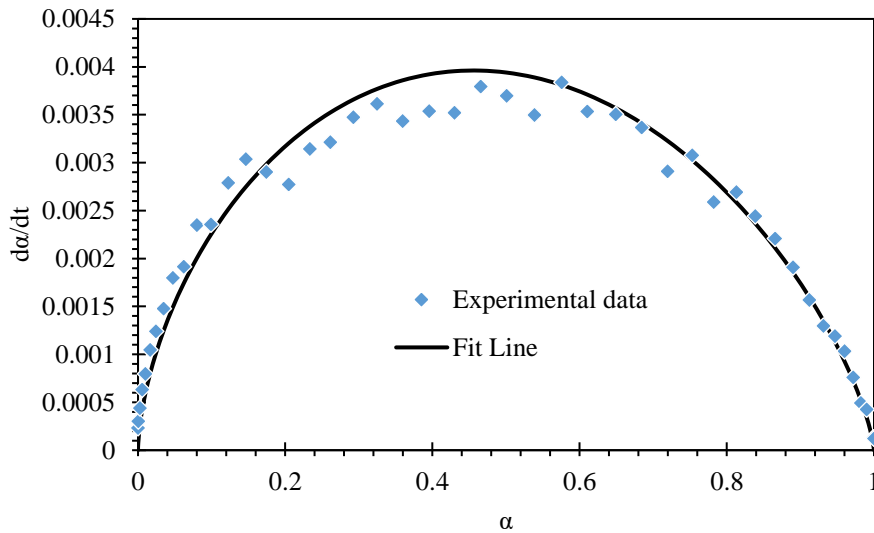


Figure 30: An initial fit of rheology data at 90°C: parameters optimized are shown in Table 7 with a regression of 0.97

The data shown in Table 7 represents the initial fitting of the rheological isothermal data with  $k$ ,  $m$ , and  $n$  using Equations 5, 6, and 7. The values of  $k$  shown should in theory increase with an increasing isothermal temperature. However, the values of  $k$  at 70, 80, and 90°C don't conform to this. This is due to the slight differences in each experiment when capturing multiple runs for each isothermal temperature. When the rate of cure differs slightly, it can drastically change the values which represent the shape of the  $d\alpha/dt$  curve and in turn influence the values of  $k$ ,  $m$  and  $n$ . Simplifying each variable: the  $k$  variable, which represents the number of reactions per second can be thought of as the amplitude of the  $d\alpha/dt$  curve. The  $m$

and n variables represent the skew of the curve, whether it skews to the left or right, as well as the sharpness of its initial incline and how fast it levels out. When m and n differ greatly between runs and isothermal temperatures, the values of k, that are used for the calculation of the activation energy ( $E_a$ ), fail to show an accurate relationship between temperature and the value of k itself. Notably, the values of m and n vary by more than 10% which is significantly greater than that found through DSC analysis.

Table 7: Isothermal Rheology initial fit results

Isothermal Temp (°C)	$k \cdot 10^3$ ( $s^{-1}$ )	m	n
70	$5.6 \pm 0.7$	$0.73 \pm 0.1$	$0.84 \pm 0.08$
80	$7.8 \pm 0.4$	$0.61 \pm 0.02$	$0.72 \pm 0.03$
90	$7.7 \pm 0.5$	$0.49 \pm 0.01$	$0.63 \pm 0.01$
Mean	$7.0 \pm 1.0$	$0.61 \pm 0.1$	$0.73 \pm 0.1$

To combat this, the same approach used when proceeding with the DSC fitting method is applied. Here an initial fit including k, m, and n are found, the values of m and n are then averaged to find values of m and n that allow for the best representation of all the data sets, and in turn the best evaluation for the relationship between temperature and the frequency factor, k. The values used in the  $E_a$  fit with the values of m and n that were held constant are shown in Table 8. When fitting was evaluated while the values were not normalized for all runs, the activation energy became much less coherent and reliable. This can be seen by noting the initial fit values of k, and the normalized m and n fit values of k. See Table SI.7 for a more in-depth explanation.

Table 8: Values used in  $E_a$  calculation

Isothermal Temp (C°)	$k \cdot 10^3$ ( $s^{-1}$ )	m (held constant)	n (held constant)
70	$4.6 \pm 0.3$	0.61	0.73
80	$7.8 \pm 0.4$	0.61	0.73
90	$9.6 \pm 0.1$	0.61	0.73

Shown in Figure 31 is the determination of the rheological isothermal  $E_a$  through slope using the same equation used previously, Equation 6. Knowing the activation energy, the same constant  $m$  and  $n$  values that were used while solving for the activation energy, can be used to determine  $A$ , the frequency factor / pre-exponential constant in the Arrhenius equation, which represents the frequency of reactions in the material. The activation energy calculated from the slope was found to be 38,229 J/mol, which is significantly lower than that found by DSC. One possible factor is thermal lag attributed to the rheometer. Some rheometry interments have multiple heating elements. Typically, one for the upper geometry as well as the lower geometry. The rheometer used in this study does not have a heating element for the upper geometry which means there can be a temperature difference between the plate in contact with the top and bottom of the sample. The x-axis has a  $1/T$  dependence so therefore the data point farthest left in Figure 31 is the highest isothermal temperature, 90°C, which would explain the lower values at higher temperatures. This thermal lag, however, is the less likely of the two possibilities. The other possibility is the method of using values of  $m$  and  $n$  that are held constant may be biased towards lower temperatures causing the values of  $k$  at higher temperatures to misrepresent the characteristics of the material.

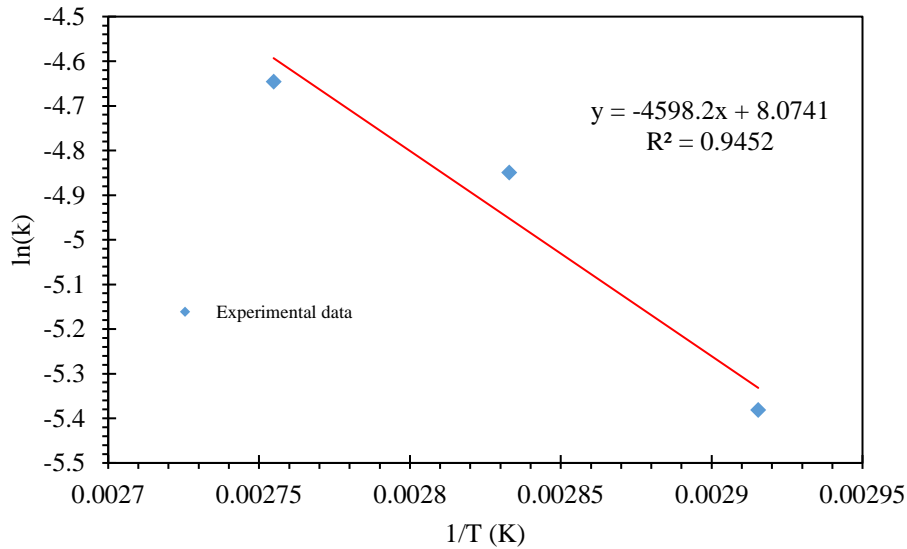


Figure 31: Rheology isothermal activation energy fit calculation

It is notable that when the activation energy calculated using a different method, by ignoring the highest temperature and simply using the triplicate values of k from 70, and 80°C, the found activation energy is much more like the DSC activation energy, which has a virtually zero thermal lag environment.

Table 9 shows the final values found for A, with the respective m and n values that were held constant through all the final rendition of the fit. The regression values shown represent the final fit values using Equation 16 for all data sets averaged. The values of A were also found to be satisfactory. The values of A should theoretically be the same for all isothermal temperatures. It can be observed that the values of A differ no more than 4% which is minimal. These values of A were also found to be agreeable when compared to the value of the y-intercept found in Figure 31, which is also observed in the results from the isothermal DSC studies.

Table 9: Isothermal Rheology final results for fit

Isothermal Temp (°C)	A (s <sup>-1</sup> )	m(held constant)	n(held constant)	Regressions
<b>70</b>	<b>8.022 ± 0.07</b>	<b>0.61</b>	<b>0.73</b>	<b>0.94 ± 0.01</b>
<b>80</b>	<b>8.176 ± 0.04</b>	<b>0.61</b>	<b>0.73</b>	<b>0.93 ± 0.06</b>
<b>90</b>	<b>7.986 ± 0.06</b>	<b>0.61</b>	<b>0.73</b>	<b>0.95 ± 0.04</b>
<b>Means</b>	<b>8.062 ± 0.10</b>	<b>0.61</b>	<b>0.73</b>	<b>0.94 ± 0.04</b>

It's also worth noting that the values of m and n when compared to that of the isothermal DSC results show a different ratio. Where instead of the n being dominant, as seen in Table 8 for the rheological results, the m is dominant in the DSC results.

Equation 16 shows the final fit equation for the isothermal rheological study. All variables solved for are input here: activation energy (E<sub>a</sub>), m, n, and the frequency factor / Arrhenius constant (A). The only variable in the equation is temperature (T), which is input as 70, 80, or 90°C in this study to be directly measured against the experimental data.

$$\frac{d\alpha}{dt} = \exp\left(8.06 + \left(-\frac{38229}{RT}\right)\right) * (\alpha^{0.61}) * (1 - \alpha)^{0.73}$$

Figure 32 shows an example fit using Equation 16 (where  $T = 90^{\circ}\text{C}$ ). This set of experimental data when fit with Equation 16 shows the correct behavior expected along with a high regression of 0.95. Within expectations this is a reasonably good fit. This method of modeling proved valid for isothermal testing through rheology. The fitting equation was successfully calculated and applied to experimental data where good results of congruency were obtained. The regression values shown in Table 9 represent the averaged regression values for the final equation applied to all three temperature sets and averaged. While this method proved successful, this procedure is very sensitive to factors like batch variation, and the time between producing the material, and studying the material. The procedure for this particular material involved mixing many small batches one at a time prior to the experiment. Any duration longer than 45 minutes could lead to the kinetics of the material being mis observed.

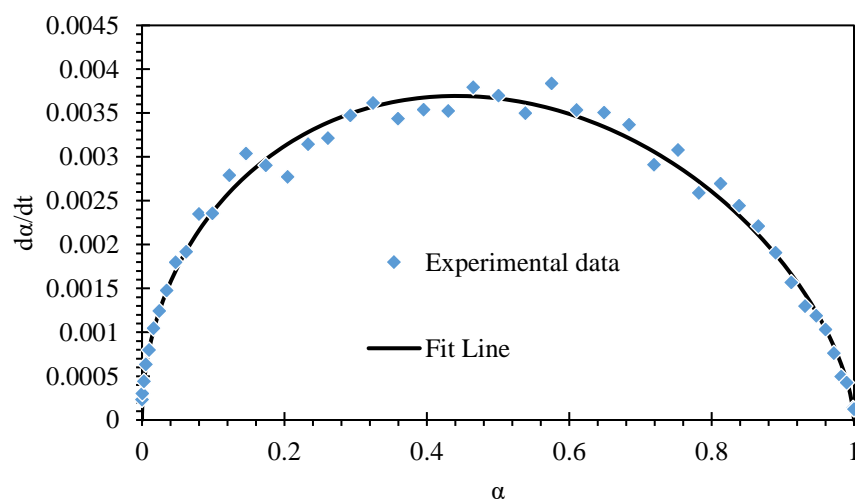


Figure 32: Rheology example fit on experimental data using Equation 16 at 90C

### 4.3 Non-Isothermal Behavior-DSC:

Shown in Figure 33 are the non-isothermal DSC results for ramp rates ranging from 5-30°C/min. As expected, the higher the non-isothermal rate, the higher the temperature that the reaction finishes, and the higher the peak heat flow. Similar to the isothermal DSC experimental results, there is a small reaction taking place before the main peak of reaction, where this time it is much closer to the main peak. In this case the smaller peak is less discernable from the main, but still apparent particularly at higher heating rates. As with isothermal experiments, only the larger more prominent peak was examined in this study as it was chosen to best represent the main reaction. Shown in Table 10 are the characteristics of the experimental non-isothermal DSC data. The data shown in Table 10 showed good consistency similar to the isothermal DSC data taken.

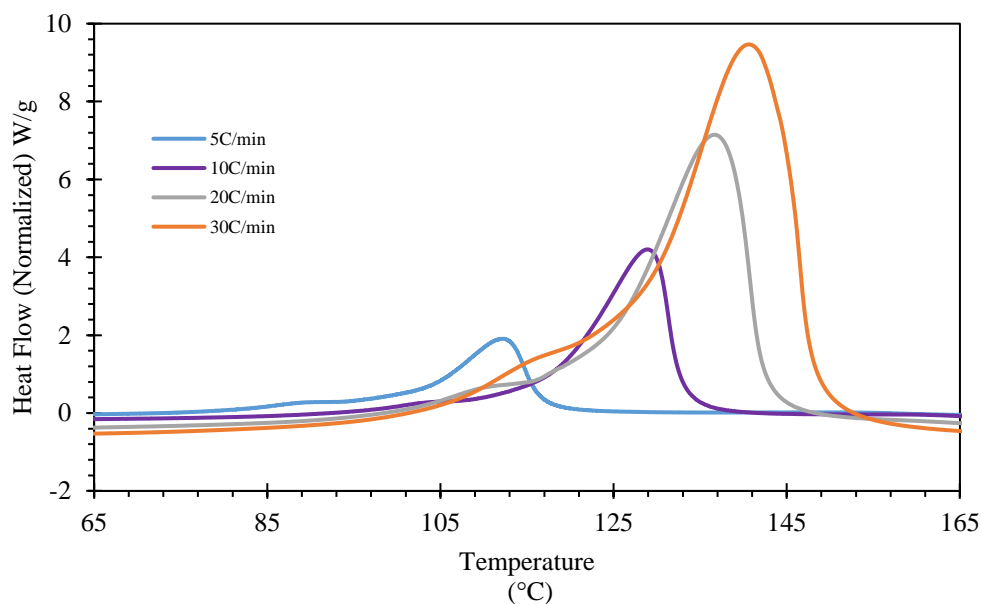


Figure 33: DSC non-isothermal data sets from 5, 10, 20, and 30°C/min

Table 10 shows the reaction times, time at peak, and the peak enthalpy. The reactions start and end times behave as expected: as the rate increases, the time it takes the reaction to start, reach its peak enthalpy, and finish all decrease. An interesting factor regarding the peak enthalpy is the large jump in peak enthalpy when examining the 5°C/min and 10°C/min rates. The enthalpy value at 5°C/min is 180 J/g, and the value for enthalpy at 10°C/min is 250 J/g. An increase in enthalpy is expected at higher non-isothermal rates as at a faster rate the sample can more easily reach a higher total cure conversion. With more thermal energy available at a lower percent cure, the sample may absorb more of the energy to reach a more complete cure. The values above 5°C/min slightly decrease with an increase in non-isothermal rate but remain relatively the same. There is a notably lower value and higher variance for the 5°C/min enthalpies. The method by which the enthalpies were calculated was congruent across all heating rates which leads to the assumption that this phenomenon is either caused by the instrument or the material itself. It is unlikely the instrument is to blame which leaves the material as the contributor to the low value of enthalpy. Since this material is proprietary, not much is known of its chemical composition. As mentioned before there is a slight initial reaction that takes place prior to the main reaction peak. While it is less noticeable in the non-isothermal raw data compared to the isothermal data, it still influences the material. The low value of enthalpy at this rate could also be an indication that something more is happening with the material that is affecting the test results at 5°C/min. It would make sense that the higher temperature rates have a higher total enthalpy as the material will reach a sufficient degree of conversion at a lower temperature with a lower rate. Throughout the process of collecting data, this data set was collected multiple times and shows identical results each time.

*Table 10: Characteristics of non-isothermal DSC results*

Rate °C/min	Induction time (mins)	reaction end (mins)	Peak time (mins)	peak enthalpy (J/g)
5	14 ± 0.8	20 ± 0.5	18 ± 0.7	190 ± 20
10	8.6 ± 0.2	12 ± 0.1	11 ± 0.03	250 ± 3
20	4.8 ± 0.04	6.7 ± 0.07	5.7 ± 0.03	240 ± 0.7
30	3.3 ± 0.02	4.6 ± 0.06	4 ± 0.006	230 ± 6

In Figure 34, the normalized enthalpy plot is shown for an example of 20°C/min. Similar to the DSC data shown for the isothermal case, it was created from the running enthalpy integration. The sampling rate, like the isothermal DSC data, is very high when compared to the rheology results which leads DSC results to generally look smoother. This yields a curve that can be used to find  $\alpha$  at any point during the experiment. This normalized  $\alpha$  curve is calculated using Equation 8, which is a ratio of the heat released at time  $t$ , over the total heat released during the reaction. Enthalpy is used to represent the amount of the reaction that has taken place because it has a direct relationship to the amount of crosslinking completed. This example plot taken at 20°C/min exhibits what is expected: The reaction starts and ends with a slope that's zero. At the beginning of the reaction, the slope diverges from ( $\alpha = 0$ ), while at the end of the reaction, the slope converges to ( $\alpha = 1$ ). With this normalization of all data, it presents a uniform set of kinetic data for use in the study of this reaction.

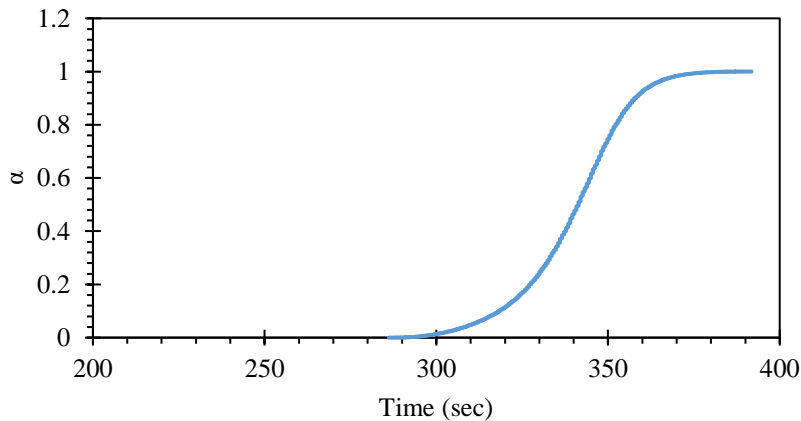


Figure 34: Example of normalized enthalpy from DSC curves at 20°C/min

Figure 35 shows the  $d\alpha/dt$  derivations of example runs at 5, 10, 20, and 30°C/min. As expected, the higher the heating rate, the higher the cure conversion rate. Since all the data was normalized using the method discussed from Figure 34, all data sets fall within ( $0 \leq \alpha \leq 1$ ). This  $d\alpha/dt$  plot is meant to be predicted

by the fitting equation calculated through this method. It is shown that the peak rate of reaction differs depending on the heating rate. For the 5°C/min heating rate, the maximum rate of reaction is achieved at  $\alpha = 0.641$ , whereas at 30°C/min the peak is shifted toward lower conversion ( $\alpha = 0.582$ ). For isothermal experiments, the peaks in the rate of reaction had the opposite trend: Here the value of  $\alpha$  peaks decreased as the isothermal temperature decreased. Under non-isothermal conditions, the peak rate of reaction can be seen happening at lower  $\alpha$  with a higher rate of heating. This is likely due to the material reaching a higher temperature more quickly and as a result, allowing the sample to cure faster at the condition of higher molecular mobility.

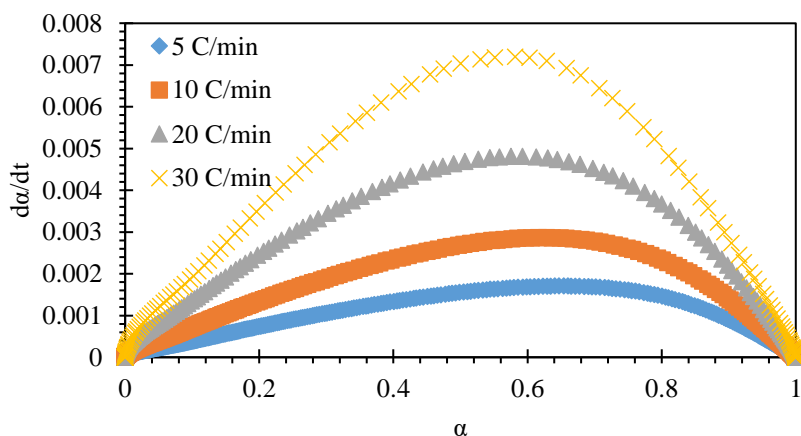


Figure 35: DSC non-isothermal runs calculated from experimental data after normalization

The first step to finding the fit equation, for the non-isothermal method, is to solve for the activation energy. The equation used previously for isothermal methods cannot be used in non-isothermal methods as the equation used for isothermal activation energy ( $E_a$ ) determination has a constant temperature variable within it. For the non-isothermal data, a different method must be used to determine  $E_a$ . For this, Equation 13 is used instead. Equation 13 is found by integrating the Equation 12, with respect to temperature and changing the  $dT/dt$  relationship to  $\beta$  which represents heating rate. Solving the rest of the integration results in this equation, which leaves some grouped constants and a function of  $\alpha$  as the y-intercept. Using a full

data set of 5, 10, 20, and 30°C/min, the activation energy can be solved for by using the Kissinger–Akahira–Sunose (KAS) method and this is depicted in Figure 17 and discussed in section 2.6.3.

The KAS method relies on a dependence between temperature and the logarithm of the rate of heating and the temperature squared as shown in Equation 11. After, we are left with the constant of  $E_a/R$  times the variable  $T$ , temperature, which is the object of the KAS method. This method uses multiple runs obtained at multiple rates to compare activation energies at different points during the cure. The activation energy of a material changes while it cures.

The KAS method allows for the analysis of the activation energy at multiple points during the cure. To do so, the temperature at a specific point during the cure is recorded. For example, for four different runs at rates, 5, 10, 20, and 30°C/min, the temperature at which ( $\alpha = 0.10$ ) is recorded for each rate. Since the rates vary, the temperatures at which ( $\alpha = 0.10$ ) differs. These temperatures are recorded across all runs at whatever value of  $\alpha$  the activation energy is desired to be known.

Figure 36 shows the values of temperature across all rates at the values of  $\alpha$  shown in the legend. There are four rows apparent in Figure 36, each row represents one rate at which these constants were solved for at a given  $\alpha$ . All of the blue squares represent the temperatures at which the different rates had a value of ( $\alpha = 0.10$ ). The points are then coordinated with the different rate values for a given  $\alpha$ . For each set of points for a given  $\alpha$  there is a slope determined. These are then all applied to the relationship discussed previously in Equation 13. An example line is shown correlating all points where  $\alpha = 0.95$ . The slopes of these lines can be used to calculate the activation energy at the value of  $\alpha$  being observed.

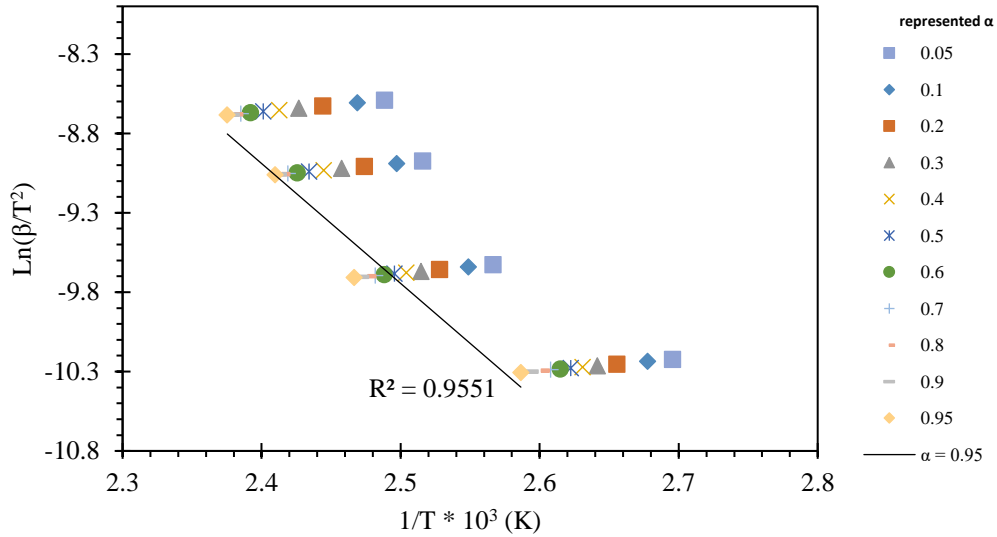


Figure 36: DSC non-isothermal activation energy calculation via the KAS method and relationship from Equation 13

The correlation of the example line is considered to be good with an  $R^2$  value of 0.96 for ( $\alpha = 0.95$ ). The four rows represent the different rates used for this method, the upper most row is  $30^\circ\text{C}/\text{min}$  while the bottom most row is  $5^\circ\text{C}/\text{min}$ . The rates of 10, 20, and  $30^\circ\text{C}/\text{min}$  seem to correlate better than the  $5^\circ\text{C}/\text{min}$  values. This was initially thought to be a product of one of the triplicate data sets used containing an outlier and disrupting the average. To check this, another full set of data was taken at  $5^\circ\text{C}/\text{min}$ . This showed the exact same result as the first triplicate set, the one shown. This may be a result of an unaccounted kinetic property that has temperature dependence, or perhaps the appearance of the start and end of the reaction in results with a lower rate are different than that of higher rates. Which would lead to an incorrect value of  $\alpha$  being calculated and used. This seems less likely as no other portion of this method showed any difference for lower rates.

The DSC non-isothermal activation energy determined as a function of degree of conversion is shown in Figure 37. Figure 37 shows the activation energy based on its point of cure; each point generated from a rate on the KAS figure corresponds to other points from the rates all located at the same cure as

shown by the legend. These slopes, when plotted like this show the activation energy based on what amount of the sample is cured.

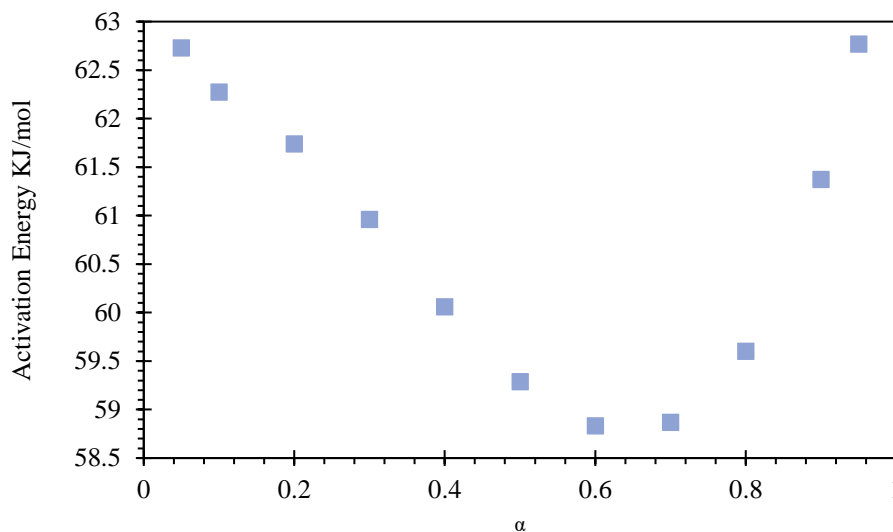


Figure 37: DSC non-isothermal activation energy by cure conversion

In most studies it is observed that the activation energies near the start and end of the reaction tend to vary compared to the middle of the reaction. A common practice is to average the values if there is no steady point to the curve, or if the activation energies level in the middle of the cure to take that value (Zhongliang, Zhang). The averaging method for this study was found to represent the activation energy more accurately. The activation energies found were averaged to 60,773 J/mol with a standard deviation of 1.51 KJ/mol, which compares well to the isothermal DSC results (Ma, Zheng, Qiao). Results from these studies showed epoxies and filled epoxies can show activation energies in the range of 40 KJ/mol to 150 KJ/mol. Many of these studies, along with others cited in this study, used the KAS method to find the activation energy. The values in this study were found the same way and are congruent with what you could expect from a filled epoxy.

With the activation energy solved for the remaining parameters needed to be fit are A, m, and n. The first approach taken was to use the relationship found in Equation 14 to solve a linear fit for the y

intercept ( $\ln(A)$ ), and the slope,  $n$ . This is shown in Figure 38 with a good correlation, axis are labeled with the linear dependence. In turn this can be used in conjunction with the  $p$  variable (defined as the ratio of  $m$  and  $n$ ) to solve for the unknown power  $m$ . The variable  $p$  is obtained by determining the maximum value of  $d\alpha/dt$  for a given experiment and using this value as the base point for a mathematical ratio between  $m$  and  $n$ , as they control the skew of the fit: it's a mathematical ratio between  $m$  and  $n$  that represents both values,  $m$  and  $n$ , in this compounded version of the fitting equation. This linear fit is shown in Figure 38, fit to experimental data.

However, the values of  $m$  and  $n$  for this method are based on the pre mentioned ratio of  $m$  and  $n$ , which was found to be less consistent than other methods (for more information see Table SI.6). The inconsistency within this approach may be due to the activation energy: the activation energy is a prominent term in this linear relationship which may cause an incorrect fit when compared to experimental data. The values of  $\ln(A)$  showed good consistency but for the best result the values of  $m$  and  $n$  found through this method were not used. Instead, the values of  $\ln(A)$  were taken, and the curve fitter was used to calculate the values of  $m$  and  $n$  only.

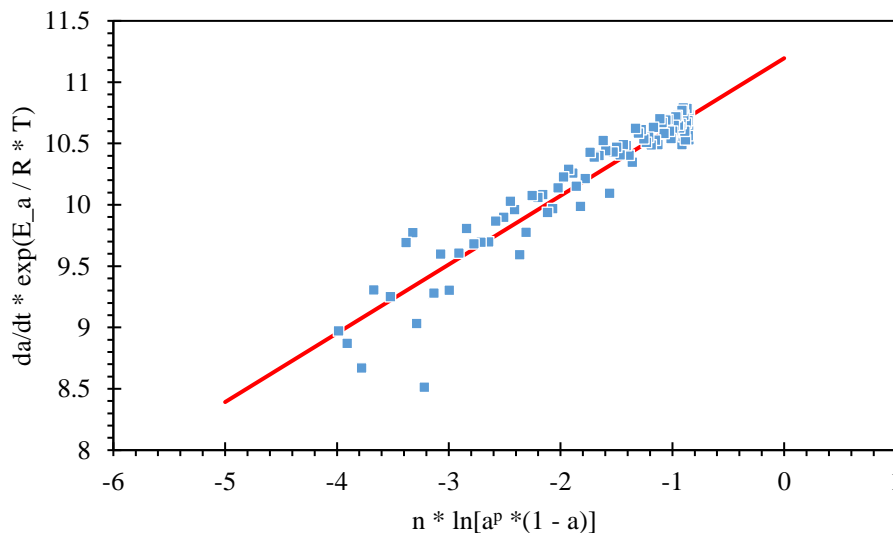


Figure 38: Linear fit example from 5C/min data using Equation 12

For a better resulting fit, the  $\ln(A)$  values collected from the previous approach were averaged and added to the MATLAB curve fitter. The goal of this study is to measure the ability of this model to accurately predict the characteristics of this novel material. In using a fit optimizer, the accuracy of the fit is assured as it relies directly on data taken through experiments to predict the behavior. This method is similar to the isothermal processes of allowing the curve fitter to obtain values for  $m$  and  $n$  independently. These values of  $A$ ,  $m$ , and  $n$  are shown in Table 11. These final values were used in the DSC non-isothermal fitting equation which is shown in Equation 17.

Table 11: Non-isothermal DSC final fit results

Non-Isothermal Rate	$\ln(A)$ ( $s^{-1}$ )	value of $m$	value of $n$	Regressions post fit
5°C/min	$13.56 \pm 0.2$	$0.72 \pm 0.07$	$0.66 \pm 0.05$	$0.96 \pm 0.02$
10°C/min	$13.32 \pm 0.09$	$0.83 \pm 0.04$	$0.8 \pm 0.03$	$0.91 \pm 0.06$
20°C/min	$13.39 \pm 0.05$	$0.64 \pm 0.02$	$0.73 \pm 0.02$	$0.98 \pm 0.004$
30°C/min	$13.31 \pm 0.05$	$0.56 \pm 0.005$	$0.72 \pm 0.007$	$0.94 \pm 0.004$
Means	$13.39 \pm 0.1$	$0.69 \pm 0.1$	$0.73 \pm 0.06$	$0.95 \pm 0.04$

The values of  $A$  from the Matlab fitting procedure showed very consistent results. The value of  $A$  showed no bias toward any trend or temperature rate. The values of  $m$  and  $n$  showed a slight bias towards having higher values at lower non-isothermal rates. Since  $m$  represents the autocatalytic effect,  $m$  is dominant towards the end of the reaction. This can be seen directly from the final fit in Equation 17. Where  $m$  is the exponent to a single term of  $\alpha$  and  $n$  is the exponent of  $(1 - \alpha)$  which means as  $\alpha$  approaches 1,  $m$  becomes dominant. The value of  $m$  generally drops as the rate increases, this may be a result of the total enthalpies of the reaction being measured. Looking at Table 10, the values of enthalpy differ depending on the heating rate. The values of  $n$  seem to conform to the enthalpies found from the raw data in Table 10. When comparing the values of the  $n$  variables found and the enthalpies of those temperatures, they seem to follow an identical trend. The values of  $m$  also seem to conform to this pattern. It's also noticeable that the

dominant variable will differ if the rate is above or below 10 or 20°C/min. This may be an indication of the uncaptured pre-reaction discussed earlier in this section being responsible for more or less initial heat, and heat output through catalysis being measured.

The final fit equation is shown in Equation 17 and fitted to experimental data in Figure 39. Since this is a non-isothermal experiment, we don't have a constant temperature, and therefore can't use a single value of temperature in the fitting process. To work around this, the temperature recorded at each point of experimental data was used as a list alongside the  $\alpha$  variable to get the most accurate fit for a non-isothermal procedure. For each value of  $\alpha$  there is a corresponding value of temperature that was used for T. This creates a three-dimensional plot for the non-isothermal conversion data. To simplify the visuals, a two-dimensional plot was used here instead. The regressions in Table 11 are based off of the three-dimensional plots, an example of the three-dimensional plots has been supplied in Figure SI.3.

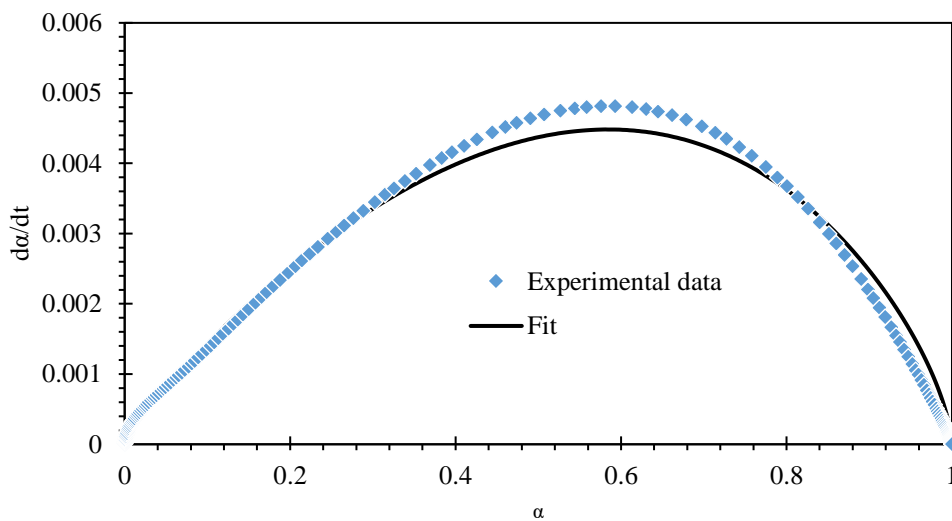


Figure 39: DSC non-isothermal experimental data at 20°C/min with equation fit using Equation 17

The fit has shown good regression values for the overall fit when applied to experimental data. Only viewing the fit in a two-dimensional plot takes away some significance, as the third dimension helps

to demonstrate its accuracy more clearly. Though viewing in two-dimensions still shows its ability to predict well. The overall regression of this fit was (0.976), which shows a very good correlation. The fit doesn't seem to reach the maximum peak of the experimental data, which may relate to the activation energy, which as discussed, showed some deficiency: where the final 5°C/min row seemed to skew slightly from where its expected placement was. These analyses may show that using a lower rate such as 5°C/min with this material may affect calculations to solve for select variables, which in turn can alter the final fit of the sample.

$$\frac{d\alpha}{dt} = \exp\left(13.39 + \left(-\frac{60773}{RT}\right)\right) * (\alpha^{0.69}) * (1 - \alpha)^{0.73} \quad 17$$

#### 4.4 Non-Isothermal Behavior-Rheology:

Shown in Figure 40 is a set of experimental non-isothermal rheology data. Similar to the non-isothermal DSC study, the experiments were performed at four rates: 5, 10, 20, and 30°C/min. The raw data was then treated using a Savitzky-Golay filter for the purpose of minimizing noise in the experimental data prior to analysis (see Figure SI.6 and SI.7 for details). Data for the non-isothermal rheology shown has similar properties as discussed in the isothermal Rheology section of this study. None of the monomer mobility issues described before are observed among the different rates: the phenomenon where the act of crosslinking a material at a certain rate can cause a decrease in the availability of monomers through a decrease in mobility. A clear pattern of induction time and point of gelation can be observed through raw data. All the rheological curves, once cured, converge to the same point, with the higher rates being slightly lower than the others as a result of the reaction finishing at a higher temperature. The slightly negative slope

shown at the end of each of the non-isothermal runs is due to the non-isothermal nature of the procedure, as the material heats up, the material's viscosity decreases.

Similar to the other studies we see the same pre cure reaction occurring before the prominent curing occurs. This is most notable in the 30°C/min curve where around 100°C there is a small jump in complex viscosity. While noticeable in this figure, once normalized (see Figure 41) and without a logarithmic scale, the reaction becomes unnoticeable. As such we have ignored this small initial curing reaction for this work.

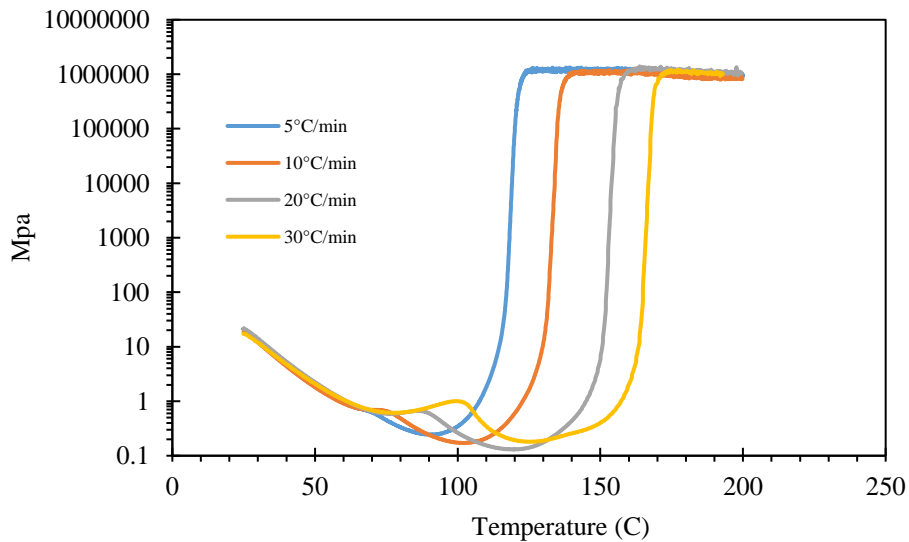


Figure 40: Rheological non-isothermal complex viscosity data sets from 5, 10, 20, and 30 °C/min

Shown in Table 12 are the characteristics of the raw rheological experiments. The trends notable in the table are recurring from the non-isothermal DSC data, where the higher the rate, the faster the reaction starts and completes. Comparing gelation time to the isothermal DHR experiments, the values fall within the expected range of time when compared to the amount of thermal energy entering the sample per unit time.

Table 12: Characteristics of non-isothermal rheology results

Rate °C/min	Induction time (mins)	Reaction end (mins)	Peak time (mins)	Final viscosity (Mpa·s)
5	14 ± 0.1	20 ± 0.1	19 ± 0.2	1.2 ± 0.04
10	8 ± 0.08	12 ± 0.08	11 ± 0.05	1.1 ± 0.02
20	4.9 ± 0.06	7 ± 0.07	6.3 ± 0.02	1.2 ± 0.01
30	3.5 ± 0.07	5.1 ± 0.07	4.7 ± 0.03	1.1 ± 0.04

The values of final viscosity are within experimental error of each other which leads to the assumption that all experimental rates lead to the sample being fully cured to the same degree, which is contrary to what was observed in 4.3 the non-isothermal DSC analysis. All variables shown in the table reflect accurately what was predicted with no significant outliers. It's notable that the induction times, and reaction end times of the non-isothermal DSC results compare very well with only small differences in the values. Another notable similarity is that the recorded peak of the non-isothermal DSC results aligns very well with the gelation times. Since gelation is perceived as the point where the material becomes more dominantly a solid, this can be connected to the rate of cure. Where the rate of cure peaks, it's possible that the ratio of reactants to products shifts as there is more product than reactant, but the peak rate of reaction can occur during other points of curing. However, this aligns well with the gel point as the product amount is dominant making the material more solid than liquid.

Following the same process as for the non-isothermal DSC data, the experimental data is normalized and trimmed, shown in Figure 41. Each data set was normalized individually so as to keep the kinetics the most consistent, with a max value of ( $\alpha = 1$ ) for each set. The data is trimmed using the same principle as the isothermal rheological data, where the storage modulus is used to represent the cure conversion. The negative slope of the material after it is cured is more prominent when the y-axis is not in logarithmic form as shown in the raw data. As discussed before, this is due to the non-isothermal nature of the experiment, where, even after the material is cured, the viscosity and therefore the storage modulus decreases in value with an increasing temperature.

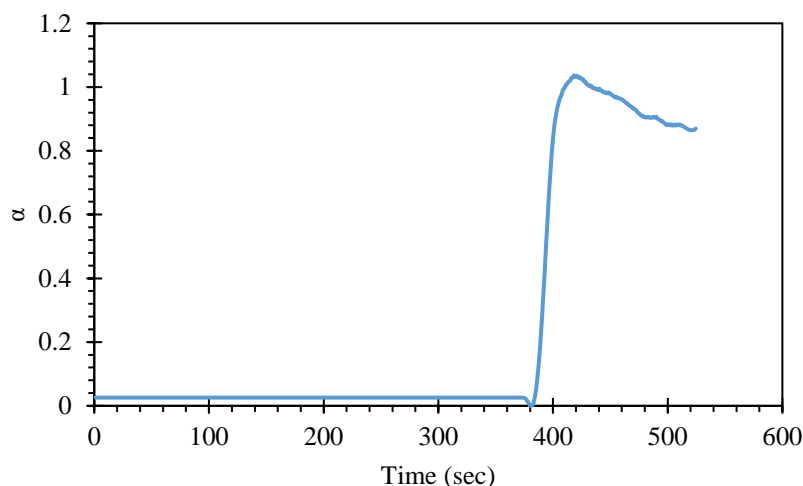


Figure 41: Normalization of 20°C/min storage modulus curve for use in  $d\alpha/dt$  calculation

The resulting derivative for the rate of reaction data, as well as the reaction rate for the other non-isothermal DHR rates can be found in Figure 42. For Figure 42, the rate of the cure is shown with respect to  $\alpha$ . Similar to isothermal rheology data, the continuity of points is poorer than found with DSC. A small wave like pattern can be noticed in the rate. This being due to how the rheometer collects data when compared to DSC. This feature is a result of the instrument having to change the experimental parameters very quickly in order to keep the conditions nominal for the instrument. Extensive testing was done to work around and diminish the effect the instrument had on the final results (for more information see Figure SI.10). A trend of the rate maxima increasing with non-isothermal rate, as well as the location of the peak with respect to cure can be observed.

It can be noticed when comparing the maximum rate achieved of 20 and 30°C/min that the difference between them is less than that of 5, 10, and 20°C/min: the model chosen for this material shows that when constant steps of heating rates are calculated, like 10 to 20°C/min and 20 to 30°C/min, that the peak reaction rate values should increase more per each increment. This may be a product of the instrument being at its maximum heating rate. There may also be other limiting factors within the material itself. The

expected results are that the difference between maximum rates achieved increases with an increasing non-isothermal rate. This would lead to the  $d\alpha/dt$  gap between 20, and 30°C/min being greater than that of 10 to 20°C/min, and 5 to 10°C/min. The experimental runs of 5, 10, and 20°C/min showed an expected results with 30°C/min being the outlier.

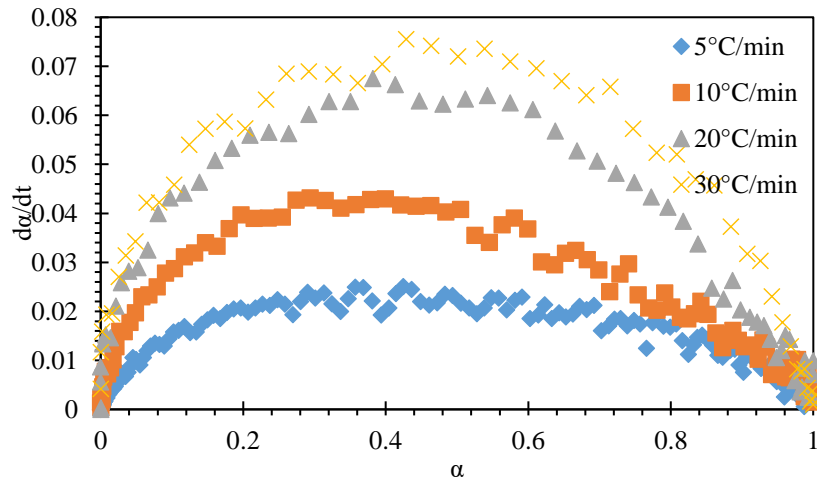


Figure 42: Triplicate  $d\alpha/dt$  curves for all rates calculated from normalization curves

Shown in Figure 43 is the KAS method applied to the non-isothermal rheology data. The rheology results for activation energy showed more consistency than expected when compared to the consistency of results from the isothermal DSC study. In the previous section, 4.3 non-isothermal DSC, the data collected at 5°C/min proved to be an outlier even with repeated tests. With rheological results, the grouping is shown to be tight and consistent along all heating rates. With the calculations of activation energy completed they can be graphed according to their cure conversion as done in the previous section.

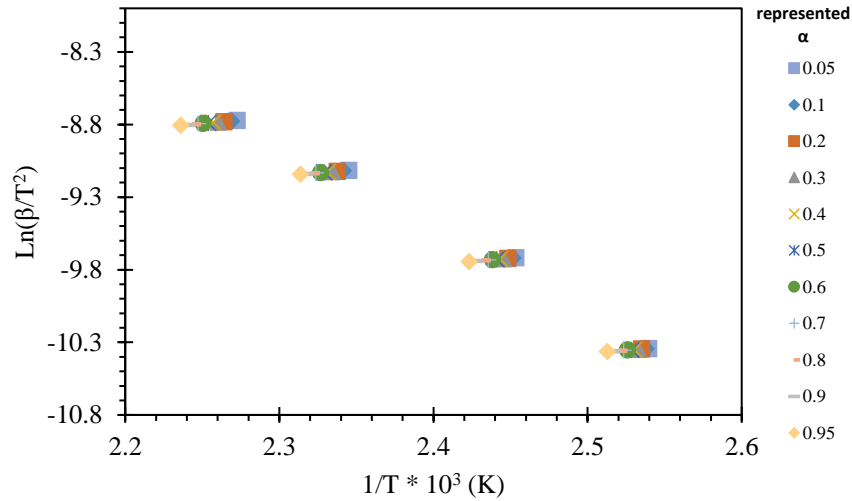


Figure 43: Rheological non-isothermal activation energy calculation involving the relationship found in Equation 13 for the KAS method

It can be seen in Figure 44, that the activation energy as a function of the degree of cure has a different shape than the DSC results. In the previous section the KAS method showed a larger range of activation energies, whereas in this portion of the study, the differences in calculated  $E_a$  were much smaller. Instead of a bell like shape where the ends of the reaction show a different activation energy than at the center, we see that only the initial part of the reaction shows a difference in activation energy. As shown the activation energy decreases by about 4% from start to finish indicating an insensitivity to degree of cure. This variation may be caused by failure to capture the entire reaction through this fitting and trimming method. When making these comparisons, it is important to understand that DSC and rheology methods measure fundamentally different properties, so while results can be comparable, they are collecting different information, and therefore give details of different properties.

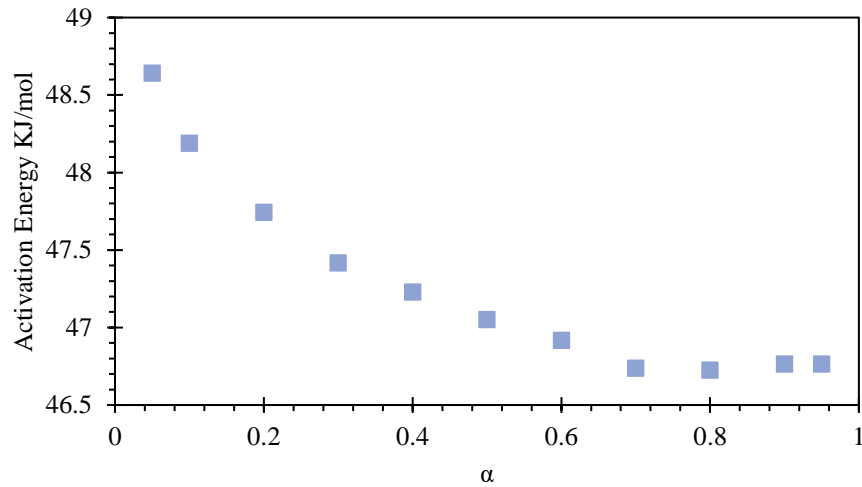


Figure 44: Activation energy by cure conversion for Rheological non-isothermal runs

After the activation energy was calculated, the same method to find A, m, and n was used for the non-isothermal rheology study as was used for the non-isothermal DSC study. This starts by using Equation 14 combined with the relationship mentioned before,  $p = \frac{m}{n} = \frac{\alpha_m}{1-\alpha_m}$  where  $\alpha_m$  represents the maximum value of the rate of cure which can be found from the experimental data (Zhongliang). From this, the value of n is calculated using Equation 14 and the value of m using the mentioned relationship of p. The value of  $\ln(A)$  can also be found using the linear fit. The values of  $\ln(A)$  used for the final fit can also be found using the Matlab fitting described in section 4.3, after which they were compared to the values of  $\ln(A)$  obtained through the linear fit using Equation 14 and these were found to be nearly identical. The values of m and n calculated through this method were shown to have a higher degree of uncertainty similar to what was seen with DSC and therefore the final values of m and n used for the fitting equation were found using the curve fitting software. This procedure was completed with each of the triplicate runs for each heating rate. Table 13 summarized the values of m, n, and  $\ln(A)$  calculated along with the previously found  $E_a$  constant.

The values of  $\ln(A)$ , m, and n are shown with their standard deviations calculated through the procedure discussed above (Table 13). The bottom most row shows the means of these values which will

be the final values for the fitting equation for the non-isothermal rheological characterization of the reaction kinetics for this material. The right most column shows the final regressions of these fits with the final values input into the final fit equation shown later in Equation 18. The values of n show a trend of increasing with an increasing heating rate. A factor of this may be the use of the general form factor of the model of  $\alpha$  used. This model is a common formula applied to epoxies, and it may not capture the kinetics of a filled epoxy such as this magnetically aligned ACA as accurately as a distinct model for this composite material. Dominguez and coworkers show the use of two different models on the same material to test the accuracy of each model and determined that the Kamal model was found to agree better to the low range of  $\alpha$ , but both the Kamal and the Markovic model yielded good results (Dominguez).

Table 13: Non-Isothermal Rheology final fit results

Non-Isothermal Rate	Ln(A) (s <sup>-1</sup> )	value of m	value of n	Regressions
<b>5c/min</b>	<b>11.16 ± 0.03</b>	<b>0.52 ± 0.02</b>	<b>0.76 ± 0.03</b>	<b>0.93 ± 0.02</b>
<b>10c/min</b>	<b>11.32 ± 0.16</b>	<b>0.43 ± 0.02</b>	<b>0.82 ± 0.05</b>	<b>0.87 ± 0.05</b>
<b>20c/min</b>	<b>11.52 ± 0.05</b>	<b>0.54 ± 0.02</b>	<b>0.89 ± 0.01</b>	<b>0.97 ± 0.003</b>
<b>30c/min</b>	<b>11.09 ± 0.06</b>	<b>0.71 ± 0.01</b>	<b>0.97 ± 0.01</b>	<b>0.72 ± 0.2</b>
<b>Means</b>	<b>11.27 ± 0.19</b>	<b>0.55 ± 0.1</b>	<b>0.86 ± 0.09</b>	<b>0.87 ± 0.1</b>

The values of m stay relatively constant, an outlier being the value of m for 30°C/min. This is also the case for the overall regression of the fits when comparing the regression to 30°C/min. As shown before in Figure 42, the experimental  $d\alpha/dt$  curve shown for 30°C/min was lower in amplitude than expected. These experimental plots are used in the calculations for the variables used in the final fit equations, so the effect on the final results may be responsible for the unexpected values found for the 30°C/min case. We suspect that this may result from instrument limitations to maintain this high heating rate during the course of the reaction. As shown in Figure SI.5, the ability to maintain a constant heating rate (temperature measured using a submerged thermocouple) decreases with increasing rate. At a programmed rate of 20°C/min, the instrument is capable of achieving nearly that rate (17.8C/min) whereas at 40°C/min,

performance decreases and this becomes even worse at 60°C/min. As such, we suspect that the error for the 30°C/min data may result from an inability of the instrument to maintain the programmed heating rate. A secondary fit was produced with the exclusion of the 30°C/min dataset as a test to see the impact of the 30°C/min data on the overall fit, this is shown in Table SI.9.

$$\frac{d\alpha}{dt} = \exp\left(11.27 + \left(-\frac{46540}{RT}\right)\right) * (\alpha^{0.55}) * (1 - \alpha)^{0.86} \quad 18$$

Figure 45 shows the final fitting equation, Equation 18, applied to an experimental run at a rate of 20°C/min. The temperature variable in Equation 18 was input as the original values of temperature at a paired value of  $\alpha$  similar to the non-isothermal DSC study. The regression of this particular plot was found to be  $R^2 = 0.968$ , which is a fit that is considered good. The oscillations in the raw data mentioned before can be seen easier in this figure with the addition of the fit line. While the Savitzky-Golay filter minimized the majority of the noise, some does make it to the final  $d\alpha/dt$  data. The average regressions of the fits showed to be 0.87. The averaged regression would be higher with the exclusion of the outlier set 30°C/min. It's important to note that since the values of T were input using previously obtained values of T and  $\alpha$ , the fit is a three-dimensional fit. This was not shown here as the ability to analyze a three-dimensional fit here would be difficult in practice.

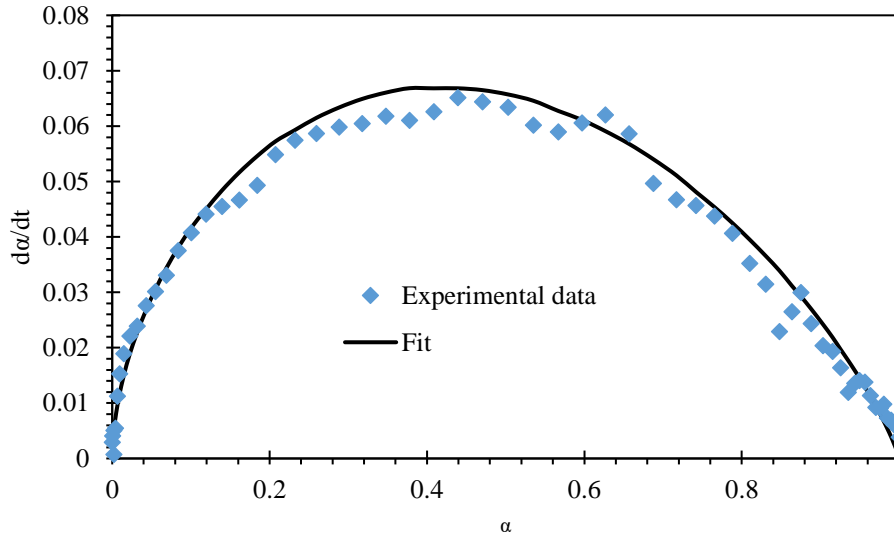


Figure 45: Rheological experimental fit for 20°C/min using Equation 18

The  $m$  and  $n$  values for this fit had similar mean and standard deviation values when compared to non-isothermal DSC values. Values for all non-isothermal fits had larger standard deviations than their isothermal counterpart. For the variables, the majority of constants calculated showed a bias towards temperature rate where in theory they should stay constant, this may be due to shortcomings in the model used. This method is a procedure widely used on many epoxy-based or polymer-based composites: the model used in this study is a basic kinetic model which applies to many different polymers. While it describes the behavior of many polymers well, it may have shortcomings when applied to a novel filled epoxy such as the magnetically aligned ACA used in this study. This study also relied on recycling values of temperature to work around the static temperature input in the final fitting equation. Since these values were used in the calculation and fitting of other constants in the procedure, this may introduce error in the final result. The overall fitting of this material in this non-isothermal rheology study yielded results that are considered good. While comparing it to the other methods in this thesis, the non-isothermal rheology study yielded lower regressions. The information gathered is still of use in a comparison of fitting methods and the assessment of information gathered through each procedure.

#### 4.5 Comparison of Rheology / DSC Results:

DSC and rheology fundamentally measure different things. This is important to acknowledge as the results of a comparison of methods measuring different characteristics of a material or reaction will vary. DSC is a measurement of the heat flow through a sample. The heat flow of the sample is then compared to a reference pan for the ability to determine characteristic temperatures, such as heat of fusion or heat of crystallization. The final result given is the difference of measurement of the reference and the sample pan. This is what produces information on the exothermic chemical reaction of the ACA curing.

Rheology measures the deformation of a material and the flow of matter, most commonly the Storage ( $G'$ ) and Loss ( $G''$ ) modulus. In a controlled environment, you can impose stress or strain on a material to measure the samples viscoelastic properties. When the ACA cures, crosslinking occurs which is linked to rate of reaction and is extrapolated through this method. The results discussed focus on the methods ability to produce a viable fit for experimental data. In the previous section 2.5, the differences between DSC and rheology are further outlined. When comparing DSC and rheology, which are applying two fundamentally different measurements, it's important to take note of each method's ability to measure different aspects of the targeted reaction.

Analyzing Table 14, the overall regressions to the farthest right of the table summarize the final results of the fits. The regressions for DSC fit results exhibit a higher correlation coefficient as compared to rheological fits. With the high sampling rate, and robustness of DSC, data analyzed is a better representation of the reaction occurring with respect to heat released and thus number of bonds formed per unit time when using the autocatalytic model. Rheological results show regressions that are comparable to DSC, and though not as high as DSC, rheology is still able to track the reaction through mechanical means. Something can also be said about the lower standard deviations across the table when comparing DSC to rheological results. The standard deviations of the DSC variables are always either on par, or superior to that of the rheological fits. This is likely due to the sampling rate mentioned prior. The activation energy

calculations for the DSC study were also more consistent. However, the rheological results show a large dip in activation energy when comparing isothermal to non-isothermal which leads to the conclusion that DSC measurements of heat flow offer a more consistent result across both isothermal and non-isothermal methods when using this approach.

Table 14: Consolidated fit data

	Procedure	Ln(A) (s <sup>-1</sup> )	m	n	Ea (J/mol)	Regressions
DSC	Isothermal	15.55 ± 0.10	0.78 ± 0.03	0.71 ± 0.02	61,465	0.98 ± 0.02
Rheological	Isothermal	8.062 ± 0.10	0.61 ± 0.11	0.73 ± 0.10	38,229	0.94 ± 0.04
DSC	Non-Isothermal	13.39 ± 0.1	0.69 ± 0.1	0.73 ± 0.06	60,773	0.95 ± 0.04
Rheological	Non-Isothermal	11.27 ± 0.19	0.55 ± 0.1	0.86 ± 0.09	46,539	0.87 ± 0.1

Comparing the results of all isothermal studies, both DSC and rheology, shows that both methods were successful in modeling the behavior of the material during cure. Both ln(A) values show very low standard deviations. However, the value of ln(A) for the rheological method was significantly lower. Since the ln(A) value represents the frequency factor which is the part of the ratio in the Arrhenius equation that shows the number of reactions taking place per second, this may be due to the differences shown in the activation energy. The greater the value of activation energy, the lower the reaction rate is. This may be the model compensating for the lower values of activation energy by showing a lower frequency factor: if it takes less energy for a reaction to occur, the higher the probability that it will occur and therefore less collisions are needed. This may also play a part in the lower value of m which is scaled with the amount of reaction completed which best represents the autocatalysis of the reaction. The values of n showed greater consistency which leads to the conclusion that the part of the reaction that is not autocatalysis is measured more equally. For details about individual regressions per temperature or rate, see Table 15.

Table 15: Regressions of all fits

Temperature/Rate	DSC	Rheology
70C	0.96 ± 0.04	0.94 ± 0.01
80C	0.98 ± 0.008	0.93 ± 0.06
90C	0.99 ± 0.006	0.95 ± 0.04
5C/min	0.96 ± 0.02	0.93 ± 0.02
10C/min	0.91 ± 0.06	0.87 ± 0.05
20C/min	0.98 ± 0.004	0.97 ± 0.003
30C/min	0.94 ± 0.004	0.72 ± 0.2

Shown in Figure 46 are all the experimental fit equations on a singular plot for the Isothermal procedures. DSC fits shown in the red gradient, rheological results shown in the blue gradient. All isothermal procedures were done at 70, 80, and 90°C, which is how they're shown ascending from the bottom, respectively. Since DSC and rheology methods rely on different characteristics to determine the amount cured, it's expected that the overall amplitudes of these equations are dissimilar. These fit lines represent what was talked about in the previous paragraphs. The average times for the length of reaction for DSC was shorter than that of rheology which is shown here as well. The area under the curves can be thought of as the amount of reaction completed. If the same reaction at the same temperature is completed within a short time period, then the rates needed to achieve that are higher than that of the slower one. This reinforces the fact that the properties measured by these instruments differ fundamentally. The skews of each curve fit, and the values of activation energy and frequency factor can also be seen here. Where the activation energy and frequency control the amplitude, and the values of m and n show the skew of the curve being either biased to earlier in the reaction, like for the case of m where m is the power of  $(\alpha-1)$ , and n which is the power of  $(\alpha)$ .

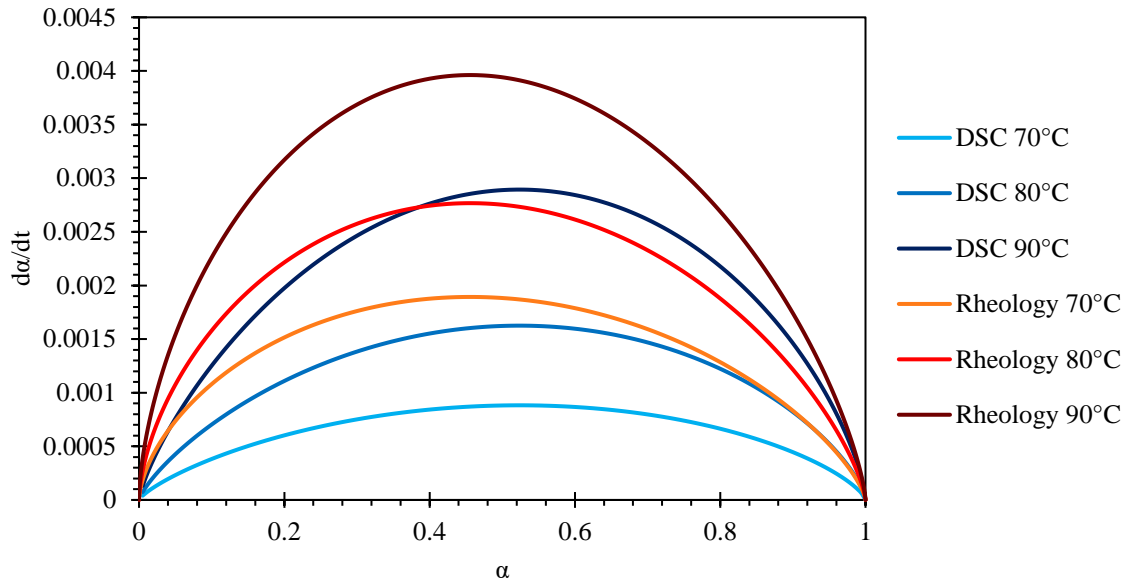


Figure 46: Both DSC and Rheological isothermal fits compared

Non-isothermal results showed good regressions. However, similar to the isothermal results, DSC conforms to the experimental data better with greater consistency. The lower regression demonstrated by the rheological fit may be a result of the issue mentioned before in section 4.4 where the actual temperature rate of the sample differs more the greater the heating rate selected. Regression of the overall fit of the non-isothermal rheological study may have increased if excluding the 30°C/min data set like mentioned prior, but the 30°C/min data set was still included as to best evaluate the whole fitting method and reflect the whole ability of the procedure. For details about individual regressions per temperature or rate, see Table 15. A similar result as the isothermal can also be seen in the  $\ln(A)$  values where the value found through the rheological fit is lower than that of isothermal results. This aligns well with the reason mentioned for the lower value in the isothermal rheological fit. Where the lower value of activation energy causes the value of  $\ln(A)$  to be underinflated. In the non-isothermal case, the difference between the values is less than the isothermal case and this is reflected in the activation energy calculated. The values of  $m$  and  $n$  are also reflected in the same way that the isothermal results were.

In Figure 47, we see the representations of both the DSC and rheological fits in the red and blue gradients for 5, 10, 20, and 30°C/min respectively ascending from the bottom of the figure respectively. With a larger difference in amplitude for reasons discussed prior, two different scales were used to represent the fits. The most noticeable difference between the DSC and rheological fit results is the skew of the graph, represented by  $m$  and  $n$ . The skew of  $da/dt$  to lower conversion was observed for rheological characterization for both non-isothermal and isothermal, further work would be required to fully understand this phenomenon. This furthers the representation on  $m$  and  $n$ , and activation energy and  $\ln(A)$  in the fits. The values of  $m$  and  $n$  for non-isothermal studies had larger differences than that of isothermal studies, as is seen in Table 14, which describes the larger skews shown. The same can be said for activation energy. The scales of the plot differ greatly, while the activation energy and  $\ln(A)$  values could be used to describe the differences in the isothermal plots, here the difference in those values are not as severe as in isothermal fits. This demonstrates that measuring non-isothermally with DSC and rheology shows an even greater difference than in an isothermal study. This may be related to how the initial reaction that can be seen in the raw data graphs in section 4.1 through 4.4 affects the heat flow of the primary reaction being studied which may give insight into what is happening during this secondary.

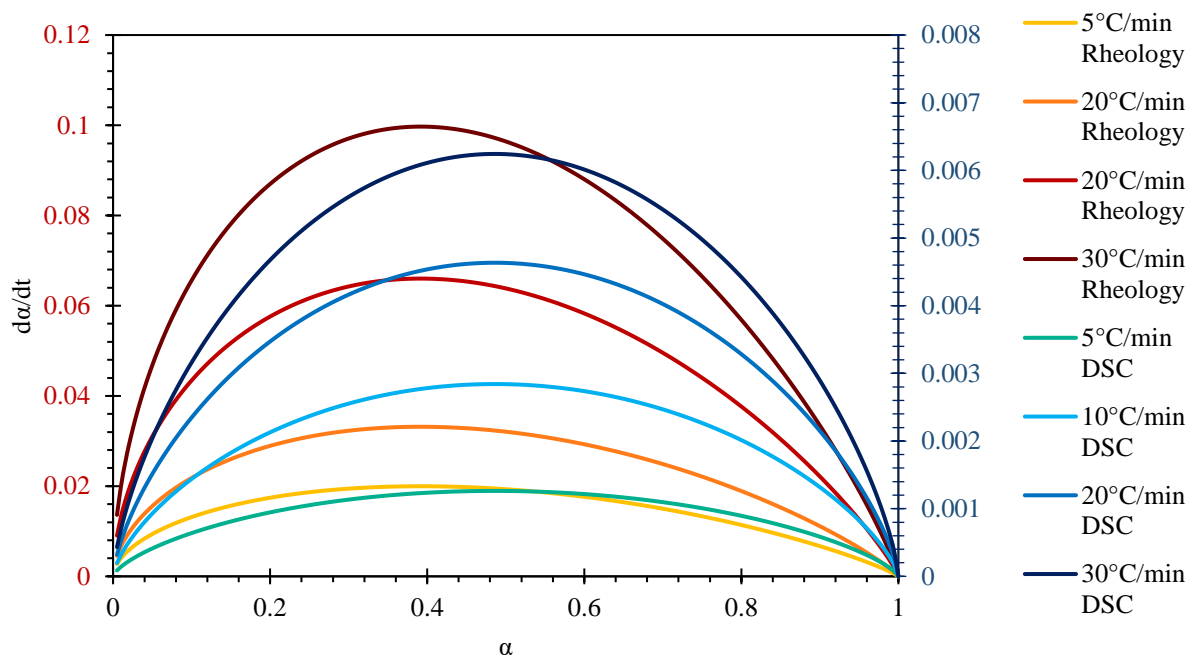


Figure 47: Both DSC and Rheological non-isothermal fits compared

While all analyses are considered acceptable ways to measure and predict a fit, they each have their own strengths. The ability of these methods to correctly predict experimental data is clear. This may represent the capacity of each instrument's input to correlate to this autocatalytic model for this ACA. The autocatalytic model also proved to be the correct choice as its ability to create an effective curve fit with multiple instruments and thermal inputs showed to be consistent with experimental data.

## Chapter 5: Conclusions and Future Work

### 5.1 Conclusion:

This work investigated the characteristics of a novel magnetically aligned anisotropic conductive adhesive in the form of an epoxy. This magnetically aligned ACA has shown much promise within the electronics manufacturing industry. This material offers a simpler way of applying an ACA with the same benefits of better physical resistances and the ability to use this material in higher component density settings. When an ACA is used on an interconnect between components, it's important to understand the kinetics of the material throughout its cure. To do so, the Šesták Berggren autocatalytic model was applied to data taken using DSC and rheology through both isothermal and non-isothermal procedures. These results allow for better insight into the curing process under different processing environments. This fit could be used in tandem with thermocouple data from the applicable industrial process to best predict the cure conversion at a point during production.

Isothermal data yielded fits that showed greater regressions to the experimental data. The process of isothermally fitting experimental data is a much simpler process when compared to non-isothermally fitting. The final values for the isothermal DSC and rheology A, m, and n results showed the values of n being greater than m for both DSC and rheology results. The behavior of m and n in all isothermal cases changed with each different set of temperature runs. For isothermal runs n proved to be the most consistent across all runs and instruments. As the temperature of the experiment was increased, the values of m would decrease, while the values of n would increase at a slower rate. In general, the isothermal data proved to be a good representation of curing kinetics.

Non-isothermal data showed lower regressions than the isothermal data but are still considered good. The consistency of the values of m and n over instruments was better, which leads to the conclusion that the non-isothermal results allow a more accurate comparison of curing kinetic. This is in part to the

consistency of heat transfer being more dynamic with non-isothermal temperature rates. However, it is important to distinguish what each instrument type is measuring, and that they are fundamentally different. This gives more meaning to each variable as it shows each instrument's relationship to the materials behavior within this method.

The practical applications of an autocatalytic fit such as this pertain to its ability to understand material behavior in a heated environment. Knowing things like gelation point, time to cure, and the speed of the cure allow the manufacturer to adjust the method used when applying this material to electronics. This study observed similar trends using the two techniques, though different values of the peak rate achieved differ reflecting the differences in the analytic models. Understanding the kinetics of a material has practical value in manufacturing and assembling electronics. The ability to predict material behavior under a specific temperature condition allows for the optimization of material properties and assembly efficiency.

## 5.2 Future Work:

While this study focused on the acquisition of information used to optimize the process of curing a magnetically aligned ACA, there is much room for development on applying this materials kinetics to optimizing an industrial process for production of electronics using the Ztach ACA. Since Ztach is used as an interconnect material, there must be a very consistent method to apply and cure the paste. If the thickness of the layer varies, the resistance also varies which can cause large inconsistencies resulting in poor performance or damage to the circuit. Expanding on this, using the kinetic data, an appropriate heating process to ensure the viscosity of the material during the manufacturing process along with its total cure conversion and physical properties can be optimized to ensure the best product. More work is required to establish the relationship between study results and application to the manufacturing process. As well as the impact the point of gelation on particle mobility.

The ability to accurately measure the viscosity of the material while it's under a magnetic field for column aligned top best emulate the industrial method could also be created. This would involve using a modified rheometer or viscometer to accurately measure the properties of the material in an environment most similar to what the real industrial settings would be.

## Appendix:

### Supplementary Tables:

*SI Table 1: Isothermal DSC extended properties table*

Temperature °C	reaction start (mins)	reaction end (mins)	first peak time (mins)	second peak time (mins)	first peak enthalpy (J/g)	second peak enthalpy (J/g)
70	18.8	57.51	8.42	37.8	5.9	54.6
70	26.21	68.37	7.48	45.49	5.79	61.66
70	21.81	56.54	8.83	39.02	8.41	58.5
80	12.6	36.65	5.98	26.13	5.69	101.11
80	11.72	36.1	5.5	25.24	4.8	102.11
80	12.92	36.17	6.01	25.72	5.03	111.47
90	6.45	20.07	3.94	13.63	2.6	119.49
90	6.25	18.29	3.37	13.12	1.9	117.76
90	6.43	19.96	3.66	13.73	2.64	110.19

*SI Table 2: Isothermal Rheology extended properties table*

Temperature °C	reaction induction time (mins)	reaction end (mins)	gelation time (mins)
70	7.79	74.63	63.62
70	8.8	77	66.83
70	9.73	80.88	71.01
80	6.08	39.67	32.96
80	7.21	41.28	34.18
80	7.13	42.27	35.38
90	4.26	23.57	18.93
90	4.28	25.74	20.63
90	4.6	25.12	20.49

SI Table 3: Non-isothermal DSC extended properties table

Rate °C/min	Induction time (mins)	reaction end (mins)	Peak time (mins)	peak enthalpy (J/g)
5	14.89	20.29	18.29	212.63
5	14.05	20.13	18.01	202.28
5	13.2	19.41	16.99	169.37
10	8.7	11.89	10.63	246.47
10	8.67	11.96	10.58	243.98
10	8.31	12.15	10.62	249.97
20	4.84	6.7	5.72	234.75
20	4.77	6.7	5.74	236.06
20	4.83	6.58	5.68	235.62
30	3.36	4.68	4	232.01
30	3.35	4.57	4.01	223.51
30	3.32	4.67	4.01	221.11

SI Table 4: Non-isothermal Rheology extended properties table

Rate °C/min	Induction time (mins)	reaction end (mins)	Peak time (mins)
5	13.68	20.44	18.59
5	13.89	20.62	18.92
5	13.93	20.37	18.68
10	8.04	11.68	10.72
10	7.89	11.84	10.7
10	7.92	11.74	10.63
20	4.86	7.02	6.35
20	4.95	7.06	6.33
20	4.83	6.93	6.36
30	3.55	5.21	4.72
30	3.42	5.11	4.7
30	3.44	5.08	4.67

SI Table 5: All final fit regressions for both isothermal and non-isothermal DSC and rheology

Run #	Temperature/Rate	DSC	DHR
1	70C	0.98423	0.95699
2	70C	0.91576	0.93519
3	70C	0.98423	0.9304
1	80C	0.99116	0.85642
2	80C	0.9744	0.95345
3	80C	0.98141	0.97484
1	90C	0.99377	0.96937
2	90C	0.98134	0.97589
3	90C	0.9865	0.90203
1	5C/min	0.96363	0.9195
2	5C/min	0.94009	0.91135
3	5C/min	0.9707	0.94659
1	10C/min	0.83687	0.90951
2	10C/min	0.94217	0.87721
3	10C/min	0.93718	0.8087
1	20C/min	0.97903	0.97445
2	20C/min	0.98614	0.97744
3	20C/min	0.97908	0.97241
1	30C/min	0.94022	0.53793
2	30C/min	0.94673	0.66816
3	30C/min	0.94661	0.95517

SI Table 6: Non-isothermal DSC results of *m* and *n* when using the only the linear fit which showed values that corresponded poorly to experimental data

Rate (°C/min)	value of <i>n</i>	value of <i>m</i>
5	0.88	0.5544
5	0.82	0.5166
5	0.88	0.5544
10	0.84	0.5124
10	0.84	0.5124
10	0.84	0.5124
20	0.78	0.4602
20	0.8	0.472
20	0.79	0.4661
30	0.76	0.4294
30	0.8	0.452
30	0.79	0.44635

SI Table 7: The values of *k* with respect to the initial and secondary fits demonstrating the improvement

Temperature (°C)	initial value of $k \cdot 10^3$ (s <sup>-1</sup> )	second fit value of $k \cdot 10^3$ (s <sup>-1</sup> )
70	5.6 ± 0.7	4.6 ± 0.3
80	7.8 ± 0.4	7.8 ± 0.4
90	7.7 ± 0.5	9.6 ± 0.1

Shown in SI Table 7, the initial values of *k* shown represent the values obtained from applying the most basic of fits to experimental data, which is just the fundamental rate equation. The aim of this portion of work was to find a set of *k* values in which the activation energy could be solved for. The main issue with that being is that when the fit is applied to three different types of data sets, the number of variables being solved for start a power struggle for control over the fit that ends with an accurate fit, but with a wide variation between each of the data sets. This is shown in Table 7 where the *k* values act much more sporadic than expected. To solve this, the values of *m* and *n* from this initial fit were averaged and used in the second fit to demonstrate the actual relationship between the isothermal data sets. This is what's shown in Table 8 where the values correlate much more to what is expected. These are the values used in the activation energy calculation for the most accurate approximation.

SI Table 8: All final fit results condensed into a single table

Procedure	Rheological				DSC			
	Ln(A)	m	n	Regressions	Ln(A)	m	n	Regressions
70C	8.022 ± 0.07	0.73 ± 0.11	0.84 ± 0.08	0.94 ± 0.01	15.59 ± 0.047	0.76 ± 0.04	0.72 ± 0.01	0.96 ± 0.04
80C	8.176 ± 0.04	0.61 ± 0.02	0.72 ± 0.03	0.93 ± 0.06	15.48 ± 0.023	0.78 ± 0.01	0.69 ± 0.01	0.98 ± 0.008
90C	7.986 ± 0.06	0.49 ± 0.01	0.63 ± 0.01	0.95 ± 0.04	15.57 ± 0.17	0.80 ± 0.02	0.71 ± 0.02	0.99 ± 0.006
5C/min	11.16 ± 0.03	0.52 ± 0.02	0.76 ± 0.03	0.93 ± 0.02	13.56 ± 0.2	0.72 ± 0.07	0.66 ± 0.05	0.96 ± 0.02
10C/min	11.32 ± 0.16	0.43 ± 0.02	0.82 ± 0.05	0.87 ± 0.05	13.32 ± 0.09	0.83 ± 0.04	0.8 ± 0.03	0.91 ± 0.06
20C/min	11.52 ± 0.05	0.54 ± 0.02	0.89 ± 0.01	0.97 ± 0.003	13.39 ± 0.05	0.64 ± 0.02	0.73 ± 0.02	0.98 ± 0.004
30C/min	11.09 ± 0.06	0.71 ± 0.01	0.97 ± 0.01	0.72 ± 0.2	13.31 ± 0.05	0.56 ± 0.01	0.72 ± 0.01	0.94 ± 0.004

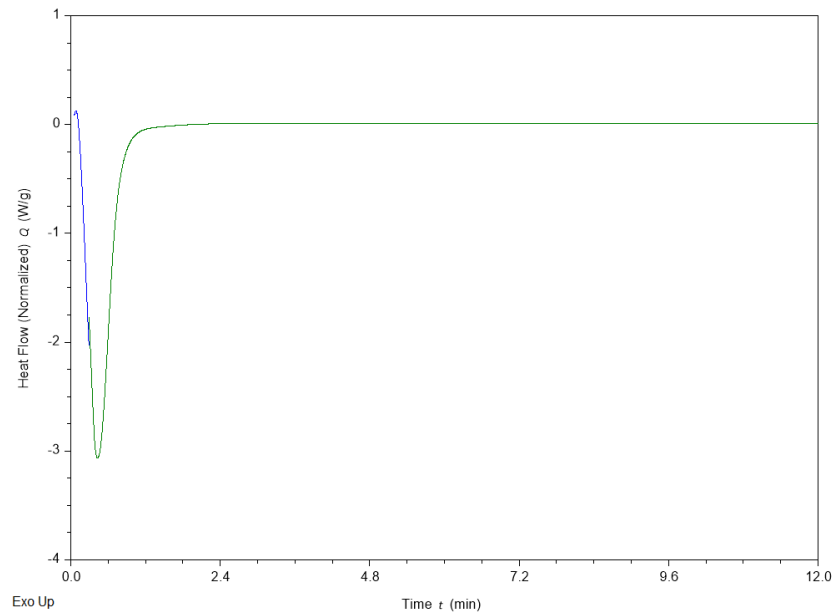
SI Table 9: Non-isothermal rheology fit parameters excluding the 30°C/min dataset

Rate (°C/min)	A (s <sup>-1</sup> )	m	n	R <sup>2</sup>
5	12.11	0.35	0.49	0.88
5	12.05	0.33	0.51	0.89
5	12.06	0.36	0.53	0.93
10	12.09	0.29	0.63	0.89
10	12.13	0.29	0.59	0.87
10	12.39	0.26	0.55	0.8
20	12.42	0.41	0.72	0.84
20	12.34	0.39	0.7	0.9
20	12.32	0.38	0.7	0.89
Means	12.21	0.34	0.6	0.88

SI Table 9 shows an identical fit of the rheological non-isothermal data with the exemption of the 30°C/min dataset. The results show an improved overall regression but not significantly. This indicates that the 30°C/min dataset altered the fit in a way that improved the regression of the fit for other rates. With the altering of parameters, this may show that higher rates such as 30°C/min show a greater sensitivity with respect to the equations ability to predict kinetic behavior.

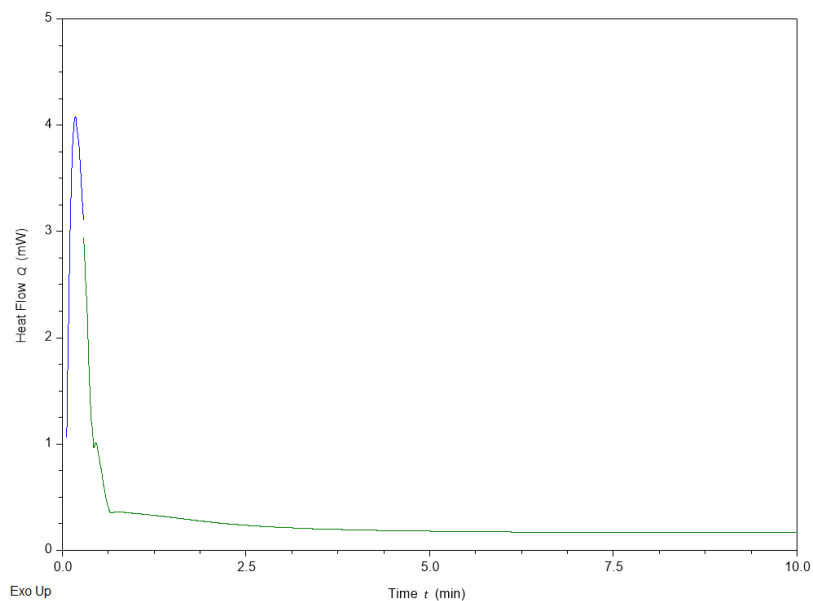
## Supplementary Figures:

In SI Figure 1, the DSC results for the material are shown with no hardener added. Since the hardener was not added there is no reaction taking place. If the small initial peak shown in experimental data was a system response, the binder/filler itself, or the instrument, it would be shown here. Since no response can be seen here it can be surmised that the initial reaction is a part of the material curing itself. Since the initial reaction is small, it was thought best to ignore it in favor of focusing on the main reaction peak where the kinetics of the material could best be observed.



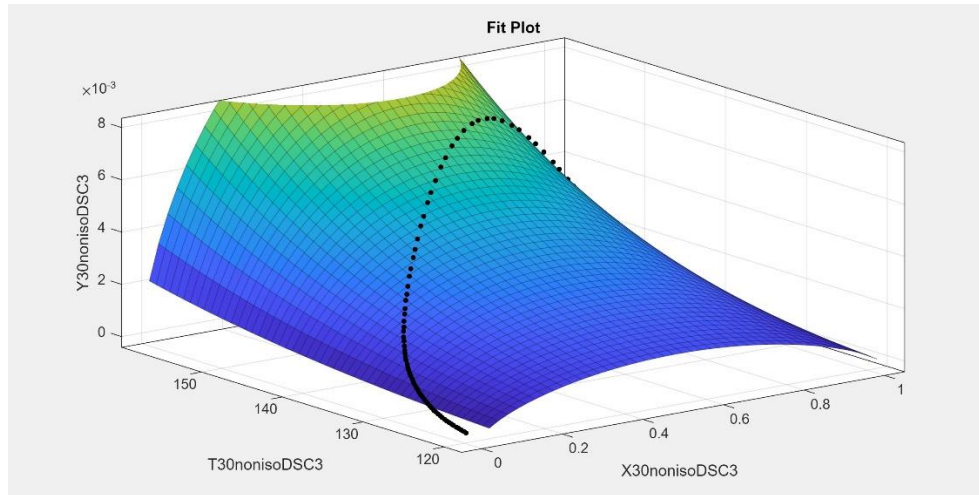
SI Figure 1: DSC non-isothermal experiment with no hardener added to ACA

SI Figure 2 below shows the sample experiment ran without anything in the sample pan to confirm the issue was not with the instrument itself. The test showed that the empty pan showed no influence on the section in question.



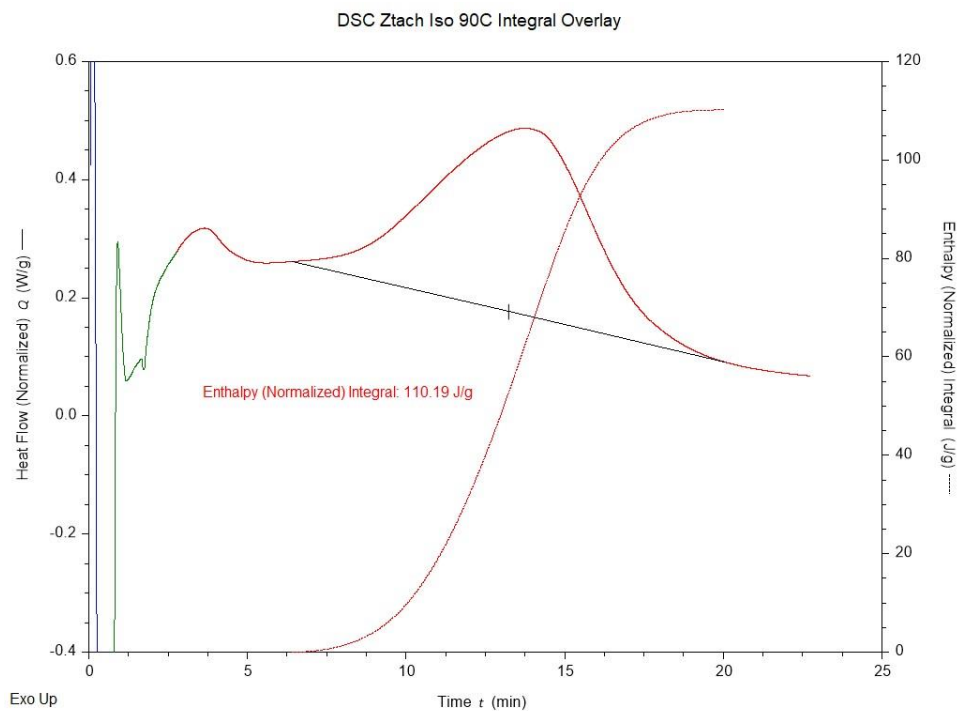
SI Figure 2: DSC experiment with empty DSC pan to confirm no issues regarding instrument

SI Figure 3 is an example of a three-dimensional plot used for curve fitting is shown. The x-axis represents the cure conversion  $\alpha$ , the y-axis represents  $d\alpha/dt$ , and the third axis “T” represents the values of temperature collected through the experimental data plotted. The green/blue three-dimensional topology represents the fit predicted for a given value of temperature at that point. This was the way the values of m and n were calculated for each experimental data set for the final values.



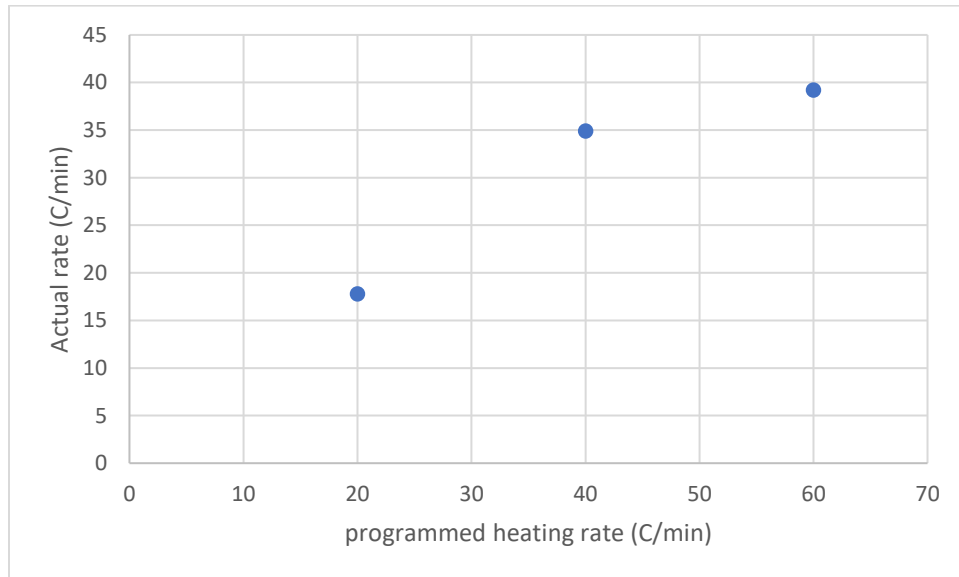
SI Figure 3: Example of a three-dimensional plot used in the context of the curve fitter from MATLAB

SI Figure 4 is an example of the integration process used to find the enthalpy for each experiment. The enthalpy curve can be seen starting at 0 J/g at about 6 minutes where it completes its cure around 18 minutes. This is a running integral which allows for enthalpy to be normalized to the heat flow at the beginning and end of the curing reaction.

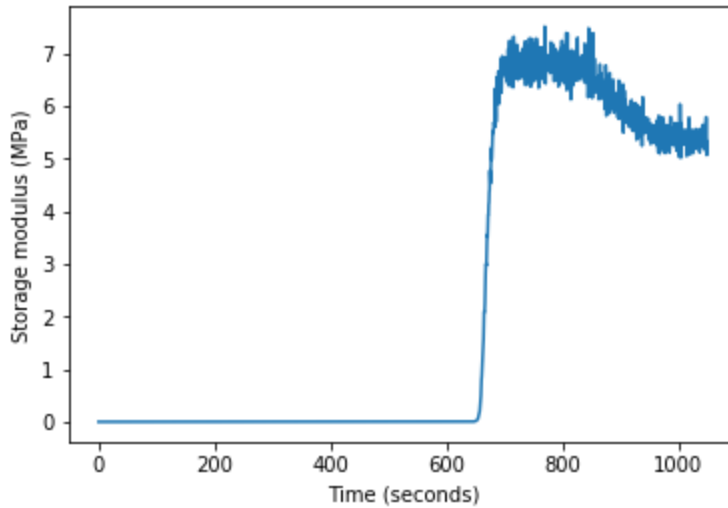


SI Figure 4: Example of the integration method used when finding the enthalpy curve with respect to the heat flow data collected from DSC

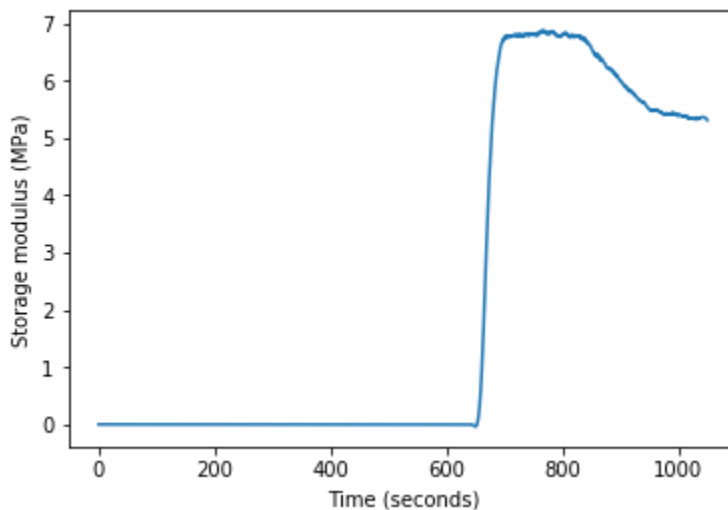
SI Figure 5 shows the expected heating rate versus the actual heating rate of the rheometer used in this study. The trend can be seen that the higher the programmed heating rate, the lower the actual heating rate will deviate from the expected. This leads to error in calculations regarding the ability of the rheometer to actually input the correct amount of thermal energy into the sample.



*SI Figure 5: Data collected by Dr. Christopher Lewis regarding the accuracy of the expected heating rate of the rheometer and the heating rate that is observed at the sample position*

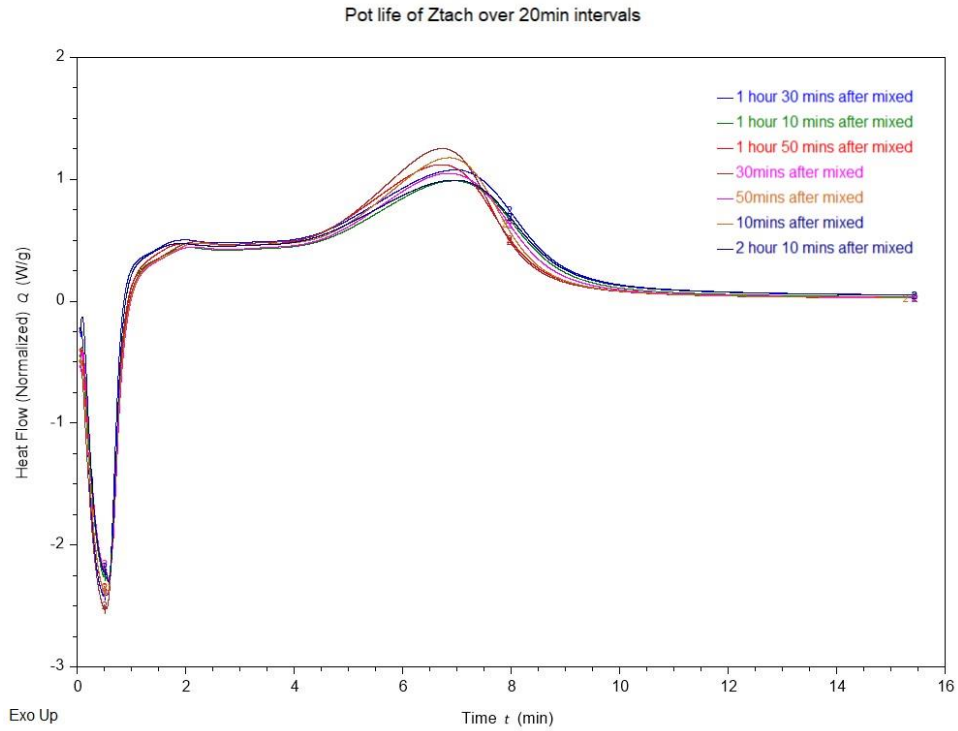


SI Figure 6: Experimental rheology data taken at 10°C/min without the use of the Savitzky Golay filter

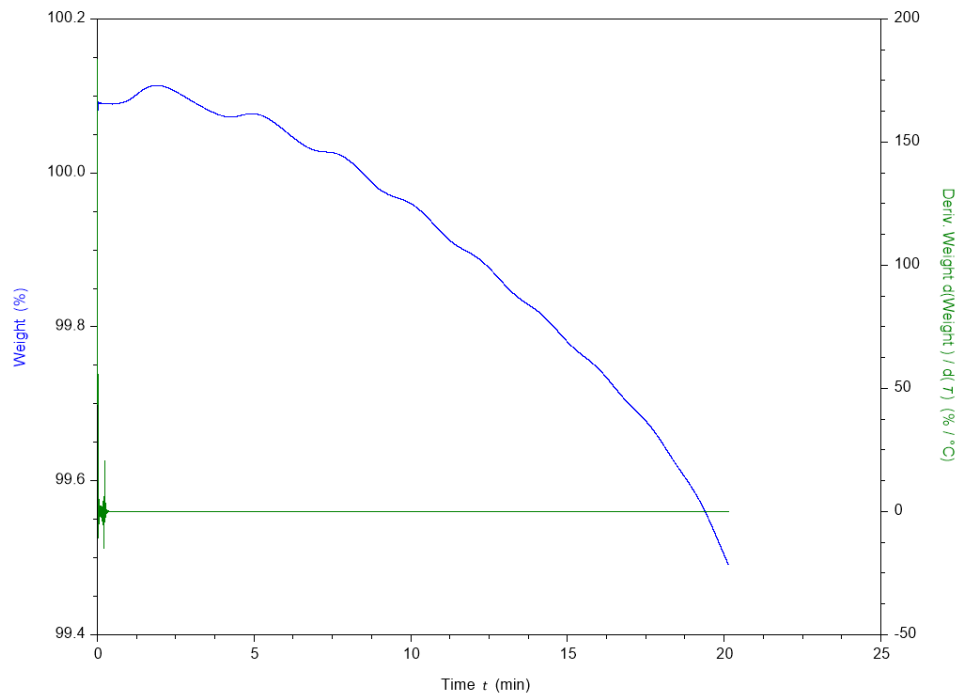


SI Figure 7: Experimental rheology data taken at 10°C/min with the use of the Savitzky Golay filter

SI Figures 6 and 7 show the impact of the Savitzky Golay filter on experimental rheological data. The Savitzky Golay filter is a least-squares smoothing method for signals (Schafer). This is meant to reduce noise and create a set of data points to show the true signal most accurately. This was originally a filter meant to reduce noise in chemical spectrum analysis but can also be used for data such as rheology (Schafer, Hellebois)



SI Figure 8: The ACA was used in a continuous manner running one experiment ever 20 mins to determine the pot life

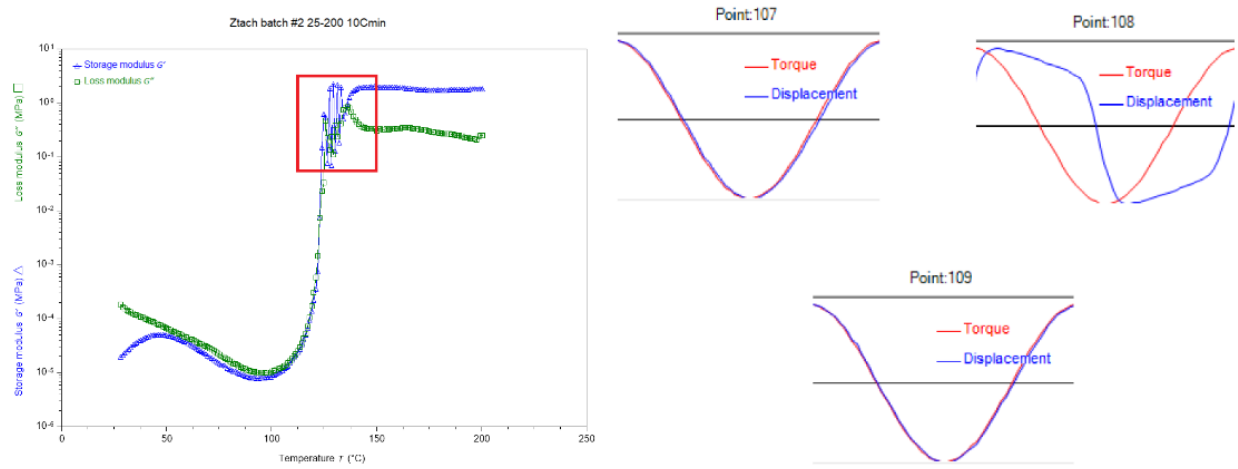


SI Figure 9: TGA of Ztch set at 200°C showed no significant weight loss

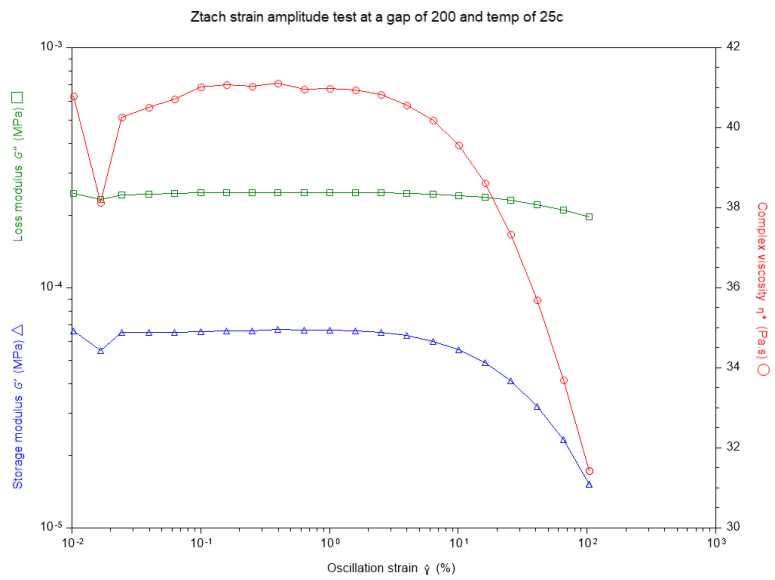
An example of early procedural challenges is shown in below in SI Figure 10. Creating the procedure for acquiring accurate data took extensive testing. When materials testing began, a commercially available test epoxy was used to test the disposable plate accuracy and consistency. The epoxy allowed the testing of a strain and torque altering option called “Non-Iterative Sampling”. This option changed the strain and torque values based on material reaction, allowing for a more consistent result from a dynamic material such as an epoxy. Once a reliable method was developed, Ztach material testing began. Initially the data collected showed a cyclic relationship that would form between strain and torque. When the chosen temperate or rate was high enough, the Non-Iterative Sampling option would become problematic. The option within the program would adjust the strain or torque with a large magnitude change caused by a reasonably fast material hardening. The program would then adjust the opposite parameter of the peak to compensate for the large change in parameters like storage and loss modulus. This would continue during and after the material cured, appearing as a zigzag between the strain and torque. After testing, the solution was to lower the strain and torque, as much as possible while not compromising data collection, this way when the Non-Iterative Sampling made adjustments during curing, they would not spike to the point the cyclic pattern would compromise the experiment.

However as higher rates and temperatures were collected, this solution failed. The solution was to adjust the sampling setting to achieve data collection rate. This was done to allow the Non-iterative Sampling to have a larger amount of data to make adjustments. The data collected using this method gave much better results.

A small adjustment was also used in the isothermal procedure. To ensure no kinetics were missed during the heating prior to recording data, while the material was heated to its chosen isothermal temperature, the isothermals were treated as a two-part experiment. The first part being a very short 90s non-isothermal run with an uncapped heating rate, and the second part being an isothermal experiment. This allowed us to monitor the material the entire time starting from the base 23°C to the designated isothermal temperature.



SI Figure 10: Example of strain issue shown from early experimental data: Plot on left shows storage and loss modulus, plots on right show the torque and displacement of the rheometer and how that effects data acquisition



SI Figure 11: Strain amplitude test at 25°C

## References:

- Akahira, T. J. R. R. C. I. T., & T. Sunose. (1971). Method of determining activation deterioration constant of electrical insulating materials. Res Rep Chiba Inst Technol (Sci Technol), 22–31.
- Aradhana, R., Mohanty, S., & Nayak, S. K. (2020). A review on epoxy-based electrically conductive adhesives. *International Journal of Adhesion and Adhesives*, 99, 102596. <https://doi.org/10.1016/j.ijadhadh.2020.102596>
- Byung-Seung Yim , Yumi Kwon, Seung Hoon Oh , Jooheon Kim , & Yong-Eui Shin. (2012). Characteristics of solderable electrically conductive adhesives (ECAs) for electronic packaging. *Microelectronics Reliability*, 52(6), 1165–1173. <https://doi.org/10.1016/j.microrel.2011.12.004>
- Capitain, C., Ross-Jones, J., Möhring, S., & Tippkötter, N. (2020). Differential scanning calorimetry for quantification of polymer biodegradability in compost. *International Biodeterioration & Biodegradation*, 149, 104914. <https://doi.org/10.1016/j.ibiod.2020.104914>
- Cheng, S., & Huang , Chien-Ming. (2017). A review of lead-free solders for electronics applications. *Microelectronics Reliability*, 75, 77–95. <https://doi.org/10.1016/j.microrel.2017.06.016>
- D'Angelo, D., Ramkumar, S. M., Wentlent, L., & Borgesen, P. (2012, November 9). Evaluation of a novel anisotropic conductive adhesive shear under multiple tin-lead and lead-free reflow... Unknown. [https://www.researchgate.net/publication/267595602\\_Evaluation\\_of\\_a\\_Novel\\_Anisotropic\\_Conductive\\_Adhesive\\_Shear\\_Under\\_Multiple\\_Tin-Lead\\_and\\_Lead-Free\\_Reflow\\_Cycles\\_for\\_Package-on-Package\\_POP\\_Assembly](https://www.researchgate.net/publication/267595602_Evaluation_of_a_Novel_Anisotropic_Conductive_Adhesive_Shear_Under_Multiple_Tin-Lead_and_Lead-Free_Reflow_Cycles_for_Package-on-Package_POP_Assembly)
- Domínguez, J. C., Alonso, M.V. , & Oliet, M. (2010). Kinetic study of a phenolic-novolac resin curing process by rheological and DSC analysis. *Thermochimica Acta*, 498(1–2), 39–44. <https://doi.org/10.1016/j.tca.2009.09.010>
- Drzeżdżon, J., Jacewicz, D., Sielicka, A., & Chmurzyński, L. (2019). Characterization of polymers based on differential scanning calorimetry based techniques. *TrAC Trends in Analytical Chemistry*, 110, 51–56. <https://doi.org/10.1016/j.trac.2018.10.037>
- Gill, P., Moghadam, T. T., & Ranjbar, B. (2010). Differential scanning calorimetry techniques: Applications in biology and nanoscience. *Journal of Biomolecular Techniques : JBT*, 21(4), 167–193.
- Gong, T., Si-Piao , P., & Rui-Ying , B. (2016). Low percolation threshold and balanced electrical and mechanical performances in polypropylene/carbon black composites with a continuous segregated structure. *Composites Part B: Engineering*, 99, 348–357. <https://doi.org/10.1016/j.compositesb.2016.06.031>
- Grout, I. (2011). *Digital systems design with fpgas and cplds*. Elsevier. <https://doi.org/10.1016/B978-0-7506-8397-5.00003-9>
- Gul, V. E. (2003). *Encyclopedia of polymer science and technology* (Vol. 5, pp. 652–697). (Original work published 1996)
- Hellebois, T., Fortuin, J., & Xu, X. (2021). Structure conformation, physicochemical and rheological properties of flaxseed gums extracted under alkaline and acidic conditions. *International Journal of Biological Macromolecules*, 192, 1217–1230. <https://doi.org/10.1016/j.ijbiomac.2021.10.087>
- Hoang-Vu Nguyen, Erik Andreassen , Helge Kristiansen , & Rolf Johannessen, Et al. (2013). Rheological characterization of a novel isotropic conductive adhesive – Epoxy filled with metal-coated polymer spheres. *Materials & Design (1980-2015)*, 46, 784–793. <https://doi.org/10.1016/j.matdes.2012.11.036>

- Jaroslav Šesták, & Gunnar Berggren. (1971). Study of the kinetics of the mechanism of solid-state reactions at increasing temperatures. *Thermochimica Acta*, 3(1), 1–12. [https://doi.org/10.1016/0040-6031\(71\)85051-7](https://doi.org/10.1016/0040-6031(71)85051-7)
- Jin, F.-L., Li, X., & Park, Soo-Jin . (2015). Synthesis and application of epoxy resins: A review. *Journal of Industrial and Engineering Chemistry*, 29, 1–11. <https://doi.org/10.1016/j.jiec.2015.03.026>
- Krupa, I., Cecen, V., & Boudenne, A. (2013). The mechanical and adhesive properties of electrically and thermally conductive polymeric composites based on high density polyethylene filled with nickel powder. *Materials & Design*, 51, 620–628. <https://doi.org/10.1016/j.matdes.2013.03.067>
- Li, Y., & Wong, C. P. (2006). Recent advances of conductive adhesives as a lead-free alternative in electronic packaging: Materials, processing, reliability and applications. *Materials Science and Engineering: R: Reports*, 51(1–3), 1–35. <https://doi.org/10.1016/j.mser.2006.01.001>
- Ma, H., Zhang, X., Ju, F., & Tsai, S.-B. (2018). A study on curing kinetics of nano-phase modified epoxy resin. *Scientific Reports*, 8(1), 1–15. <https://doi.org/10.1038/s41598-018-21208-0>
- Martha. (2016, August 8). *Printed circuit boards*. Digilent Reference. <https://digilent.com/reference/learn/fundamentals/electronic-components/printed-circuit-boards/start>
- Mir, I., & Kumar, D. (2008b). Recent advances in isotropic conductive adhesives for electronics packaging applications. *International Journal of Adhesion and Adhesives*, 28(7), 362–371. <https://doi.org/10.1016/j.ijadhadh.2007.10.004>
- Moon, S., Sigmarsson, H., Huang, Y., Bruemmer, T., Khanna, S., & Chappell, W. (2010). Magnetically aligned anisotropic conductive adhesive for microwave applications. *IEEE Transactions on Microwave Theory and Techniques*.
- Osswald, T. A., & Rudolph, N. (2015). *Polymer rheology: Fundamentals and applications*. Hanser Gardner Publications. <https://chooser.crossref.org/?doi=10.3139%2F9781569905234> (Original work published 2013)
- Pérez, J. M., Oliet, M., & Rodríguez, F. (2009). Cure kinetics of lignin–novolac resins studied by isoconversional methods. *Thermochimica Acta*, 487(1–2), 39–42. <https://doi.org/10.1016/j.tca.2009.01.005>
- Qiao, Y., Das, O., Zhao, S.-N., Sun, T.-S., Xu, Q., & Jiang, L. (2020). Pyrolysis kinetic study and reaction mechanism of epoxy glass fiber reinforced plastic by thermogravimetric analyzer (TG) and TG-FTIR (fourier-transform infrared) techniques. *Polymers*, 12(11), 2739. <https://doi.org/10.3390/polym12112739>
- Ramachandran, V. S., & Beaudoin, J. J. (2001). *Handbook of Analytical Techniques in Concrete Science and Technology: Principles, Techniques and Applications*. William Andrew.
- Ramkumar, S. M., & Srihari, K. (2006, January 1). Performance of a novel anisotropic conductive adhesive under thermal and temperature/humidity aging conditions. Unknown. [https://www.researchgate.net/publication/288402413\\_Performance\\_of\\_a\\_novel\\_anisotropic\\_conductive\\_adhesive\\_under\\_thermal\\_and\\_temperaturehumidity\\_aging\\_conditions](https://www.researchgate.net/publication/288402413_Performance_of_a_novel_anisotropic_conductive_adhesive_under_thermal_and_temperaturehumidity_aging_conditions)
- Ramkumar, S. M., & Srihari, K. (2007, January 1). Modeling and experimental verification of the contact resistance of a novel anisotropic conductive adhesive. Unknown. [https://www.researchgate.net/publication/267590018\\_Modeling\\_and\\_Experimental\\_Verification\\_of\\_the\\_Contact\\_Resistance\\_of\\_a\\_Novel\\_Anisotropic\\_Conductive\\_Adhesive](https://www.researchgate.net/publication/267590018_Modeling_and_Experimental_Verification_of_the_Contact_Resistance_of_a_Novel_Anisotropic_Conductive_Adhesive)

- Ramkumar, S. M., Venugopalan, H., & Khanna, K. (2011). Novel anisotropic conductive adhesive for 3D stacking and lead-free PCB packaging — A review. IEEE Xplore.
- Rueda, M. M., Auscher, Marie-Camille, Fulchiron, René, & Périé, T. (2017). Rheology and applications of highly filled polymers: A review of current understanding. *Progress in Polymer Science*, 66, 22–53. <https://doi.org/10.1016/j.progpolymsci.2016.12.007>
- Sangroniz, L., Fernández, M., & Santamaria, A. (2023). Polymers and rheology: A tale of give and take. *Polymer*, 271, 125811. <https://doi.org/10.1016/j.polymer.2023.125811>
- Schafer, R. W. (n.d.). *What is a savitzky-golay filter? [Lecture notes]*. IEEE Xplore. Retrieved April 4, 2024, from <https://ieeexplore.ieee.org/document/5888646>
- Schindler, A., Doedt, M., Gezgin, Ş., Menzel, J., & Schmölzer, S. (2017). Identification of polymers by means of DSC, TG, STA and computer-assisted database search. *Journal of Thermal Analysis and Calorimetry*, 129(2), 833–842. <https://doi.org/10.1007/s10973-017-6208-5>
- Strasser, C. (n.d.). *How to apply the cox-merz rule: A step-by-step guide*. NETZSCH - Analyzing and Testing. Leading in Thermal Analysis, Rheology and Fire Testing. Retrieved April 1, 2024, from <https://analyzing-testing.netzsch.com/en/application-literature/how-to-apply-the-cox-merz-rule-a-step-by-step-guide>
- Trihatri, M., Dwivedi, U. K., & Khan, Fozia Haque. (2015). Effect of curing on activation energy and dielectric properties of carbon black–epoxy composites at different temperatures. *Journal of Non-Crystalline Solids*, 421, 1–13. <https://doi.org/10.1016/j.jnoncrysol.2015.04.020>
- Tziamtzi, C. K., & Chrissafis, K. (2021). Optimization of a commercial epoxy curing cycle via DSC data kinetics modelling and TTT plot construction. *Polymer*, 230, 124091. <https://doi.org/10.1016/j.polymer.2021.124091>
- Upton, L. (2011, December 6). *High-res pics of the PCBs*. Raspberry Pi. <https://www.raspberrypi.com/news/high-res-pics-of-the-pcbs/>
- Vyazovkin, S., Burnham, A. K., Criado, J. M., Pérez-Maqueda, L. A., Popescu, C., & Sbirrazzuoli, N. (2011). ICTAC Kinetics Committee recommendations for performing kinetic computations on thermal analysis data. *Thermochimica Acta*, 520(1–2), 1–19. <https://doi.org/10.1016/j.tca.2011.03.034>
- Vyazovkin, S., Chrissafis, K., Di Lorenzo, M. L., Pijolat, M., & Koga, N. (2014). ICTAC Kinetics Committee recommendations for collecting experimental thermal analysis data for kinetic computations. *Thermochimica Acta*, 590, 1–23. <https://doi.org/10.1016/j.tca.2014.05.036>
- Zhang, Y., Fang, R., Xue, H., Xia, J., & Lin, Q. (2022). Investigation of DSC curing kinetic model fitting and rheological behavior of urushiol/IPDI system. *Thermochimica Acta*, 711, 179210. <https://doi.org/10.1016/j.tca.2022.179210>
- Zheng, T., Xi, H., Wang, Z., Zhang, X., Wang, Y., Qiao, Y., Wang, P., Li, Q., Li, Z., Ji, C., & Wang, X. (2020). The curing kinetics and mechanical properties of epoxy resin composites reinforced by PEEK microparticles. *Polymer Testing*, 91, 106781. <https://doi.org/10.1016/j.polymertesting.2020.106781>
- Zhongliang, M., Le, Q., Wei, H., & Liming, H. (2019). A novel approach on the study of cure kinetics for rheological isothermal and non-isothermal methods. *Composites Part B: Engineering*, 162, 242–249. <https://doi.org/10.1016/j.compositesb.2018.10.066>
- ZTACH ACE. (2017, October 11). Sunray Scientific. <https://sunrayscientific.com/solutions/>